EXPERIMENTAL AND NUMERICAL ANALYSIS OF DIRECT CONTACT CROSS FLOW PACKED BED CONDENSERS

By

Parnab Saha

A DISSERTATION

Submitted to
Michigan State University
in partial fulfillment of the requirements
for the degree of

Mechanical Engineering – Doctor of Philosophy

2022

ABSTRACT

Efficient, simple, and cost-effective approaches to mitigate shortages of freshwater are much needed today. Humidification and dehumidification (HDH) desalination systems are particularly well suited for small and distributed installations that can treat high salinity waters which are often found deep underground or associated with produced water. HDH systems however can be relatively inefficient when equipped with conventional heat exchangers. The installation of a direct contact packed bed in a HDH system is simple and can improve its performance significantly. Recent studies in HDH systems have been performed on counterflow direct contact condensers within a packed bed. The goal of this work is to perform a detailed study of crossflow direct contact condensers within a packed bed. Crossflow configuration is simple to install in larger units, the liquid supply and exhaust approach is also less complicated compared to counterflow systems. A two-dimensional mathematical model has thus been developed to estimate the performance of the system. The model is based on the balance of mass and energy. The resulting differential equations are solved numerically to predict the temperature of the water, air, and packed bed. Optimization was done using a genetic algorithm to find an optimized dimension of the packed bed domain to achieve the highest water production for a given volume A lab scale experimental setup has been built up to validate all results. In addition, the impact of geometry changes in the packed bed shape and flow directions were studied. A two-dimensional mathematical model was adopted to model condensers with new geometries. Computational results show that a wedge-shaped crossflow direct contact condenser can be 10-12 percent more effective than a regular rectangle cuboid-shaped packed bed condenser, square-shaped crossflow condenser. In addition, a compact cylindrical design of a crossflow HDH system configuration has been proposed, modeled, and its performance is presented.

ACKNOWLEDGMENTS

First, I would like to express my gratitude to my advisor, Professor Andre Benard. He is the one who saw potential in me to do PhD and hired me as a graduate research assistant in his research lab. As I came to do PhD after my bachelors, I did not have a lot of research experiences. He has taught me how to proceed with a simple idea and make it. In my last three years, I have never seen him without smile. He has taught me how to be persistent in doing research without being frustrated. I would like to thank him for being patient with my shortcomings and inadequacies.

I would also like to thank Dr Xu Tan, for his encouragement and support throughout the course of my graduate study. He helped me from very first stage of my PhD. With the help of him, I learnt how to develop an experimental setup and run it successfully. In this thesis study, enthalpy-based modeling code has been developed by him which has helped me to match my experimental results more accurately. I would also like to thank Professor James Klausner, Abraham Engeda, Charles Petty and Junlin Yuan for providing me feedback with some insightful comment which has made my PhD journey easier and more significant.

Building an experimental setup from scratch was not an easy task if Jared Koekkoek was not there. I am grateful to his assistance regarding 3D printing and building experimental setup. Thanks for helping me to apply idea and spending tireless night doing 3D printing. Thanks to Mahyar Abedi for his continuous support throughout my PhD. I enjoyed our academic discussion which used to enhance my motivation. Thanks to another lab mate Raghav Bihani for spending nights after night for helping me to implement our idea regarding compact crossflow HDH system.

I would like to thank my professors of BUET (Bangladesh University of Engineering and Technology) and Dr Mohammed Abdul Hannan (Lecturer of University of British Columbia) to educate me with a solid foundation of engineering which has helped me during PhD study. I would also like to thank Muhammad Rubayat bin Shahadat, Fatema Tuz Zohra, Towhidur Rahman, Saima Alam, Shimanto Chowdhury, Suvro Sudip, Nikita Saha, Dr. Al Ahsan Talukder and Dr. Nusair Hasan for their guidance regarding academic and personal needs. Thanks to my brother-in-law Sujan Saha and my only sister Purnita Saha. My PhD life would not be smooth without you!!!

I would especially like to thank my wife, Anashua Roy and my mother Sheuli Saha, for their love and support throughout my graduate studies. I would like to dedicate my PhD thesis my father Dr. Pran Kanai Saha. He is the one who inspired me to do PhD. He was there for me in all ups and downs during PhD. He spent night after night listening to my work and supported in every possible way to go through this long journey of PhD.

The support of ARPA-E(Advanced Research Project Agency-Energy) of the US department of energy under award no DR-AR0001000 is gratefully acknowledged. I would also like to thank Department of Mechanical Engineering in Michigan State University to give me such a great opportunity.

TABLE OF CONTENTS

CHAPTER 1 : Introduction	1
CHAPTER 2 : Thermal Desalination Technology	8
CHAPTER 3 : Modeling Direct Contact Crossflow Packed Bed Condensers	5
CHAPTER 4 : Evaluation of Mass Transfer and Interfacial Area Correlations in Direct Contact Packed Bed: Comparison of Correlations	
CHAPTER 5 : Optimization of Direct Contact Cross Flow Packed Bed Condenser 5	0
CHAPTER 6: Modeling and Experimental Validation of Direct Contact Crossflow Packed Bed Condenser Used in HDH Desalination system	
CHAPTER 7 : Modeling of Compact Crossflow Cylindrical HDH system : Condenser Performance Analysis	6
CHAPTER 8 : Summary, Conclusion, and Future Work	0
REFERENCES	3
APPENDIX12	21

CHAPTER 1: Introduction

1.1 Context

All living species around the world cannot live without water. Though 71 percent of the world is covered by water, 97 percent of them are from seawater. Moreover, rapid population growth, industrial revolution has led the world towards scarcity of water. According to United Nation Environment Program(UNEP), around 66.7 percent will face water shortage by 2025[1]. Therefore, the distillation system has been a significant research interest over the past years. .Desalination is one of the straightforward to fulfill the demand of freshwater [2][3]. Reverse osmosis (RO), single-stage multistage flash distillation (MSF), multi-effect distillation (MED), and vapor compression distillation (VCD) are just a few of the desalination methods that are currently available.[4] [5] [6]. Among them RO (reverse osmosis) is favored due to its low cost [3]. Reverse osmosis, on the other hand, rejects water that is still highly salinized and has larger pressure drops which leads to concern when discharged into environment. [7]. Therefore, thermal based humidification and dehumidification desalination (HDH) is a low-cost approach to treat compromise waters using low-grade heat or solar energy [8]. It can treat water of wide range of salinity and can treat industrial wastewater. A better design of HDH system can have zero brine discharge[9][10]. In Figure 1-1, the operation of a typical HDH system is shown. Seawater is heated by a solar heater at the start of the process, and it is then supplied to a humidifier. Warm, humid air is produced when cold air going into the humidifier is exposed to the heated seawater. Warm, humid air coming out of the humidifier is drawn into a dehumidifier where it loses heat to the cool seawater that is also fed.

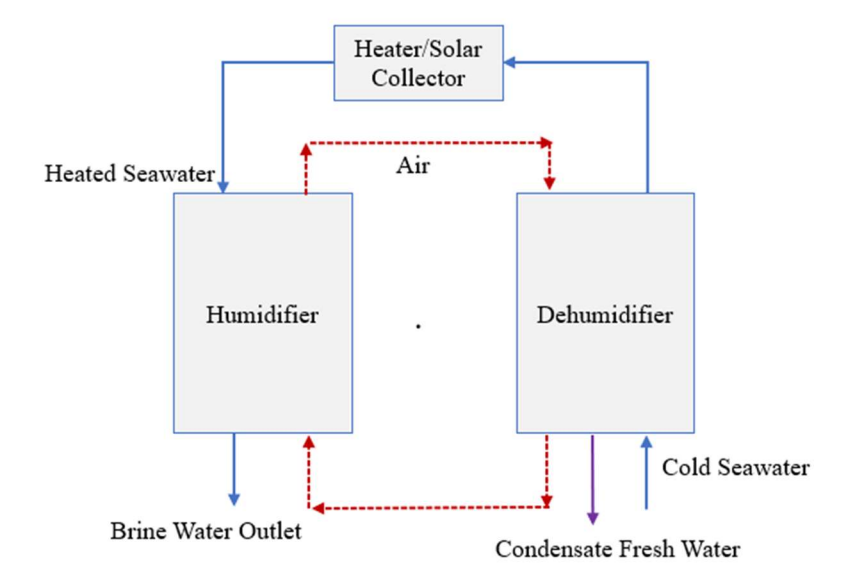


Figure 1-1. A typical HDH system consisting of a humidifier and dehumidifier where the blue line represents water, and the red line represents the airflow[8]

Different sources can be used as a preheater such as PV panel, heat pump [11] [12]. Several researchers have investigated Humidification and Dehumidification desalination (HDH) system efficiencies from around 1990. Table 1-1 shows previously used different types of condensers taken for research studies. K.Bourouni et al.[13] did experiment by compressing humid air and installing by absorbing water from the humid atmosphere.

Table 1-1. List of previous representative research on HDH desalination systems based on the types of condensers (dehumidifiers)

	Experimental	Parametric	Analytical modeling	l	Direct	Concurrent/ Counter flow	Crossflow
Y. Assouad [14]	✓			✓			✓
S. Al-Hallaj [15]	✓			✓		✓	
R. H. Xiong [16]	✓			✓		\checkmark	
Y. Li [17] [18]	✓		✓		✓	✓	
F. Alnaimat [19] [20]	√		✓		✓	✓	
M. Zamen [21]	✓			✓		✓	
H. Xu [11]	✓			✓			✓
D. U. Lawal [22]		✓		✓		✓	✓
A. Mohamed [4]		✓			✓	✓	
M. I. Zubair [23]		✓		✓		✓	
S. Hou [24]		✓		✓		✓	
Fouda [25]	✓	✓		✓		✓	
Zhao, Y [26]	✓	✓			✓		✓
Kabeel [5]	✓	✓		✓		✓	
Gabrielli [27]		✓	✓		✓	✓	
Hu [28]	✓	✓	✓		✓	✓	

In 1998,Al-Hallaj et al.[15],Assouad and Lavan et al.[14] have shown the proper usage of thermodynamics energy in the HDH system analytically and experimentally as well. Al-Hallaj et al.[15], Xiong et al.[16],Muller-Holst et al. [29], Goosen et al.[30] El-Dessousky et al.[31] have discussed the high efficience of humidification and dehumidification system and also economic viability. However, most of the analyses were based on experimental and parametric analysis. Klausner et al.[18] and Li et al. [17] have developed a mathematical formulation for analyzing steady-state direct contact condensation packed bed evaporator and condensers. They used the fundamentals of heat and mass transfer to formulate the equation. They have built an experimental setup. The experimental result and numerical result had a good match. In 2011, Alnaimat et al.[19]

developed a mathematical model for a transient direct contact condenser and evaporation and also built an experimental setup. The performance of condensation and evaporation depends on several factors such as air, water temperature and the humidity ratio, etc. The model of Alnaimat et al.[19] takes into consideration parameters such as interfacial area for heat and mass transfer. The numerical simulations and experimental results also had a good fit. The above studies on HDH systems are based on a counterflow configuration.

Though many kinds of literature are available in direct contact counter flow packed bed HDH systems, there is very less research on crossflow packed bed HDH systems. In 2017, Lawal et al.[22],[32] developed a three-stage cross flow packed HDH system where humidification system was direct contact but condenser was made of three aluminum fins and copper tubes. In 2018, Xu et al.[11] developed a a single-stage and two-stage cross-flow HDH system to improve on the heat recovery. Their main objective was to obtain optimal operating parameters of the system. They have used shell and tube heat exchanger as condenser. The indirect contact condenser has several disadvantages such as corrosion, high-pressure drops, less lifetime, and efficiency. In 2019, Zhao. Y et al.[26] developed a crossflow HDH system. They used a crossflow direct contact condenser and presented a systematic and parametric analysis of the system.

Though the thermal performance of a crossflow cooling tower was an important subject of analysis of the last few decades, no study has been found on developing a mathematical model regarding cross flow direct contact condenser within a packed bed. Commonly used methods for estimating the rates of heat and mass transfer of crossflow systems are the so-called Merkel method [33] and the effectiveness-NTU method [34]. Merkel's approach is used for evaluating the performance of cooling towers and assumes that the Lewis number has a value of 1, which is the ratio of thermal and mass diffusivities. It also neglects mass losses due to evaporation of the liquid

water phase. Merkel's analysis underpredicts the performance of the cooling towers [35]. The effectiveness-NTU method, which is presented in Jaber and Webb [34], is also based on the assumption of a Lewis number having a value of one. The advantage of the effectiveness-NTU method is its simplicity for a crossflow configuration, but it has similar limitations as Merkel's method [33]. Besides, there is no exact correlation for estimating NTU for crossflow direct contact packed bed condenser is available in effectiveness-NTU method.

The goal of this research work is to propose a crossflow direct contact HDH system as shown in Figure 1-2.

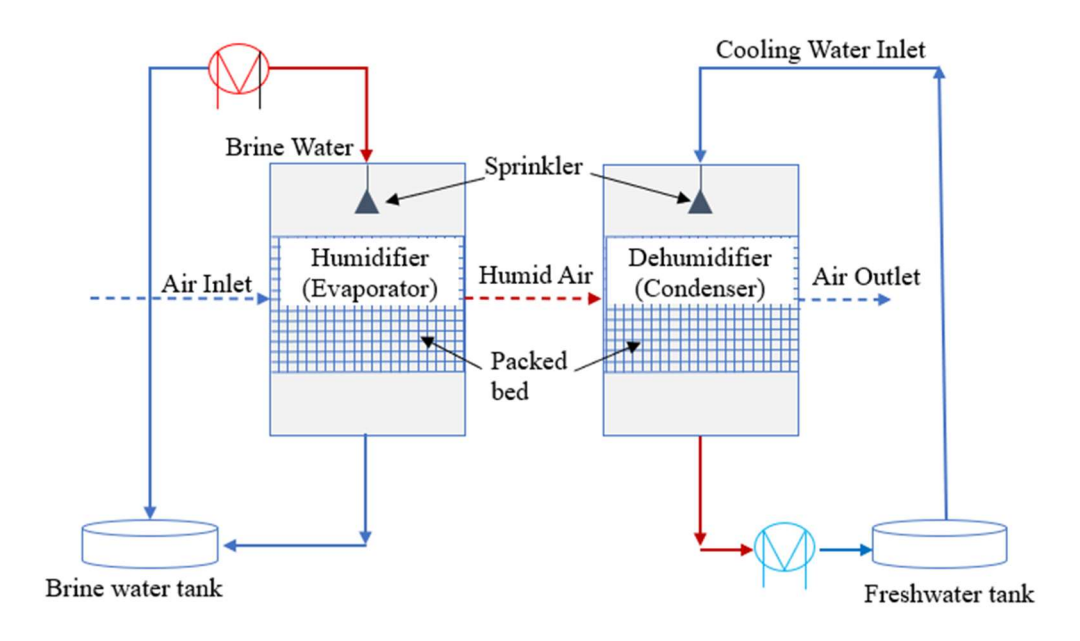


Figure 1-2. Typical configuration of crossflow compact packed bed condensers

In the above figure, Air-vapor flows horizontally all the way through humidifier and dehumidifier, while the hot sea water and cooling freshwater are sprayed from the tops of the humidifier and dehumidifier, respectively. Comparing to counterflow HDH systems, a crossflow system has lower effectiveness but simpler structure without the many elbows to redirect the air flow.

The aim of this PhD study is to investigate a detailed analysis of crossflow packed bed condensers by adopting a mathematical model, experimental setup, and optimization as it is more compact, easy to install, less complex piping.

1.2 Objectives

As a part of my PhD, I have developed a mathematical model for crossflow packed bed condenser. A MATLAB platform has been used to solve coupled PDE using finite differences method. Newton's method is also adopted by COMSOL to solve the set of partial differential equations.[36] [37]. Then GA optimization has been used to have an idea that what should be the optimized dimension of packed bed condenser to get highest effectiveness and water production [38]. A wedge shape design has also been proposed and showed the improved effectiveness through simulation. A lab scale direct contact crossflow packed bed condenser of (0.4x0.3x0.2)m has been built. Around 35 thermocouples have been inserted throughout the packed bed. Experimental results have been compared with simulation results and a detailed analysis has been conducted to show how temperature changes throughout the domain. Finally, a more compact design has been proposed which does not require complex piping and it can be accommodated any industrial places easily.

1.3 Thesis Organization

The thesis has been organized in a proper manner which is described below:

- ➤ In chapter 1, I have discussed the background studies in direct contact packed bed systems and importance of this study in present world
- ➤ In chapter 2,Some existing desalination technologies are explained.
- ➤ In chapter 3, I have explained why Onda's correlation work better than other existing correlation in packed bed.

- ➤ In chapter 4, I have discussed the formulation of mathematical model and solving technique in finite difference method and finite element methods. I will also show comparison with counterflow direct contact packed bed condenser
- ➤ In chapter 5, I have optimized dimension of packed bed with genetic algorithm and analyzed an innovative shape to improve the effectiveness of the system
- ➤ In chapter 6, I have shown the detailed analysis of experimental results in direct contact crossflow packed bed condenser
- ➤ In chapter 7, I have proposed a new compact design of a cylindrical crossflow packed bed condenser
- ➤ In chapter 8, I have summarized the whole research study of this thesis and proposed significant research studies for future.

CHAPTER 2 : Thermal Desalination Technology

2.1 General

Solar Desalination Techniques are mainly divided into two sections:

- (i). Indirect system in large plants majority consists of two components including desalination unit and solar collectors and,
- (ii). Direct system uses energy from solar radiation directly into the desalination unit. These systems do not need complex structures and are cost-effective.

These sections will offer an overview of the technologies which is currently installed and being used for freshwater production around the world.

2.2 Multi-Effect Distillation (MED)

MED is covering 7% of global solar desalination [39]. It is an effective process to produce freshwater with low enthalpy [40]. There are several types of MED systems such as Multi-Effect Distillation with Thermal Vapor Compression (MED-TVC), Multi-Effect Distillation with mechanical vapor compression (MED-MVC). The fundamental of multi-effect distillation is desalination of seawater or brackish water by applying successive boils. In this process, seawater is sprayed overheated pipe which only evaporates clean water. This is developing brine and freshwater vapor. MED systems maintain pressure and lower temperature than the previous stage. In designing of MED system, the difference between temperature initial stage and final stage needs to be maintained. Besides making the system more efficient preheaters can be used but that will increase the expenses of the system. Some of the design considerations can be taken in solar field selection to have high efficiency. Now mostly solar collectors are. (i) FPC (Flat Plate Collectors) (ii) PTC (parabolic through collectors) (iii) LFC (linear Fresnel collectors.) [41]. Some other vital parameters should be taken into consideration for example large-scale solar MED can be utilized,

the feasibility of location of the plant should be based on economic analysis [42]. However, nowadays. Adsorption technology (surface phenomenon) coupled

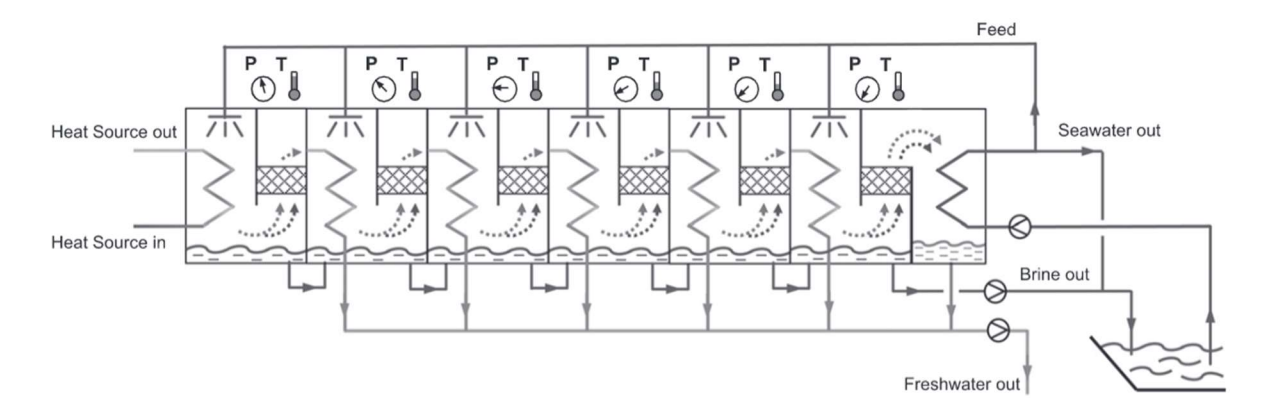


Figure 2-1. Schematic diagram of multi-effect distillation system with TVC [43] MED to increase the stage of the whole system and can be operated with good temperature difference.

In 2015, dela Calle et al.[44] has developed a dynamic model which was implemented using object-oriented Modelica modeling language. It can describe the physical analysis as well as heat and mass transfer phenomena of the system.

2.3 Solar Pond

A solar pond acts as a solar collector which can be used as heat storage for supplying thermal energy to desalination, agricultural needs, electricity generation. The advantage of the solar pond is that collections from solar energy can store its thermal energy for a longer period. Solar ponds can have two types. One is convective solar ponds and another one is non-convective solar ponds. The non-convective solar ponds are of three types .1. Membrane solar pond 2. polymer gel layers solar pond 3. Gradient solar pond. The SCGP (salinity gradient solar pond) is the most environmentally friendly. The solar pond typically has three layers. 1. Upper convective zone (UGZ) 2. Lower convective zone (LCZ) and salinity gradient non-convective zone (NCZ). Freshwater production by the solar pond is done with help of a multistage flash distillation system

(SPMSF). A solar pond is widely used in Israel, USA, India, and Australia now [45] [46] [47] [48]. Figure 2-2 shows a schematic diagram of SGSP. Solar radiation is used to heat water and store it for dense saline water [49].

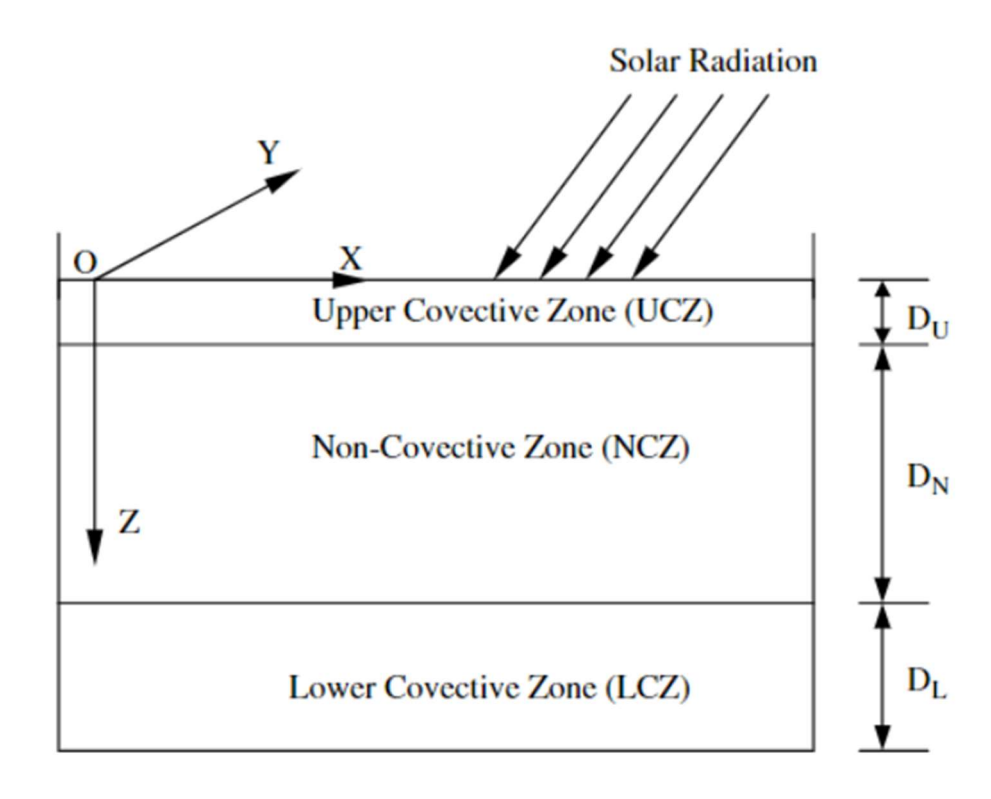


Figure 2-2. A schematic view of SGSP[49]

CFD study of One dimensional[50], Two dimensional [51], Three dimensional [52] conservation equations can be taken into consideration for analysis. To produce freshwater, it can be coupled with the MSF plant. According to Ali et al. [53], it can produce freshwater ranging from 2.37 to 7.2 m³/d.

2.4 Reverse Osmosis

The reverse osmosis process is a widely used water purification system around the world. It cover almost 69 percent worldwide production capacity[39] [53]. It uses a partially permeable membrane to distinguish between ions, molecules, larger particles from freshwater. In the reverse osmosis process, pressure is applied to overcome developed osmotic pressure which is driven by

chemical potential difference and thermodynamics. The membrane should be developed in such a way that large molecules should not allow ions through pores, but it may allow smaller components of the solution. In summary, the reverse osmosis process is based on the natural osmosis process in which water molecules go from low salinity to high saline solution through a semi-permeable membrane. The process stops when a system reaches equilibrium, then applying large pressure that osmotic pressure reverses the natural osmosis process. The advantage of reverse osmosis proves because of its easy adaptations to the local environment, meeting long-term demand [54]. Though it can adapt to the environment the major issue in the reverse osmosis process is semi-permeable membrane increases pressure demand to reverse the flow. This occurs fouling problems in the system. The fouling can be biofouling, organic or colloidal [55]. However, it can be controlled by increasing feed pressure and lowering mass flux. The main challenge of modeling RO systems is to predict the efficiency of reliability of RO systems [56]. The detailed and proper explanation of modeling a membrane is explained well by Wang [57].

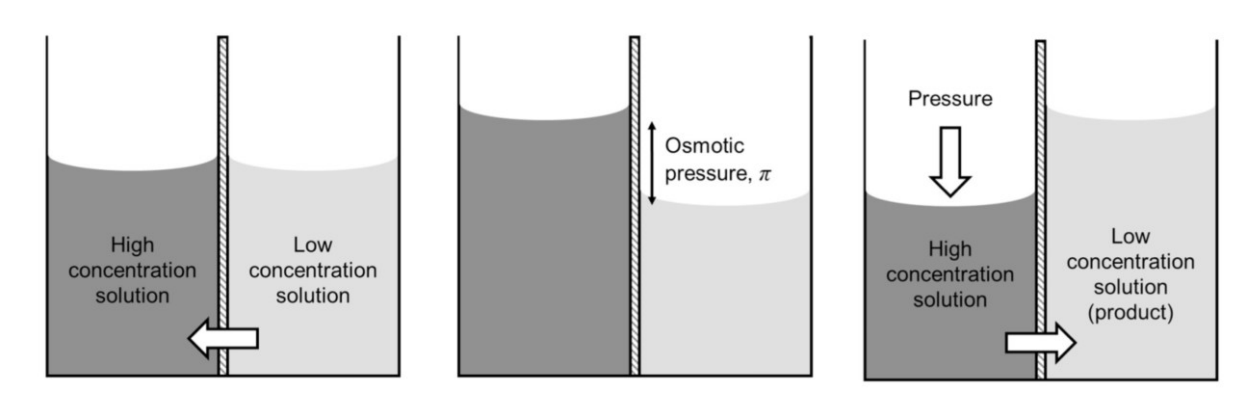


Figure 2-3. Reverse osmosis process Qasim et al. [58]

2.5 Solar Still

Solar still is a conventional approach to producing freshwater. It requires minimum skills, maintenance. The disadvantage of solar still is it requires a large amount of space. Solar still uses

solar radiation to follow evaporation and condensation. In as basin, saline water is a fully insulated feed, as radiation strikes saline water, the saline water starts evaporating. the vapor from saline water goes upward which helps condensation in the lowers side of the glass and freshwater is collected. However, to get higher distillate research has shown many efforts. Improvement of a reflector can be one promising way for solar still. There are mainly two subcategories of a reflector.

1. Internal Reflector 2. External Reflector. Figure 2-4 shows a basic design of solar still with reflectors.[59]

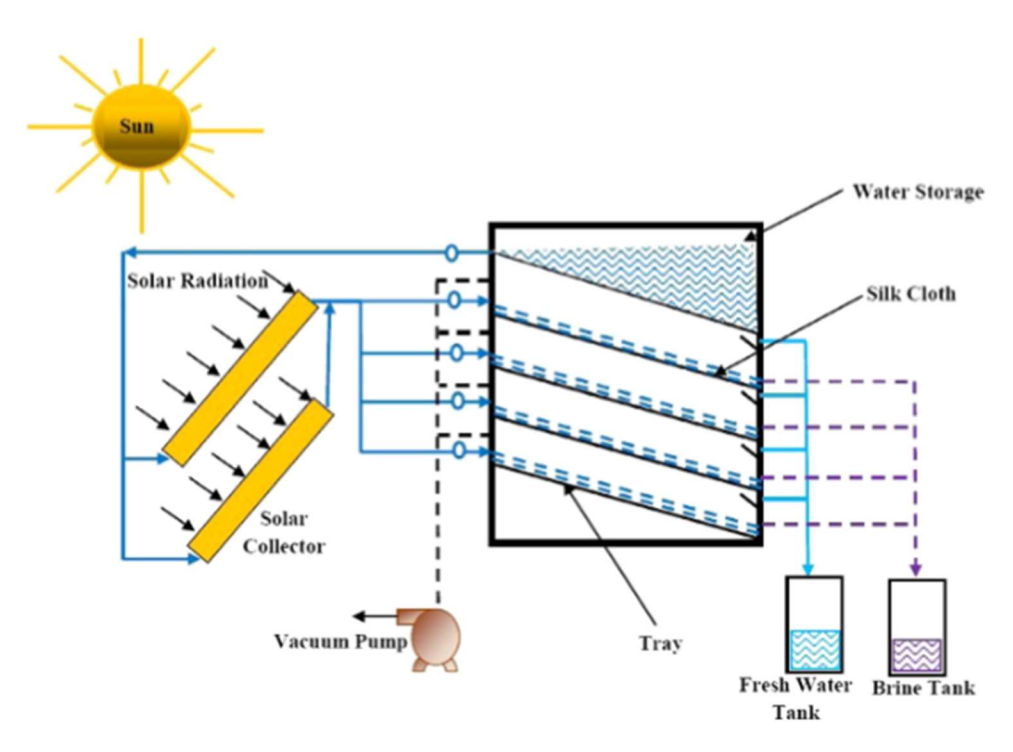


Figure 2-4. Basic design of solar still [3]

In recent decades, there have been several improvements made by researchers regarding solar still. In 2014, Shrivastava et al. [60] developed a solar still which is made of blackened jute clot pieces. It creases productivity by 57%. In 2017, Haddad et al. [61] showed rotating vertical can increase productivity by 51.1%.In the future solar still can be used for rainwater harvesting and distillation for river water. One of issues with this system is that there is not perfect correlation

to calculate convective heat transfer coefficient. Ahsan et al.[62] and Setoodeh et al. [63] did CFD study to come up with most accurate to conclude this issue.

2.6 Humidification Dehumidification (HDH)

Humidifier and dehumidifier are the main two components of the HDH system. In humidifier section, hot saline water is sprayed to increase the moisture of the air. Then in the dehumidifier, moist air coming out of the evaporator is made indirect contact with cold salty water. This causes water vapor to the condenser. The air circulation can be either natural or forced. HDH system can be classified into four parts such as closed air-closed water, open air-open water, closed air-open water, and open air-closed water. The saline water can be heated through a solar water heater or any other effective source. In 2017, Gang et al. [32] developed a mathematical model of HDH system which three stages of heat recovery for steady-state condition. His numerical model deviates from the mathematical model around 5 percent. Maximum freshwater production was obtained is 0.183m³/s. They have also concluded that with a smaller amount of water, better flow is yield. They also discussed that increasing stages increases dissipated energy. In 2017, Marale et al.[64] made a two-stage HDH system with air cooling. The proposed design show indicates higher production at the second stage than the first stage. In 2018, Rahimi-Ahar et al. [65] analyzed by varying pressure in humidification. HDH system can be coupled with solar still [66]. Water was heated by solar in the system. Besides, air circulation was a closed loop. Their studies show that if the pressure inside the humidifier is decreased, water vapor carrying capacity also increases. It has been showed that if pressure is decreased from 0.9 bar to 0.1 bar, water production increases from 54.16% to 57.89%.

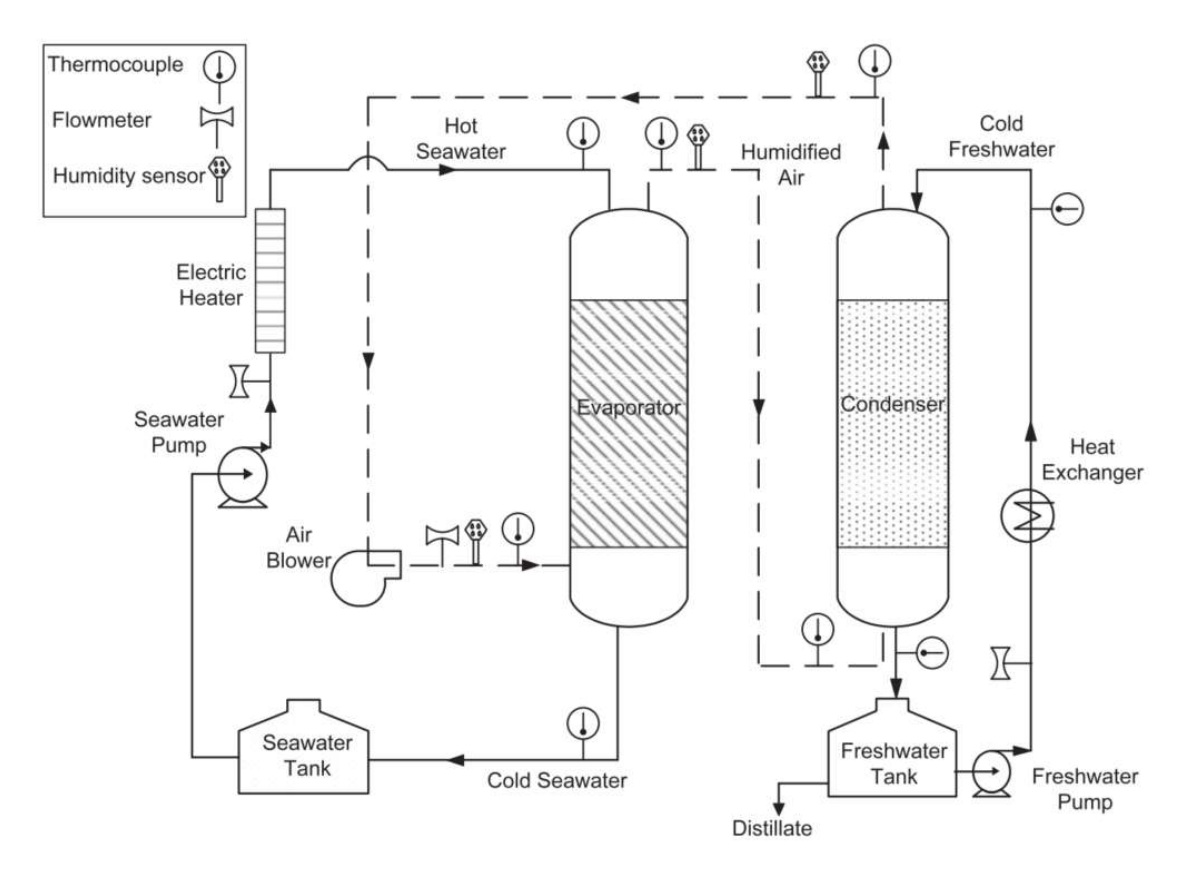


Figure 2-5. A schematic diagram of direct contact HDH system [11]

Alnaimat et al.[2] has done proper research on the recent advancement of HDH around the world. These studies give a clear view of finding optimal design and operating parameters for HDH systems. They mostly focused on GOR, mass flow rates, the temperature of the fluid to get optimized water production and less energy consumption. GOR is defined as

$$GOR = \frac{\dot{m}_w h}{Q_{heat}} \tag{2-1}$$

Which is measure of how much thermal energy is consumed in a desalination process. Decent amount of suggestions was proposed for the future to design an optimized direct contact packed bed condenser in the literature[2].

CHAPTER 3: Modeling Direct Contact Crossflow Packed Bed Condensers

3.1 Introduction

Humidification and dehumidification systems are based on relatively low-cost designs that operate using low grade heat. An important component in these systems is the condenser. The current chapter focuses on estimating the performance of a crossflow direct contact condenser in which the fluids flow perpendicularly from one another while being in direct contact. A packed bed is employed to enhance the surface area between the fluids. A steady-state two-dimensional model is presented for crossflow direct contact condensers incorporating a packed bed. The balances of mass and energy are solved numerically for the liquid, air/vapor, and packed bed phases. Simulations results are presented on crossflow condensers with varying inlet conditions for the liquid and air/vapor phases and compared with experimental data from the literature. In addition, a comparative study between cross flow and counter flow direct contact packed bed condensers is provided. It is found that both cross flow and counter flow direct condenser have almost similar freshwater production for most of the considered conditions. A cross flow configuration can thus also be used effectively instead of a counter flow direct contact packed bed condenser and can accommodate a variety of spaces and configurations.

3.2 Nomenclature

A surface area of the system (m^2)

 A_c cross-sectional area of packed bed (m²)

a specific area of packing material (m²/m³)

 C_p specific Heat(kJ/kg)

D Molecular diffusion coefficient(m²/s)

dx width of computational domain(m) Fr Froude Number g gravity (m^2/s) h_v enthalpy of vapor(kJ/kg) h_L enthalpy of liquid(kJ/kg) h_{fg} enthalpy of condensation(kJ/kg) *k* mass transfer co-efficient(m/s) M molecular vapor weight(kg/kmol) \ddot{m}_a mass flux of air(kg/m²s) \ddot{m}_L mass flux of liquid(kg/m²s) Nu Nusselt Number P Total pressure of the system(kPa) Re Reynolds number R Universal gas constant ((kJ/kmol K) Sc Schmidt number T Temperature(°C/K) *U* overall heat transfers co-efficient(W/m²K) We Webber Number

Z height of computational domain(m)
σ_L surface tension of a liquid(N/m)
ω Humidity ratio
σ_c surface tension of packing material(N/m)
μ dynamic viscosity (kg/ms)
ρ density(kg/m ³)
Subscripts
a air
cond condenser
mix mixture of vapor and air
sat saturation state of species
L liquid phase
v vapor phase
a air phase
in inlet condition
Out outlet condition
amb ambient state
pack packed bed

w wetted

LA liquid side parameter based on the specific area of packing material.

GA Gas side parameter based on the specific area of packing material.

3.3 Mathematical Formulation

3.4 Condenser

Condensation in a crossflow direct contact system is achieved by spraying cold water from the top and humid air flows from the side through a packed bed. Condensation occurs when water vapor in the humid air comes in contact with the colder liquid droplets. The relative directions of the streams are provided in Figure 3-1.

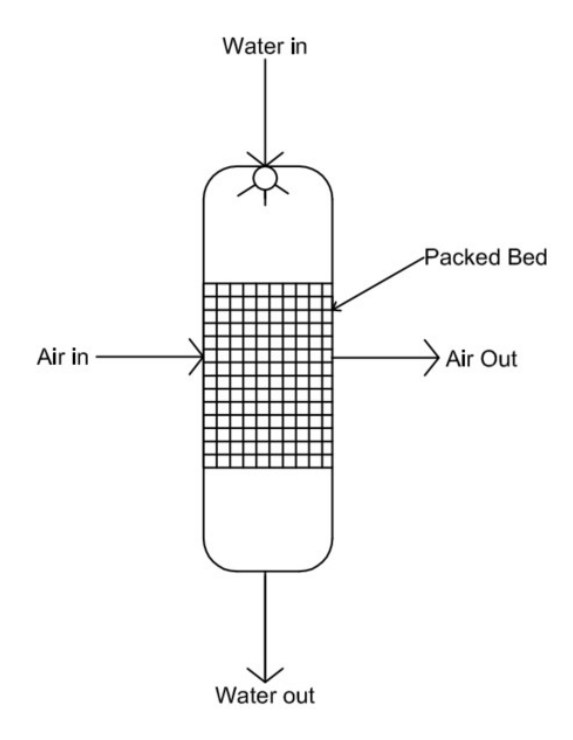


Figure 3-1. Diagram of crossflow packed bed condenser illustrating the various stream directions

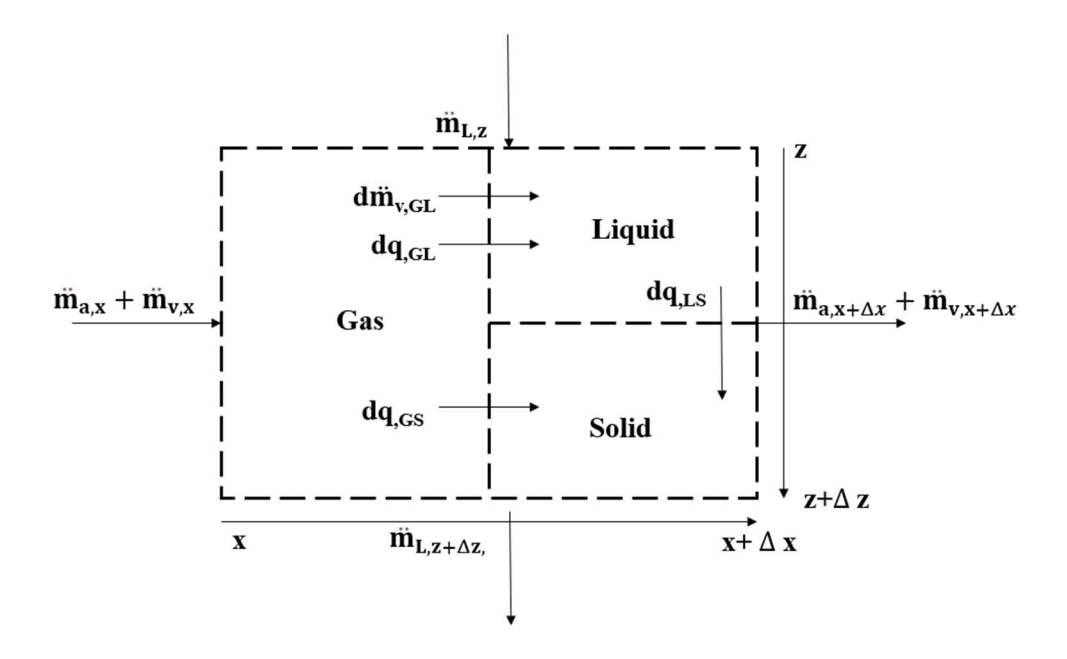


Figure 3-2. A simplified representation of the mass and energy exchanges between the three possible phases, gas phase comprises of air and water vapor, liquid phase is comprised of water from the inlet and condensation and solid phase corresponds to packing material at the small scale

A simplified diagram of mass and energy balances has been illustrated in Figure 3-2. Mass and energy balances, applied to a small control volume, result in equations that can provide the temperatures of the air, liquid phase, and packed bed. The momentum equation is not considered since the air flow is approximated as uniform and unidirectional on the system scale; the packed bed is approximated as a porous media. Other assumptions include steady state operations, no thermal losses to the environment, both air and water vapor are considered to follow the ideal gas model, and the relative humidity is set to 100 percent at the inlet and throughout condensation. The model is developed for a two-dimensional steady-state cross flow direct contact with packing material. The governing equations are developed below for both the liquid side and gas sides. Each phase is considered separately and interact through condensation and an interfacial area model.



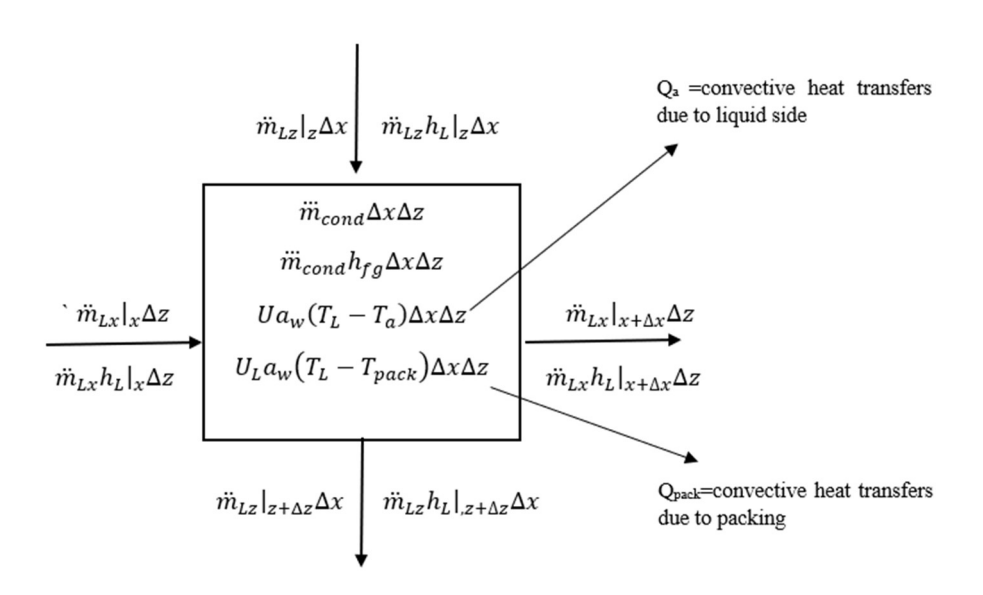


Figure 3-3. Cartesian coordinates and control volume used to determine the main Balance equations for the liquid phase

The control volume used for deriving the liquid phase equation is shown in Figure 3-3. Applying conservation of mass in liquid in the control volume, for Cartesian coordinates, results in

$$\ddot{m}_{Lz}|_{z}\Delta x - \ddot{m}_{Lz}|_{z+\Delta z}\Delta x + \ddot{m}_{Lx}|_{x}\Delta z - \ddot{m}_{Lx}|_{x+\Delta x}\Delta z = -\ddot{m}_{cond}\Delta x\Delta z$$
 (3-1)

where \ddot{m}_{Lx} is liquid of mass flux in the x-direction (kg/m²s), \ddot{m}_{Lz} is liquid of mass flux in the z-direction and \ddot{m}_{cond} is rate of condensation(kg/m³s). Similarly, after applying the conservation of energy for the liquid phase, we find that

$$\ddot{m}_{Lz}h_L|_z\Delta x - \ddot{m}_{Lz}h_L|_{,z+\Delta z}\Delta x + \ddot{m}_{Lx}h_L|_x\Delta z - \ddot{m}_{Lx}h_L|_{x+\Delta x}\Delta z$$

$$- Ua_w(T_L - T_a)\Delta x\Delta z - U_L a_w(T_L - T_{pack})\Delta x\Delta z$$

$$= -\ddot{m}_{cond}h_{fa}\Delta x\Delta z$$
(3-2)

In the above equations, \ddot{m}_L is the mass flux of liquid and it varies with both the x and z directions, h is the enthalpy of the phase, and h_{fg} is the heat of condensation. \ddot{m}_{cond} is the rate of condensation, U is the overall heat transfer coefficient between air and liquid, while U_L is the heat transfer coefficient between liquid and packing material, a_w is the wetted specific area T_L , T_{pack} , and T_a are the temperature of the liquid, packing material, and air within the differential control volume.

After simplifying the equations and taking their limits, Eq.(3-1) and Eq.(3-2) can be expressed as,

$$\frac{\partial \ddot{m}_L}{\partial x} + \frac{\partial \ddot{m}_L}{\partial z} = \ddot{m}_{cond} \tag{3-3}$$

$$-\frac{\partial (\ddot{m}_L h_L)}{\partial x} - \frac{\partial (\ddot{m}_L h_L)}{\partial z} = -\ddot{m}_{cond} h_{fg} + U a_w (T_L - T_a) + U_L a_w (T_L - T_{pack})$$
(3-4)

In Eq.(3-4), the first two terms represent enthalpy change in the x-direction and the z-directions. The first term on the right-hand side depicts latent heat of condensation, the second term is the convective heat transfer to the gas side, and the third term accounts for the heat transfer rate from the liquid to the packing.



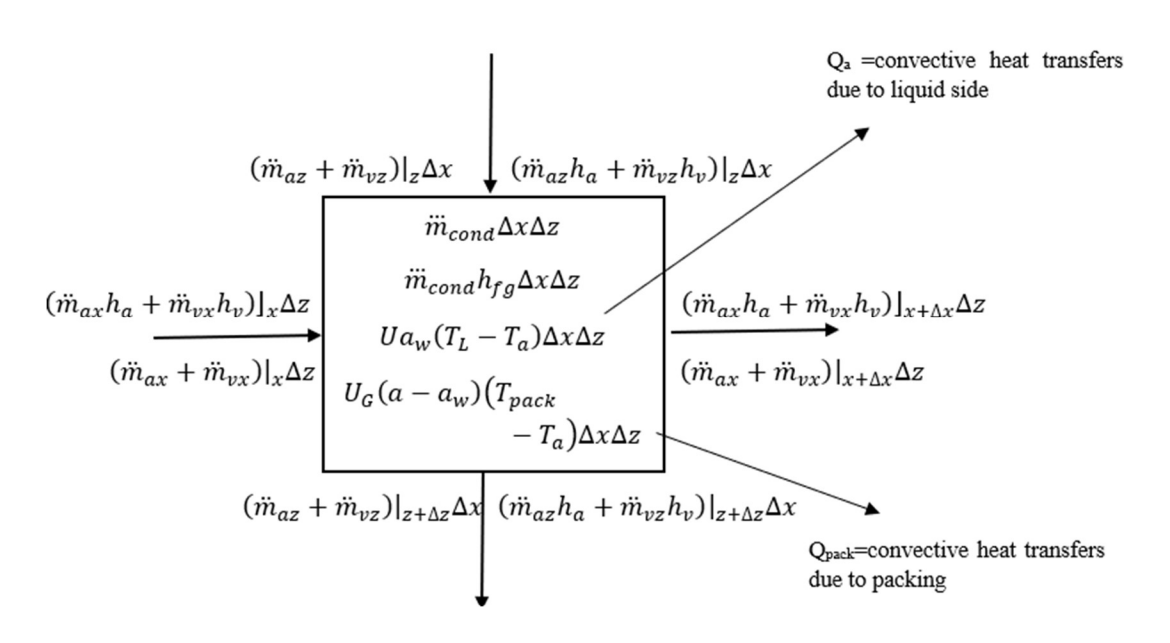


Figure 3-4. Cartesian coordinate and control volume used to determine the main balance equation for the gas phase

Figure 3-4 illustrates the control volume used for developing differential equations for the gas side. \ddot{m}_{cond} in the equation is a sink of mass as water vapor condenses. A similar expression for the balance of mass for the gas phase (air and vapor components) can be written as

$$(\ddot{m}_{az} + \ddot{m}_{vz})|_{z}\Delta x - (\ddot{m}_{az} + \ddot{m}_{vz})|_{z+\Delta z}\Delta x + (\ddot{m}_{ax} + \ddot{m}_{vx})|_{x}\Delta z - (\ddot{m}_{ax} + \ddot{m}_{vx})|_{x+\Delta x}\Delta z = \ddot{m}_{cond}\Delta x \Delta z$$

$$(3-5)$$

Likewise, the balance of energy for the gas components is

$$(\ddot{m}_{az}h_{a} + \ddot{m}_{vz}h_{v})|_{z}\Delta x - (\ddot{m}_{az}h_{a} + \ddot{m}_{vz}h_{v})|_{z+\Delta z}\Delta x + (\ddot{m}_{ax}h_{a} + \ddot{m}_{vx}h_{v})]_{x}\Delta z - (3-6)$$

$$(\ddot{m}_{ax}h_{a} + \ddot{m}_{vx}h_{v})|_{x+\Delta x}\Delta z = \ddot{m}_{cond}h_{fg}\Delta x\Delta z - U_{G}(a - a_{w})(T_{pack} - T_{a})\Delta x\Delta z - U_{G}(a - a_{w})(T_{pack} - T_{a})\Delta x\Delta z - U_{G}(a - a_{w})(T_{pack} - T_{a})\Delta x\Delta z$$

In Eq.(3-6), \ddot{m} is the mass flux of gases with units of kg/ (s·m²). Subscripts "az" and "vz" represent air and vapor in z direction and Subscripts "ax" and "vx" represent air and vapor in x direction. U_G is the heat transfer coefficient between air and packing material.

After taking their limits, Eq. (3-5) and energy balance Eq. (3-6) are expressed as

$$-\frac{\partial (\ddot{m}_a + \ddot{m}_v)}{\partial x} - \frac{\partial (\ddot{m}_a + \ddot{m}_v)}{\partial z} = -\frac{\partial (\ddot{m}_v)}{\partial x} - \frac{\partial (\ddot{m}_a)}{\partial x} - \frac{\partial (\ddot{m}_a)}{\partial z} - \frac{\partial (\ddot{m}_v)}{\partial z} = \ddot{m}_{cond}$$
(3-7)

$$-\frac{\partial (\ddot{m}_{a}h_{a} + \ddot{m}_{v}h_{v})}{\partial x} - \frac{\partial (\ddot{m}_{a}h_{a} + \ddot{m}_{v}h_{v})}{\partial z}$$

$$= \ddot{m}_{cond}h_{fg} - U_{G}(a - a_{w})(T_{pack} - T_{a}) - Ua_{w}(T_{L} - T_{a})$$
(3-8)

$$-\frac{\partial (\ddot{m}_a h_a + \ddot{m}_v h_v)}{\partial x} = -h_a \frac{\partial (\ddot{m}_a)}{\partial x} - \ddot{m}_a \frac{\partial (\ddot{m}_a)}{\partial x} - h_v \frac{\partial (\ddot{m}_v)}{\partial x} - \ddot{m}_v \frac{\partial (h_v)}{\partial x}$$
(3-9)

$$-\frac{\partial (\ddot{m}_a h_a + \ddot{m}_v h_v)}{\partial z} = -h_a \frac{\partial (\ddot{m}_a)}{\partial z} - \ddot{m}_a \frac{\partial (h_a)}{\partial z} - h_v \frac{\partial (\ddot{m}_v)}{\partial z} - \ddot{m}_v \frac{\partial (h_v)}{\partial z}$$
(3-10)

The following simplifications or steps are used in simplifying Eq.(3-3), Eq.(3-4), Eq.(3-7) and Eq.(3-8):

(1) The liquid flow on x-direction is negligible and thus

$$\frac{\partial \ddot{m}_L}{\partial z} = \ddot{m}_{cond} \tag{3-11}$$

(2) The gases flow directions in z are negligible, which implies that

$$-\frac{\partial (\ddot{m}_a + \ddot{m}_v)}{\partial x} - \frac{\partial (\ddot{m}_a + \ddot{m}_v)}{\partial z} \approx -\frac{\partial \ddot{m}_a}{\partial x} - \frac{\partial \ddot{m}_v}{\partial x} = \ddot{m}_{cond}$$
(3-12)

(3) As the liquid flow on x-direction is neglected, and substituting $\frac{\partial (\ddot{m}_L h_L)}{\partial z} = \ddot{m}_L \frac{\partial h_L}{\partial z} + h_L \frac{\partial \ddot{m}_L}{\partial z}$, Eq.(3-4) can be reduced into,

$$\ddot{m}_L \frac{\partial h_L}{\partial z} + h_L \frac{\partial \ddot{m}_L}{\partial z} = \ddot{m}_{cond} h_{fg} - U a_w (T_L - T_a) - U_L a_w (T_L - T_{pack})$$
(3-13)

$$C_p \left(T_L \frac{\partial \ddot{m}_L}{\partial z} + \ddot{m}_L \frac{\partial T_L}{\partial z} \right) = \ddot{m}_{cond} h_{fg} - U a_w (T_L - T_a) - U_L a_w (T_L - T_{pack})$$
(3-14)

$$\frac{\partial T_L}{\partial z} = \frac{1}{C_p m_L} \left[\frac{\partial m_L}{\partial z} (h_{fg} - h_L) - U a_w (T_L - T_a) - U_L a_w (T_L - T_{pack}) \right]$$
(3-15)

(4) The gas flow component on z-direction is neglected, i.e., $\frac{\partial (\ddot{m}_a h_a + \ddot{m}_v h_v)}{\partial z} \approx 0$.

Therefore, the energy equation on the gas side is given by

$$-\ddot{m}_{a}\frac{\partial h_{a}}{\partial x}-h_{v}\frac{\partial \ddot{m}_{v}}{\partial x}-\ddot{m}_{v}\frac{\partial h_{v}}{\partial x}=\ddot{m}_{cond}h_{fg}-U_{G}(a-a_{w})\left(T_{pack}-T_{a}\right)-Ua_{w}\left(T_{L}-T_{a}\right)$$

$$T_{a}$$

(5) The temperature of vapor and air are the same as they are well mixed, therefore

$$-\ddot{m}_{a}C_{pa}\frac{\partial T_{a}}{\partial x}-h_{v}\ddot{m}_{a}\frac{\partial \omega}{\partial x}-\ddot{m}_{v}C_{pv}\frac{\partial T_{a}}{\partial x}$$

$$=\ddot{m}_{cond}h_{fg}-U_{G}(a-a_{w})(T_{pack}-T_{a})-Ua_{w}(T_{L}-T_{a})$$
(3-17)

In the above equation, $\omega = \frac{\ddot{m}_v}{\ddot{m}_a}$, and \ddot{m}_a is considered as constant.

(6) Let $C_{Pmix} = \frac{\ddot{m}_a}{\ddot{m}_a + \ddot{m}_v} C_{pa} + \frac{\ddot{m}_v}{\ddot{m}_a + \ddot{m}_v} C_{pv}$, then finally Eq.(3-17) can be written as,

$$\frac{\partial T_a}{\partial x} = \frac{1}{C_{Pmix}(1+\omega)\ddot{m}_a} \left[-\ddot{m}_a \frac{\partial \omega}{\partial x} (h_v - h_{fg}) + U_G(a - a_w) (T_{pack} - T_a) + Ua_w (T_L - T_a) \right]$$

$$(3-18)$$

The temperature of the liquid can be also expressed as,

$$\frac{\partial T_L}{\partial z} = \frac{1}{C_p \ddot{m}_L} \left[-\frac{\partial \omega}{\partial x} \left(h_{fg} - h_L \right) - U a_w (T_L - T_a) - U_L a_w \left(T_L - T_{pack} \right) \right] \tag{3-19}$$

For an air/vapor mixture, the humidity ratio ω can be written as

$$\omega = \frac{0.622 \phi P_{sat}(T_a)}{P - \phi P_{sat}(T_a)} \tag{3-20}$$

Eq. (3-20) is derived using the assumption that air and water vapor are ideal gases. The pressure of saturated air can be calculated from the following empirical equation

$$P_{sat}(T) = a \exp(bT - cT^2 + 3dT^3)$$
 (3-21)

where a=0.611379(Pa), b=0.0723669 (1/°C), c=2.78793x10⁻⁴ (1/°C²), d=6.766138x10⁻⁷ (1/°C³), P_{sat} is the saturation pressure in Pa, and temperature is at °C. Based on Li et al. [17], the gradient of humidity ratio can be obtained by differentiating Eq.(3-20) with T_a and combining with Eq.(3-21), then

$$\frac{\partial \omega}{\partial x} = \frac{\partial T_a}{\partial x} \frac{P}{P - P_{sat}(T_a)} \omega (b - 2cT_a + 3dT_a^2)$$
 (3-22)

3.5 Heat and Mass Transfer Coefficient

Correlations are used to estimate the heat transfer coefficient of the liquid and gas side [67]. The Nusselt number on the liquid side is given by an analogy with the Sherwood number, i.e.

$$\frac{Nu_L}{Pr^{0.5}} = \frac{Sh_L}{Sc_I^{0.5}} \tag{3-23}$$

and the overall heat transfer coefficient of the liquid is

$$U_L = k_L (\rho_L C_{PL} K_L / D_L)^{(1/2)}$$
(3-24)

The heat transfer coefficient of gas side is obtained from an analogy between the Nusselt and Sherwood numbers, i.e., and the overall heat transfer coefficient of the gas is

$$\frac{Nu_G}{Pr^{0.33}} = \frac{Sh_G}{Sc_L^{0.33}} \tag{3-25}$$

and the overall heat transfer coefficient of the gas is

$$U_G = k_G (\rho_G C_{Pmix})^{(\frac{1}{3})} ((\frac{K_G}{D_G})^{(\frac{2}{3})})$$
(3-26)

Finally, from Eq.(3-24) and Eq.(3-26), the overall heat transfer coefficient can be calculated as below:

$$U = (U_L^{-1} + U_G^{-1})^{-1} (3-27)$$

In the above equations, k is mass transfer coefficient of liquid and air/vapor side. Klausner et al. [18] and Alnaimat et al. [19] used. Onda's correlation [67] to evaluate the mass Transfer coefficient. Onda's relation is widely used in determining mass transfer coefficients related to packed bed [68].

3.6 Solving Systems of Partial Differential Equations

The finite differences method was used to solve the Eq.(3-18),Eq.(3-19), and Eq.(3-22) using MATLAB as a platform. A Gauss-Seidel iterative method was used solve the systems of the equations [69]. The Gauss Seidel method uses a relative approximate error, after each iteration, to determine if it is maintaining the criteria of pre-specified tolerance. The tolerance criteria in this method have been kept to 10⁻⁴ to ensure accuracy of the method. A similar procedure is found in Kloppers [70] to solve a system of partial differential equations for cross flow evaporator in cooling towers. A uniform grid was developed to generate the mesh. Eqs.(3-18), (3-19)and (3-20) are coupled and were solved for the temperature of liquid and gas phases, and the humidity ratio.

To ensure the accuracy of the computational results, a grid sensitivity study was performed with 21x21 nodes, 51x51 nodes, 101x101, 151x151 nodes. It can be observed from

Table 3-1 that increasing nodes above 101x101 results in only about 0.1% difference in the outlet temperature of the air, and around 0.073 % for that of outlet liquid temperature. Therefore, simulations were conducted using mesh with 101x101 nodes.

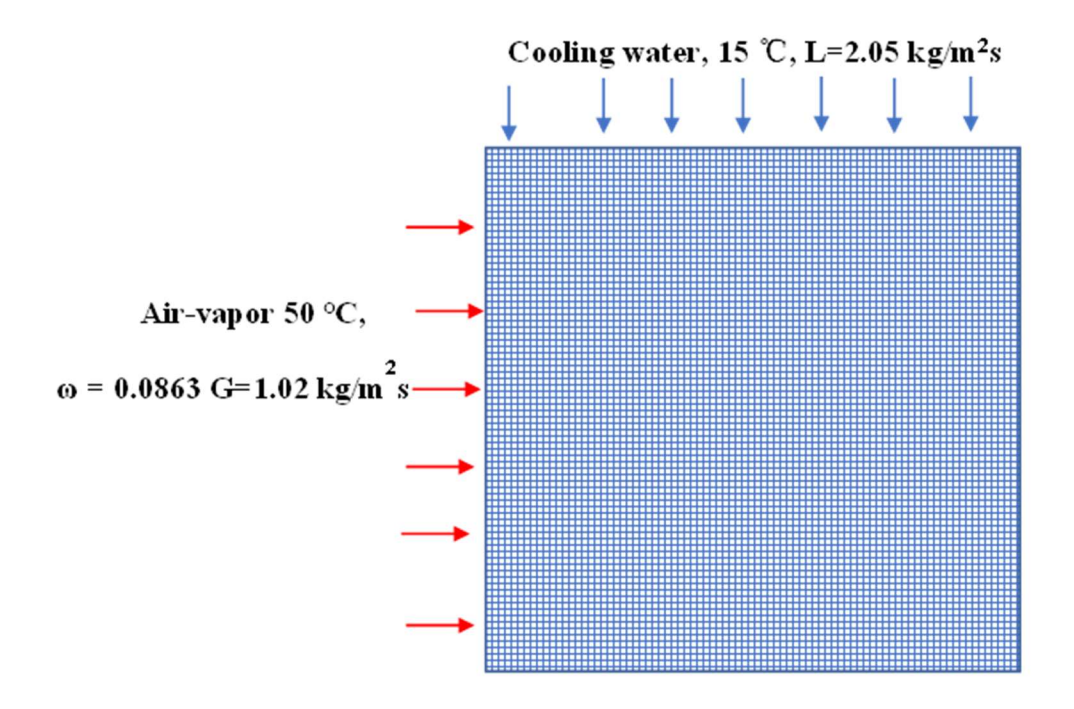


Figure 3-5. Specified boundary conditions for liquid and air streams for the case used to study convergence of the numerical method

Table 3-1. Summary of mesh independence study for liquid mass flux $2.05 kg/m^2s$ and air mass flux $1.02 kg/m^2s$, $T_{L,in} = 15$ °C and $T_{a,in} = 50$ °C

Mesh size	Liquid outlet temperature (°C)	Air outlet temperature (°C)
21x21	28.83	40.81
51x51	27.33	39.52
101x101	27.12	39.20
151x151	27.10	39.24

Figure 3-6 represents how liquid temperature, air temperature, and humidity ratio changes throughout the computational domain for the conditions stated in the caption.

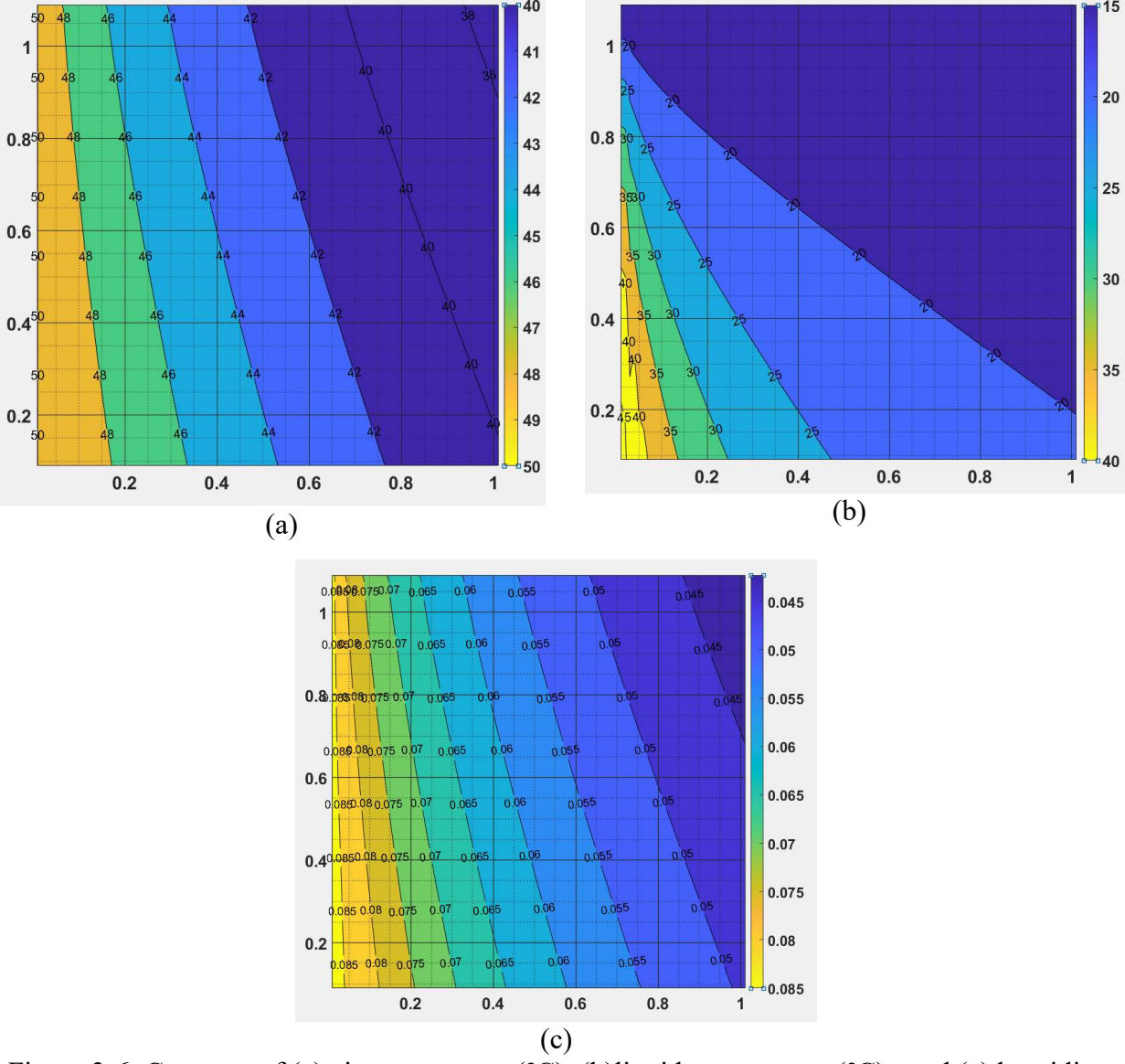


Figure 3-6. Contours of (a) air temperature (°C); (b)liquid temperature (°C); and (c) humidity ratio (kg/kg) are shown above for a liquid mass flux of $2.05 \text{kg/m}^2\text{s}$ and air mass flux of $1.02 \text{kg/m}^2\text{s}$, $T_{L,in} = 15 \text{ °C}$ and $T_{a,in} = 50 \text{ °C}$

3.7 Counterflow Direct Contact Condenser

The mathematical formulation of a transient counterflow direct contact condenser and experimental results were provided by Alnaimat et al.[19]. The steady-state equations of the temperatures of the air, water, and humidity ratio are briefly repeated below:

$$\frac{\partial T_a}{\partial z} = \frac{\partial \omega}{\partial z} \frac{h_v(T_a) - h_{fg}(T_a)}{(1+\omega)C_{pmix}} \ddot{m}_a + \frac{Ua_w(T_L - T_a)}{(1+\omega)\ddot{m}_a C_{pmix}} + \frac{U_G(a - a_w)(T_{pack} - T_a)}{(1+\omega)\ddot{m}_a C_{pmix}}$$
(3-28)

$$\frac{\partial T_L}{\partial z} = \frac{\partial \omega}{\partial z} \frac{(h_{fg} - h_L)\ddot{m}_a}{\ddot{m}_L C_{PL}} - \frac{Ua_w(T_L - T_a)}{\ddot{m}_L C_{PL}} - \frac{U_L a_w(T_L - T_{pack})}{\ddot{m}_L C_{PL}}$$
(3-29)

$$\frac{\partial \omega}{\partial z} = \frac{\partial T_a}{\partial z} \frac{P}{P - P_{sat}(T_a)} \omega (b - 2cT_a + 3dT_a^2)$$
(3-30)

where
$$a=0.611379[Pa]$$
, $b=0.0723669(1/{}^{\circ}C)$, $c=2.78793x10^{-4}$ $(1/{}^{\circ}C^{2})$,

d=6.766138x 10^{-7} (1/°C³), P_{sat} is the saturation pressure, and temperature is in °C. Alnaimat et al. [19] solved these numerically and built an experimental setup for validation. Both experimental results and numerical solutions were found to have a good match.

3.7 Comparative Study of Counterflow and Crossflow condenser

The performance of both counterflow and crossflow condensers are compared in this section. The computational domains were kept at the same size. The inlet condition of water temperature, air temperature, and humidity ratio were also kept the same. The experimental data for inlet liquid mass flux 2.05 kg/m²s ,inlet air mass flux 1.02kg/m²s and inlet liquid mass flux 2.05 kg/m²s ,inlet air mass flux 0.5 kg/m²s were extracted from the work of Alnaimat et al.[19]. For the first case, the liquid mass flux at the inlet is 2.05 kg/m²s, and the air mass flux at the inlet is 1.02kg/m²s. Other cases studied for different inlet conditions are described in Table 3-2.

Table 3-2. Inlet conditions used for comparing computational with experimental results for a liquid mass flux 2.05kg/m²s and air mass flux 1.02 kg/m²s

Case Number	Air Temperature (°C)	Liquid Temperature (°C)	Humidity Ratio
1	24	15.58	0.0191
2	29	15.09	0.0259
3	32	15.11	0.031
4	35	15.31	0.037
5	38	15.60	0.044
6	40	16.23	0.0494
7	41	16.5	0.0523
8	46	16.5	0.0693
9	48	16.92	0.0779
10	49.5	17.27	0.0848
11	50	17.5	0.0872
12	50.5	17.89	0.0897
13	51.5	18.23	0.0949
14	52.5	18.23	0.1004
15	53	18.57	0.1033
16	53.5	19	0.1063

The analysis was performed with varying inlet conditions and a comparison is shown from Figure 3-7. Comparison between computed outlet liquid temperature vs. experimental counter flow outlet liquid temperature obtained from [19] for different inlet liquid temperatures. The inlet liquid mass flux is 2.05 kg/m2s and the air mass flux is 1.02 kg/m2s. A comparison between crossflow and counterflow condensers was done based on outlet liquid temperature, air temperature, humidity ratio, and water production. Weighted area average of temperature and humidity ratio was taken at the outlet of the domain

$$\frac{\sum_{i=1}^{n} a_i A_i}{\sum_{i=1}^{n} A_i} \tag{3-31}$$

In Eq. (3-31), a_i refers temperature of liquid, air, or humidity ratio in each node at the outlet, A_i is the area of that specified node. The water production rate was calculated for both types of condensers. Water production was calculated using Eq. (3-32) in (kg/s), i.e.

$$m_{cond} = \ddot{m}_a(\omega_{in} - \omega_{out})A_c \tag{3-32}$$

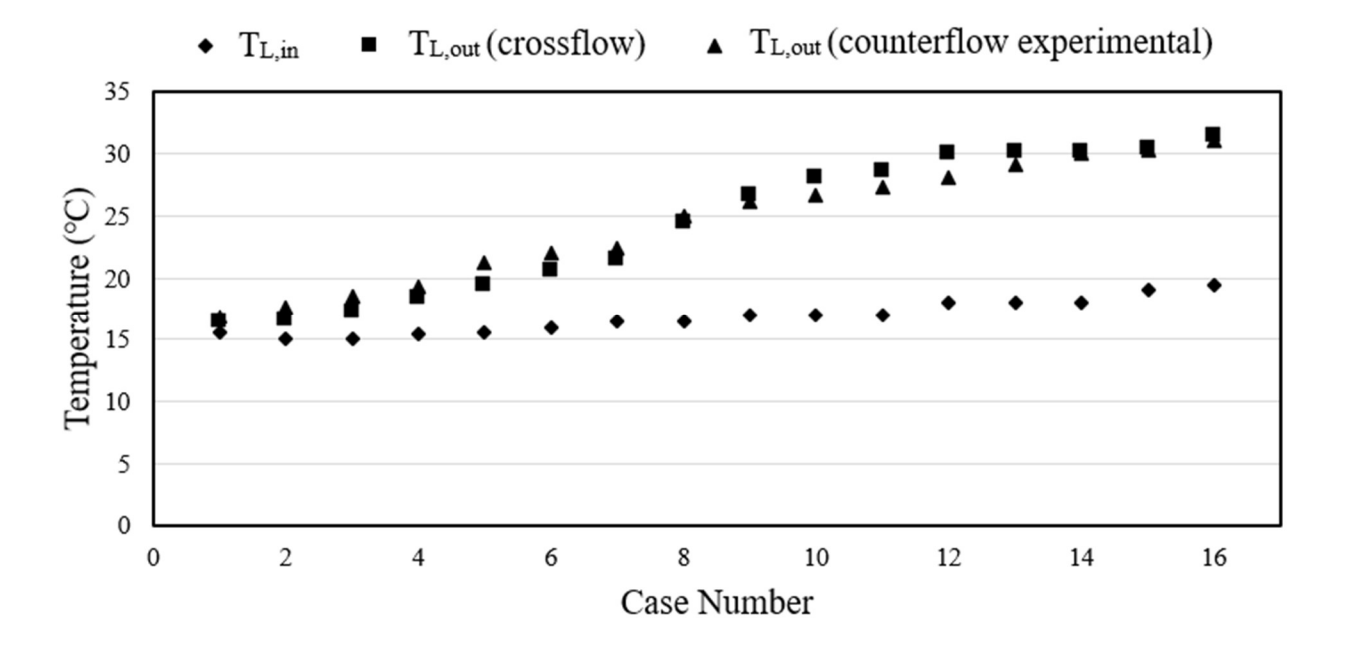


Figure 3-7. Comparison between computed outlet liquid temperature vs. experimental counter flow outlet liquid temperature obtained from [19] for different inlet liquid temperatures. The inlet liquid mass flux is 2.05 kg/m²s and the air mass flux is 1.02 kg/m²s

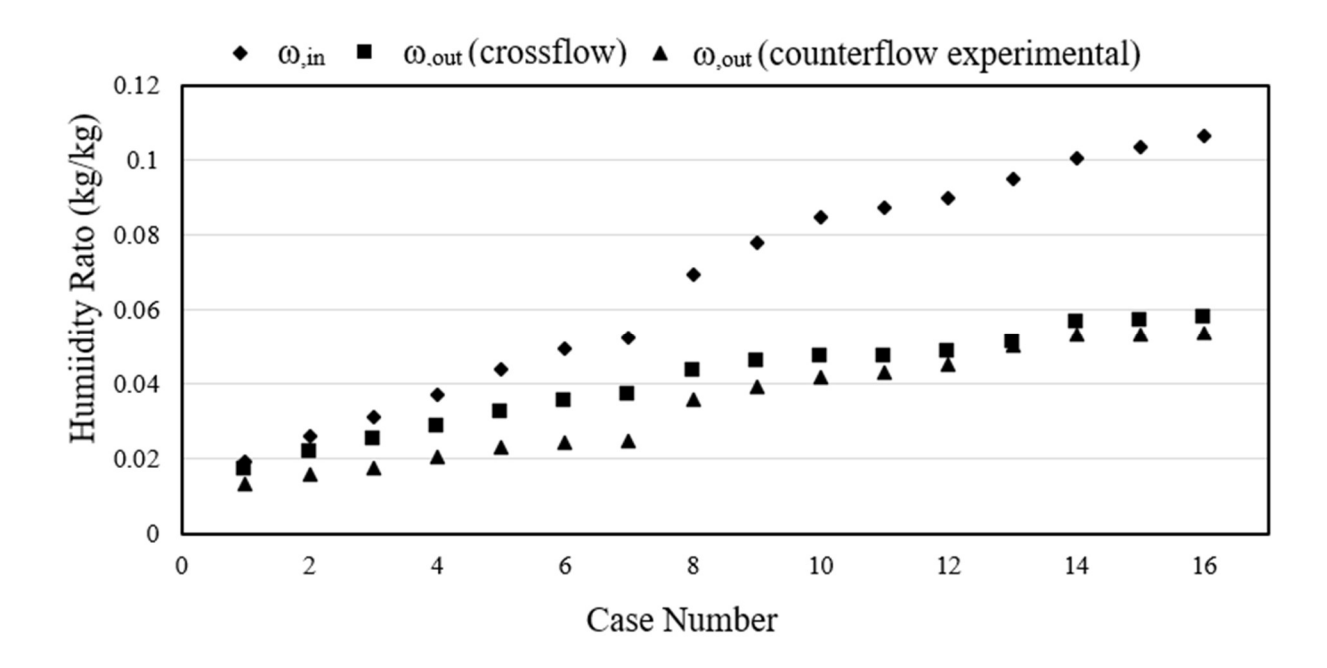


Figure 3-8. Comparison between computed outlet humidity ratio vs. experimental counter flow outlet humidity ratio obtained from [19] for different inlet humidity ratios. The inlet liquid mass flux is 2.05 kg/m²s and the air mass flux is 1.02 kg/m²s

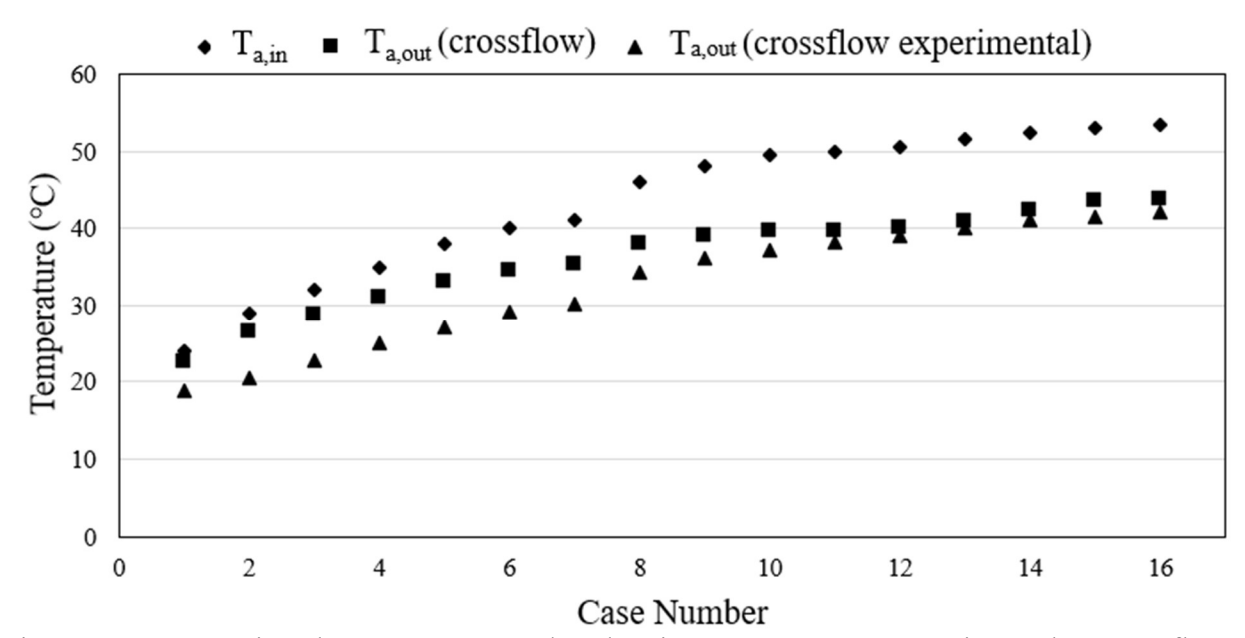


Figure 3-9. Comparison between computed outlet air temperature vs. experimental counter flow outlet air temperature obtained from [19] for different inlet air temperatures. The inlet liquid mass flux is $2.05 \text{ kg/m}^2\text{s}$ and the air mass flux is $1.02 \text{ kg/m}^2\text{s}$

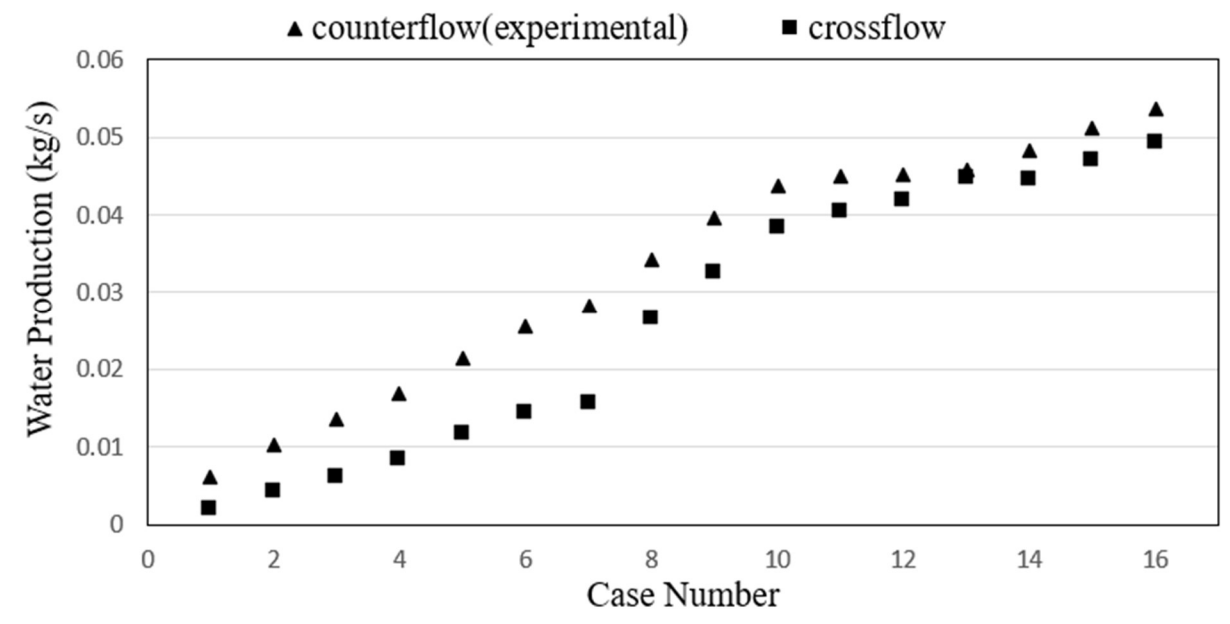


Figure 3-10. Comparative study of the estimated water production, from Eq. (3-32), for cross flow and counter flow direct contact condenser for the liquid mass flux is 2.05kg/m²s and the air mass flux is 1.02 kg/m²s

For the second case considered, the liquid to air mass flux ratio was kept at almost 4 by keeping the liquid mass flux at 2.05 kg/m²s and air mass flux at 0.5 kg/m²s. The conditions studied are found in and the result of the analysis is found in Figure 3-12 to Figure 3-14.

Table 3-3. Inlet conditions used for each case in both computational and experimental study for liquid mass flux 2.05kg/m²s and air mass flux 0.5 kg/m²s

Case Number	Air Temperature (°C)	Liquid Temperature	Humidity Ratio
		(°C)	
1	21.5	14.424	0.0163
2	28	13.351	0.0244
3	31.95	12.96	0.0309
4	36	12.82	0.0392
5	38.6	13.00	0.0456
6	41.3	13.58	0.0532
7	44	14.05	0.0621
8	46.5	13.78	0.0715
9	49	14.12	0.0824

Table 3-3 (cont'd)

10	50	14.39	0.0872
11	51	14.43	0.0923
12	54	14.3	0.1093
13	55	14.3	0.1157
14	57	14.5	0.1334
15	57.5	15.7	0.1297
16	58	16	0.1373

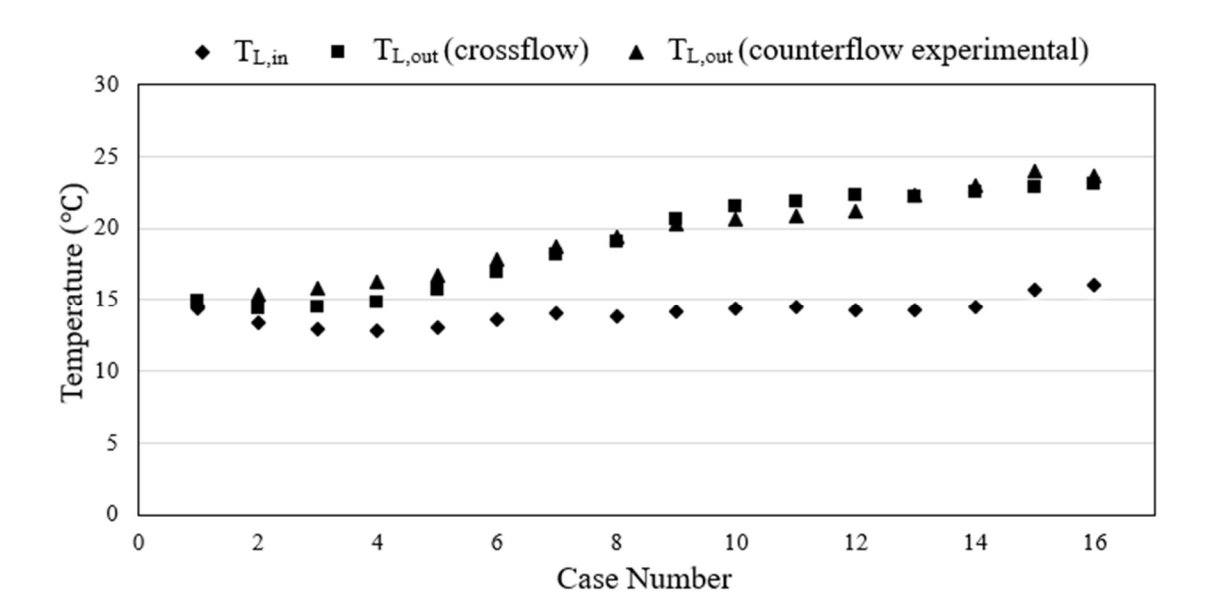


Figure 3-11. Comparison between computed outlet liquid temperature vs. experimental counter flow outlet liquid temperature obtained from [19] for different inlet liquid temperatures. The inlet liquid mass flux is $2.05~{\rm kg/m^2s}$ and the air mass flux is $0.5~{\rm kg/m^2s}$

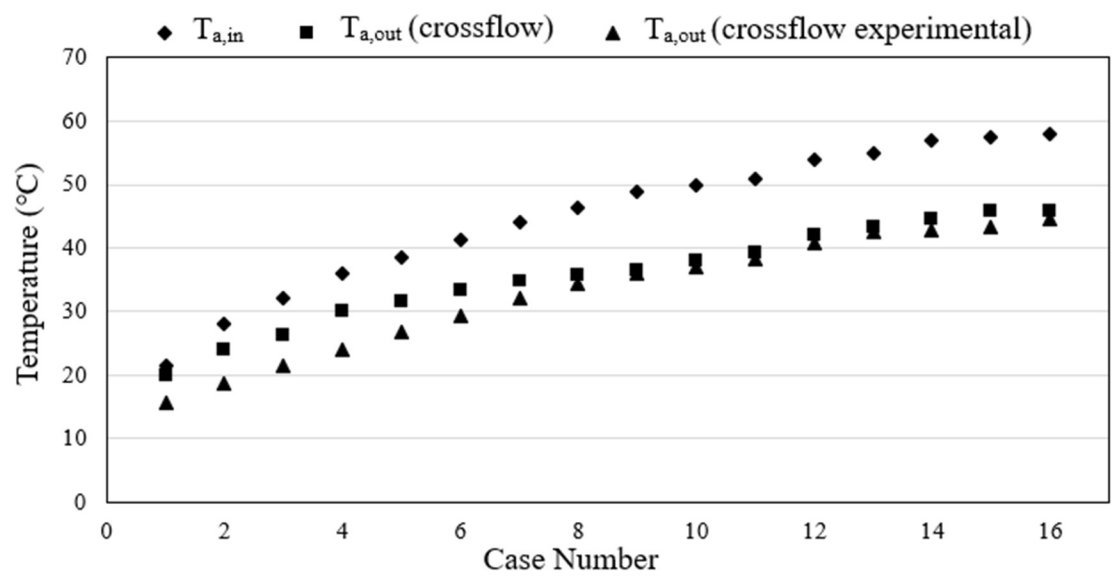


Figure 3-12. Comparison between computed outlet air temperature vs. experimental counter flow outlet air temperature obtained from [19] for different inlet air temperatures. The inlet liquid mass flux is 2.05 kg/m²s and the air mass flux is 0.5 kg/m²s

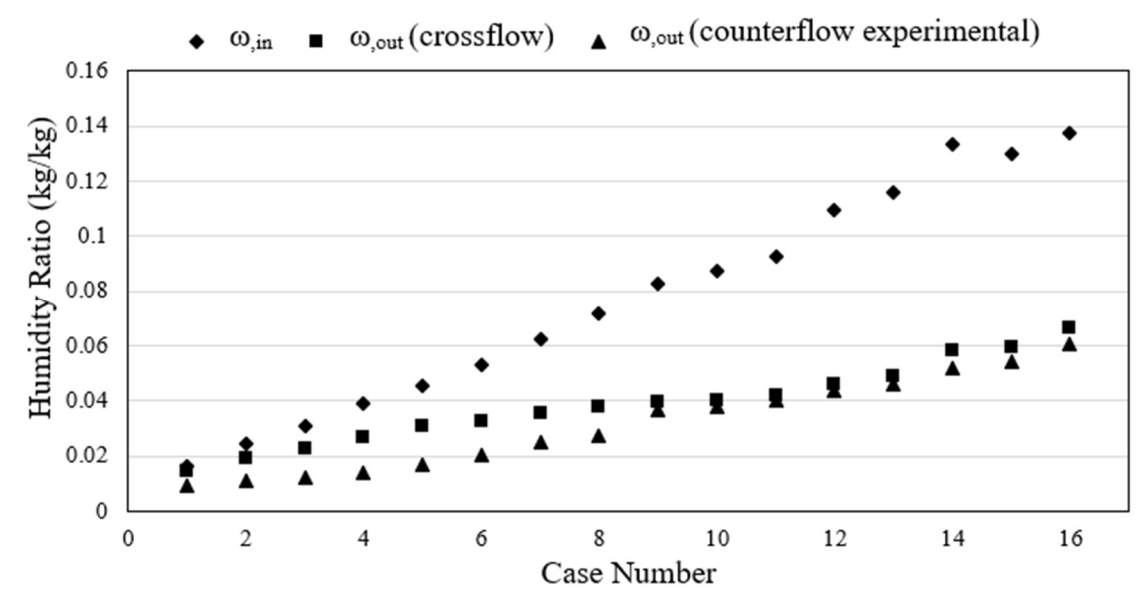


Figure 3-13. Comparison between computed outlet humidity ratio vs. experimental counter flow outlet Humidity ratio obtained from [19] for different inlet humidity ratio. The inlet liquid mass flux is $2.05 \text{ kg/m}^2\text{s}$ and the air mass flux is $0.5 \text{ kg/m}^2\text{s}$

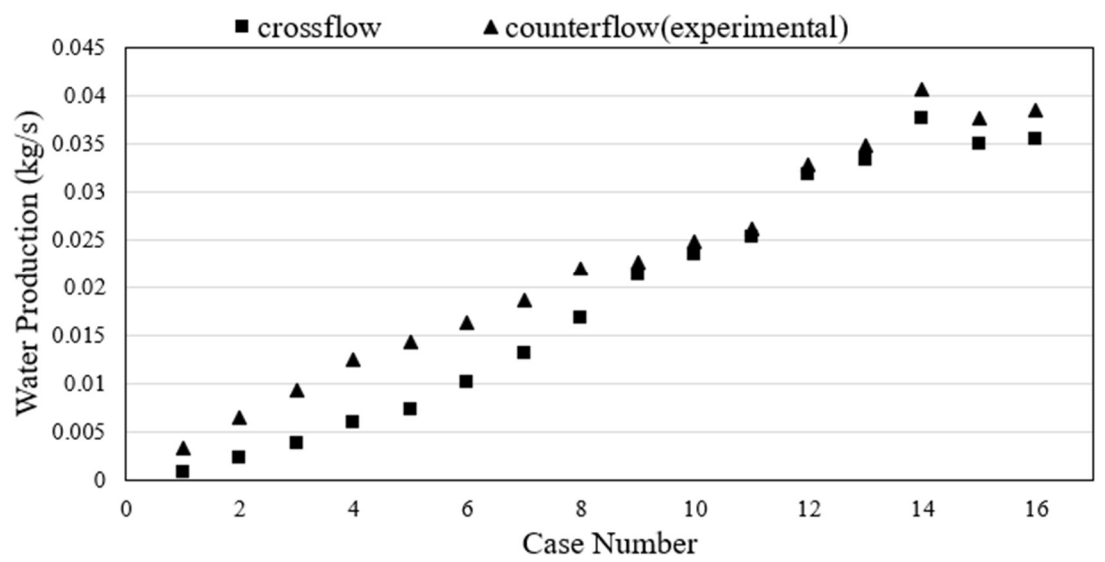


Figure 3-14. Comparative study of the estimated water production, from Eq. (3-32) for cross flow and counter flow direct contact condenser for the liquid mass flux is $2.05 \text{kg/m}^2\text{s}$ and the air mass flux is $0.5 \text{kg/m}^2\text{s}$

In both cases, through Figure 3-14, it can be observed that in most of the cases outlet temperature of the air in counterflow is close to the crossflow results. The same trend can be seen for the humidity ratio. The water production rate mainly depends on the difference between the humidity ratio of inlet and outlet conditions. As the inlet humidity ratio has been kept the same for both cases, the water production rate is dependent on the outlet humidity ratio and air temperature. However, the crossflow direct contact condenser is somewhat less efficient than the counter flow direct contact condenser in some of the specified cases. A probable reason behind the reduced efficiency of the crossflow direct contact condenser is a reduction in the wetted surface area along the gas flow direction. The larger the wetted specific, the more effective is the heat transfer rate between liquid and air. In Figure 3-15, a crossflow direct contact condenser is shown, and the wetted specific area decreases by approximately 12% in the direction of the air/vapor flow. For the case of the counter flow direct contact condenser, the wetted specific area increases from the air/vapor inlet to its outlet, ranging of from 157 m²/m³ to 193 m²/m³ (inlet liquid mass flux 2.05 kg/m²s, air mass flux 1.02 kg/m²s, air temperature 50°C, liquid temperature 15°C) and 157 m²/m³

to 185 m²/m³ (inlet liquid mass flux 2.05 kg/m²s, air mass flux 0.5 kg/m²s, air temperature 50°C, liquid temperature 15°C). As the wetted specific area is decreasing more in the crossflow direct contact condenser than the counterflow direct contact condenser, the overall heat transfer coefficient is also reduced in the crossflow direct contact heat exchanger. The crossflow configuration however requires a simple installation making these configurations attractive.

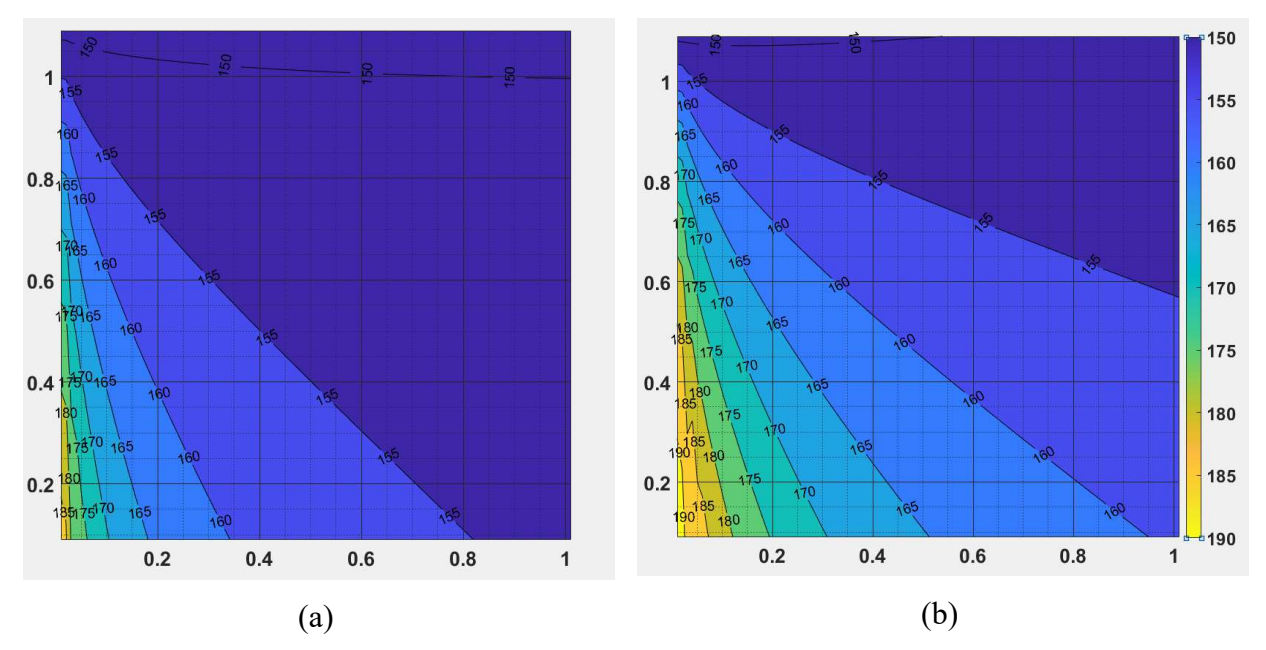


Figure 3-15. Contours of wetted specific area throughout the domain for two different mass fluxes, the values suggest that the crossflow configuration might be less effective for large systems as it reduces toward the exit, (a) liquid mass flux of 2.05 kg/m²s ,air mass flux 0.5 kg/m²s; (b) liquid mass flux 2.05 kg/m²s air mass flux 1.02 kg/m²s

3.8 Conclusion:

A steady-state mathematical model is presented to study heat and mass transfer in direct contact crossflow condensers. The model steady-state heat and mass transfer within a packed for given inlet air, water temperature, and humidity ratio. The equations are solved numerically using the simple Gauss Seidel method. This model is used to evaluate the performance of two different condenser configurations. Though the counterflow direct contact condenser appears slightly more

efficient in the cases studied, the crossflow direct contact condenser offers an attractive alternative due to its increased compactness, and simpler installation. The experimental setup will be used to analyze in detail the proposed mathematical model for crossflow direct contact condenser in some chapters.

CHAPTER 4 : Evaluation of Mass Transfer and Interfacial Area Correlations in Direct Contact Packed Bed: Comparison of Correlations

4.1 Introduction

This chapter I have explained in detail why Onda correlation is used to calculate mass transfer coefficient in packed bed. Choosing the accurate mass transfer coefficient relation and interfacial area correlations is a challenging task. A mathematical model is crucial to predict the performance of the condenser, but existing models contain empirical correlations with a limited or undefined range of validity. In this chapter, a comparison between several mass transfer coefficient correlations for air/vapor and liquid and the interfacial area is performed. An experimental setup has been built and tested for validation purposes. The boundary conditions and experimental data have been compared with the prediction from various listed models. It is concluded from the study that the Onda and Billet correlations are compatible with most of the results obtained from the experimental study. Therefore, to calculate the mass transfer coefficient, Onda correlation has been taken into account throughout the study.

4.2 Variables

a_p	specific area of packing	h_{fg}	vaporization	latent	heat
	material (m^2/m^3)		(kJ/kg)		
a_e	interfacial area (m ² /m ³)	K	thermal condu	ctivity (W	7/mK)
С	constant coefficient	k	mass transfer o	coefficient	(m/s)
D	Molecular diffusion	7	1:: 1	··· (1/2	-)
	coefficient (m ² /s)	L	liquid mass flu	ix (kg/m s	s)
d_c	column internal diameter	Re	Reynold numb	per	
	(m)				

d_h	hydraulic diameter (m)	Sc	Schmidt number		
d_{pe}	diameter of packing	T	Temperature (K or °C)		
	element (m)				
d_p	particle diameter (m)	U	heat transfer coefficient		
			(W/m^2K)		
Fr	Froude number	We	Webber number		
G	air mass flux (kg/m²s)	7	height of packed bed diameter		
		Z_t	(m)		
g	gravity (m/s²)	α	volume fraction		
h	enthalpy (kJ/kg)	ϵ	void fraction of packing		
h_L	liquid holdup (m ³ /m ³)	θ	contact angle (deg)		
ν	kinematic viscosity (m²/s)	μ	dynamic viscosity (kg/ms)		
σ_c	critical surface tension	ρ	density (kg/m³)		
	(N/m)				
ω	humidity				
	Su	bscript			
а	Air	G	Air/Vapor mixture phase		
L	Liquid phase	pack	Packed bed		
v	Vapor phase				

4.3 Experimental Setup

To comparatively study the mass transfer coefficients and interfacial area, an experimental device was set up for a direct contact condenser using a packed bed. Cooling water with a

temperature range of 20-22 °C was sprayed from the top with sprinklers. An "Aquatec" pump was placed to provide the condenser with the desired flow rate around 23 g/s from a water tank to the condenser chamber made of CPVC pipe. The total height of the CPVC pipe was 1 m and 0.5 m of its height was filled with a packed bed. The packed bed was made of a 3D regular array of square printed polycarbonate material. The specific area was 267 m²/m³. The packed bed had an inner diameter of 0.14 m and its effective diameter was 17 mm when orientation was vertical. other properties of packing material include the specific heat capacity are 1.12 kJ/kg K, density is 1200 kg/m³ and the void fraction is 87.8%. Finally, inlet air is pushed through the packed bed. Two valves were used to control flow rate of air. Several type T-type thermocouples were used to measure temperatures at different locations of the condenser. To provide steam, a steam generator was utilized. To prevent heat loss from the setup, the inlet of air vapor has been covered with insulation. A Labjack data acquisition system along with LabVIEW was used for the temperature measurements.

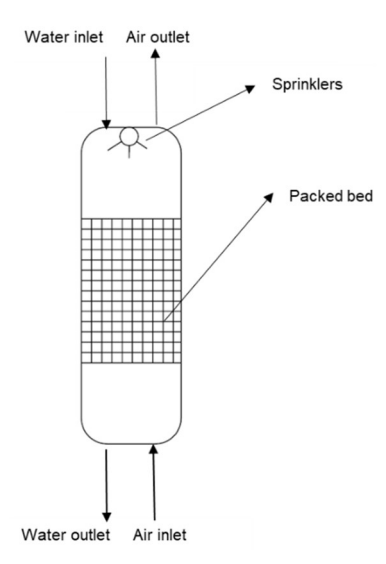


Figure 4-1. Schematic diagram of direct contact counter flow condenser

4.4 . Mathematical Model

The mathematical model is developed by Alnaimat et. al [19] for direct contact packed-bed condensers is presented below:. The important equations are provided in Eqs. (4-1) to (4-3)

$$\frac{\partial T_L}{\partial t} = \frac{L}{\rho_L \alpha_L} \frac{\partial T_L}{\partial z} - \frac{\partial \omega}{\partial z} \frac{G(h_{fg} - h_L)}{\rho_L \alpha_L C p_L} + \frac{U \alpha_w (T_a - T_L)}{\rho_L \alpha_L C p_L} + \frac{U_L \alpha_w (T_{pack} - T_L)}{\rho_L \alpha_L C p_L}$$
(4-1)

$$\frac{\partial T_{a}}{\partial t} = \frac{-G}{\rho_{a}\alpha_{a}} \frac{\partial T_{a}}{\partial z} - \frac{\partial \omega}{\partial z} \frac{G\left(h_{fg}(T_{L}) - h_{v}(T_{a})\right)}{\rho_{a}\alpha_{a}Cp_{G}(1+\omega)} - \frac{U_{G}(\alpha_{p} - \alpha_{w})(T_{a} - T_{pack})}{\rho_{a}\alpha_{a}Cp_{G}(1+\omega)} - \frac{U_{G}(\alpha_{p} - \alpha_{w})(T_{a} - T_{pack})}{\rho_{a}\alpha_{a}Cp_{G}(1+\omega)} - \frac{U_{G}(\alpha_{p} - \alpha_{w})(T_{a} - T_{pack})}{\rho_{a}\alpha_{a}Cp_{G}(1+\omega)}$$
(4-2)

$$\frac{\partial T_{\text{pack}}}{\partial t} = \frac{1}{\rho_{\text{pack}} \alpha_{\text{pack}} C p_{\text{pack}}} \left(U_{\text{G}} (a_{\text{p}} - a_{\text{w}}) (T_{\text{a}} - T_{\text{pack}}) - U_{\text{L}} a_{\text{w}} (T_{\text{pack}} - T_{\text{L}}) \right) \tag{4-3}$$

Overall heat transfer coefficient for gas and liquid could be calculated through Eqs.(4-4) to (4-6)

$$U_L = k_L \left(\rho_L C_{PL} \frac{K_L}{D_L} \right)^{1/2} \tag{4-4}$$

$$U_G = k_G (\rho_G C_{PG})^{1/3} \left(\frac{K_G}{D_G}\right)^{2/3}$$
 (4-5)

$$U = \left(\frac{1}{U_L} + \frac{1}{U_G}\right)^{-1} \tag{4-6}$$

A focus of this study is comparing various correlations for mass transfer coefficient and interfacial area and the possibility of validation to experiment result for the direct contact packed-bed condenser. In this study, we considered mass transfer correlation developed by Onda et. al. (Eqs. (4-7)- (4-8)) [71], Van Krevelen et al. (Eqs. (4-9) - (4-10))[72], Shi et al. (Eqs. ((4-11) - (4-12))[73], Billet et al. (Eqs. (4-13) - (4-14))[74], and Zech et al. (Eqs. (4-15) - (4-16)) [75]. In addition, the various correlation for the interfacial area was investigated to see the impact of interfacial area value on the simulation's result. These correlations are suggested by Onda et. al.

(Eq. (4-17)) [71], Puranik et al. (Eq. (4-18))[76], Kolev et al.(Eq (4-19)) [77], Bravo et al. (Eq. (4-20)) [78], and Billet et al. (Eq. (4-21)) [74]. These equations are mentioned below:

$$k_L = \frac{0.0051}{\left(a_p d_p\right)^{-0.4}} \left(\frac{\mu_L g}{\rho_L}\right)^{1/3} \left(\frac{\rho_L u_L}{a_e \mu_L}\right)^{2/3} S c_L^{-0.5}$$
(4-7)

$$k_G = c_G \left(\frac{D_G}{a_p d_p^2}\right) \left(\frac{\rho_G u_G}{a_p \mu_G}\right)^{0.7} S c_G^{1/3}$$
(4-8)

$$k_{L} = 0.015 \frac{D_{L}}{\left[\frac{\mu_{L}^{2}}{(\rho_{L}^{2}g)}\right]^{1/3}} \left(\frac{\rho_{L}u_{L}}{a_{e}\mu_{L}}\right)^{\frac{2}{3}} Sc_{L}^{1/3}$$
(4-9)

$$k_G = 0.2 \frac{D_G}{d_c} \left(\frac{\rho_L u_L}{a_v \mu_L} \right)^{0.8} S c_G^{1/3}$$
 (4-10)

$$k_L = 0.86 \sqrt{\frac{6D_L}{\pi d_{pe}}} \sqrt{\frac{u_L^{1.2} g^{1.3} \sigma_L^{0.3} \epsilon^{1.2} (1 - 0.93 \cos \theta)^2}{v_L^{1.4} \rho_L^{0.3} a_p^{2.4}}}$$
(4-11)

$$k_G = c_G \frac{D_G}{d_{ne}} \left(\frac{\rho_G u_G d_{pe}}{\mu_G}\right)^{2/3} S c_G^{1/3}$$
(4-12)

$$k_{L} = c_{L} \left(\frac{\rho_{L} g}{\mu_{L}}\right)^{1/6} \left(\frac{D_{L}}{d_{h}}\right)^{0.5} \left(\frac{u_{L}}{a_{p}}\right)^{1/3}$$
(4-13)

$$k_G = c_G \frac{a_p^{0.5} D_G}{\sqrt{d_p(\epsilon - h_I)}} \left(\frac{\rho_G u_G}{a_p \mu_G}\right)^{3/4} S c_G^{1/3}$$
(4-14)

$$k_{L} = c_{L} \sqrt{\frac{6D_{L}}{\pi d_{pe}}} \left(\frac{\rho_{L} g d_{pe}^{2}}{\sigma_{L}}\right)^{-0.15} \left(\frac{u_{L} g d_{pe}}{3}\right)^{1/6}$$
(4-15)

$$k_G = c_G \frac{D_G}{d_n} \frac{\epsilon + 0.12}{\epsilon (1 - \epsilon)^{-1}} \left(\frac{\rho_G u_G d_p}{(1 - \epsilon)\mu_G} \right)^{2/3} S c_G^{1/3}$$
(4-16)

$$a_e = a_p \left(1 - exp \left[-1.45 \left(\frac{\sigma_c}{\sigma_L} \right)^{0.75} Re_L^{0.1} Fr_L^{-0.05} We_L^{0.2} \right] \right)$$
 (4-17)

$$a_e = 1.045 a_p \left(\frac{\rho_L u_L}{\mu_L a_p}\right)^{0.041} \left(\frac{\rho_L u_L^2}{\sigma_L a_p}\right)^{0.133} \left(\frac{\sigma_c}{\sigma_L}\right)^{0.182}$$
(4-18)

$$a_e = 0.583 a_p \left(\frac{\rho_L g}{a_p^2 \sigma_L}\right)^{0.49} \left(\frac{u_L^2 a_p}{g}\right)^{0.196} \left(a_p d_p\right)^{0.42} \tag{4-19}$$

$$a_e = 0.498 a_p \left(\frac{u_L \mu_L}{\sigma_L} \frac{6\rho_G u_G}{a_p \mu_G} \right)^{0.392} \frac{\sigma_L^{0.5}}{Z_t^{0.4}}$$
 (4-20)

$$a_e = 1.5 \left(a_p d_h \right)^{-0.5} \left(\frac{\rho_L u_L d_h}{\mu_L} \right)^{-0.2} \left(\frac{\rho_L u_L^2 d_h}{\sigma_L} \right)^{0.75} \left(\frac{u_L^2}{g d_h} \right)^{-0.45}$$
(4-21)

4.5. Comparison of Results

A finite difference scheme is used to solve the system of equations. A second-order approximation is used for the partial differences in Eqs.(4-1) – (4-3) for the whole domain. The quasi-steady-state assumption is used for simplification. A MATLAB program is developed to calculate various parameters used in the equations and solve the coupled non-linear ordinary differential equations.

4.5.1 Mesh Independency

In the first step, solver dependency on the grid resolution is investigated. Based on Table 4-1 and the negligible change in outlet temperature for different grid resolutions, simulation results are almost independent of the number of nodes.

Table 4-1. Summary of mesh independence study performed for L = 1.4 kg/m²s, G = 0.1 kg/m²s, $T_{L,inlet}$ = 21 °C and $T_{a,inlet}$ = 68 °C

	Nodes number	51	101	201	51	101	201
Interfacial area	Mass transfer	Liquid o	utlet temp	erature	Air out	let tempe	rature
correlation	coefficient	S	imulation		S	imulation	
Onda	Onda	29.98	29.98	29.98	22.23	22.21	22.20
Onda	Van Krevelen	29.10	29.10	29.10	34.75	34.74	34.73
Onda	Shi	29.97	29.97	29.96	22.49	22.47	22.46
Onda	Billet	29.97	29.97	29.97	22.41	22.39	22.39
Onda	Zech	29.98	29.97	29.97	22.38	22.36	22.36
Bravo	Van Krevelen	29.10	29.10	29.10	34.75	34.74	34.73
Puranik	Shi	29.97	29.97	29.96	22.49	22.47	22.46
Kolev	Zech	29.98	29.97	29.97	22.38	22.36	22.36
Billet	Billet	29.97	29.97	29.97	22.41	22.39	22.39

4.5.2 Interfacial Area

To investigate the effect of interfacial area on the resulting temperature, Eqs. (4-17)- (4-18) were used for interfacial area and Eqs. (4-7) - (4-8) was used for the mass transfer coefficient. Figure 4-2 shows variation in the interfacial area across the packed bed. Interfacial area value changes a lot depending on which correlation would be used; however, based on the values in Table 4-2, we can see that the outlet temperature isn't affected by the change in the interfacial area value since the liquid and gas velocity is not that high.

Table 4-2. Outlet temperature values found for different interfacial area correlations

		Liquid outlet	Difference	Air Outlet	Difference
Correlation	Average aw	temperature	for liquid	Temperature	
		simulation (°C)	simulation (°C) (%)		for air (%)
Onda	126.99	29.985		21.654	
Bravo	4.37	29.984	0.003	21.663	0.040
Puranik	81.91	29.985	0.003	21.652	0.051
Kolev	27.45	29.985	0.001	21.653	0.006
Billet	45.86	29.985	0.000	21.653	0.002

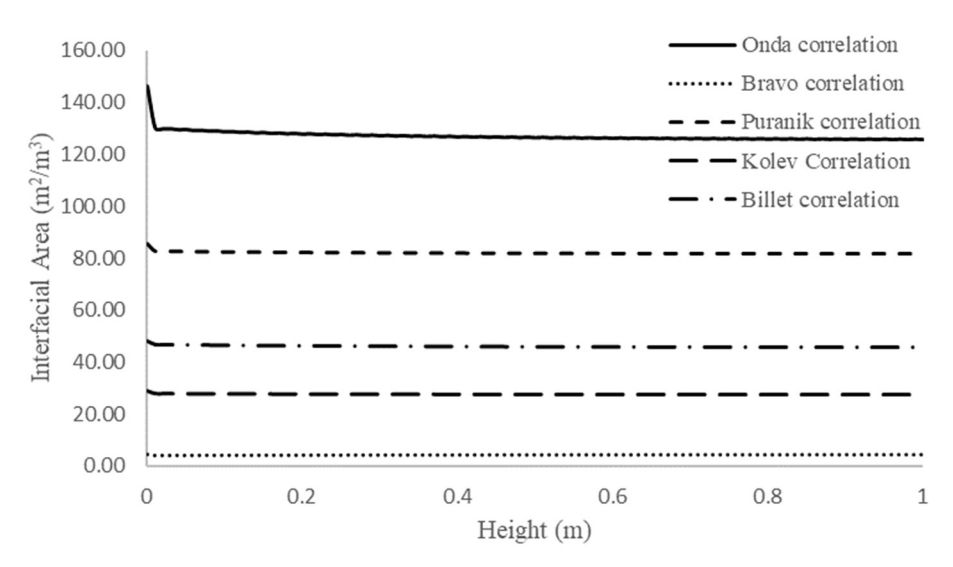


Figure 4-2. Correlation predicts very different values of interfacial area for the packed-Bed column

4.6 Mass Transfer Coefficient

When comparing simulation results with the experiment, it can be noticed that Onda and Billet correlations predict the temperature of air (5% error) and liquid (9% error) more accurately in comparison with others. Furthermore, Shi and Zech correlations aren't as precise as Onda's, but the error for these correlations is within the 10% range. Moreover, Figure 4-3 depicts that Van Krevelen works better for around 50% of the experimental data for liquid, but there is significant error whenever someone makes use of the correlation to predict air temperature which has been

illustrated in Figure 4-4. In addition, it can be observed that as the air temperature at the inlet increases, the error for predicting liquid temperature also rises. Among possible causes of the error include having a non-uniform flow, water bridging, heat losses to the environment for experimental setup, and misrepresentation of packed-bed geometry.

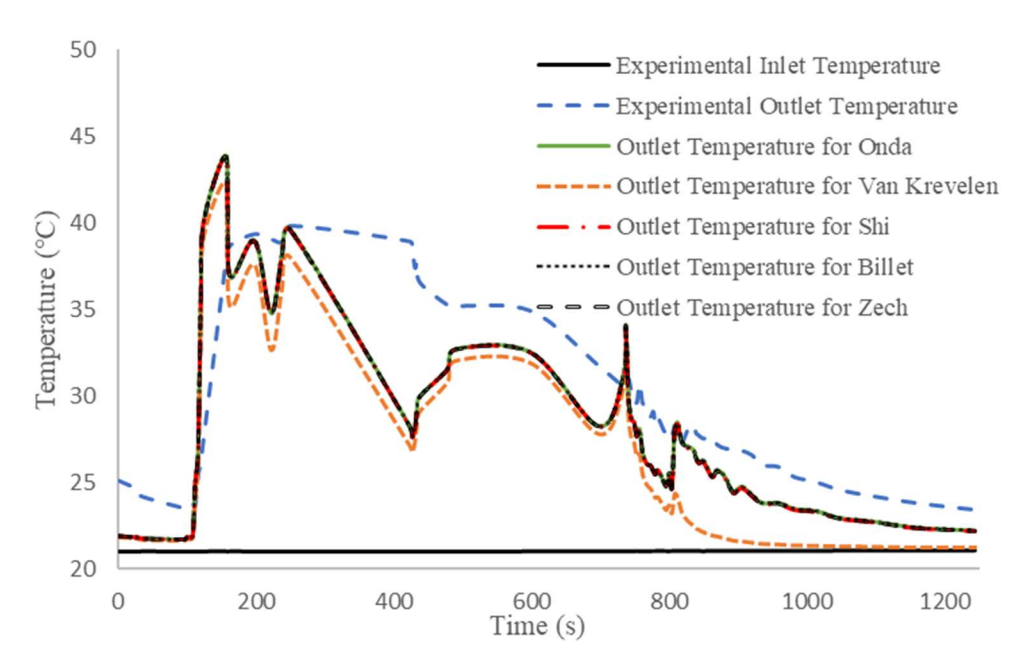


Figure 4-3. Temperature obtained by varying the inlet air temperature (Inlet temperature for water is Constant). Most correlations predicted adequate measured values except for the Van Krevelen correlation

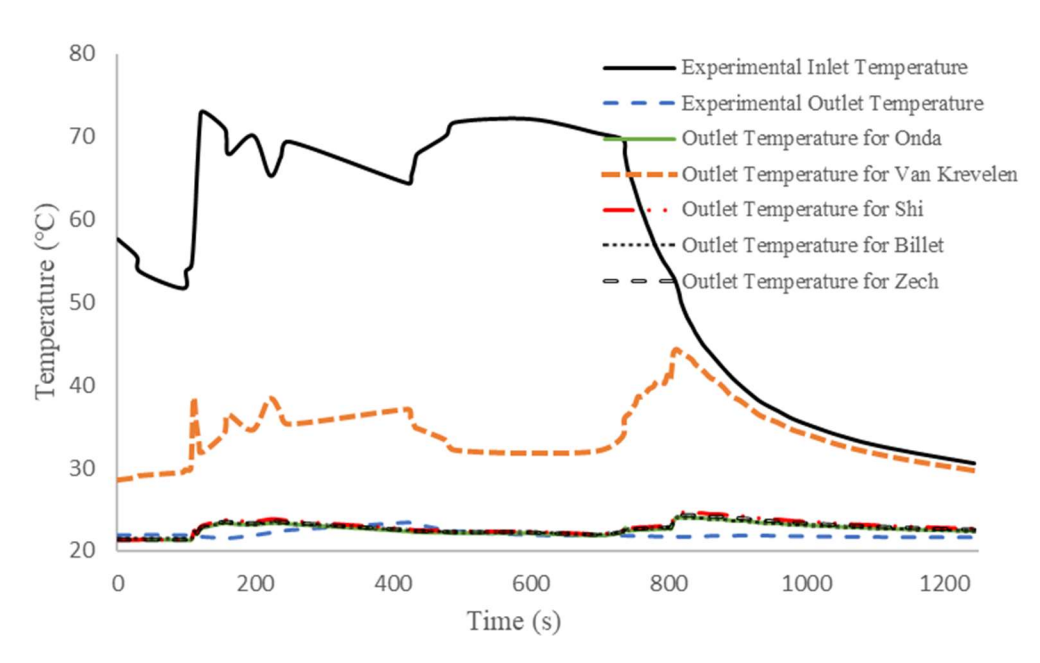


Figure 4-4. Comparison of predicted outlet air temperature with experimental data for varying inlet air temperature. most correlations predicted adequate measured values except for the Van Krevelen correlation

Table 4-3. Average temperature error of gas and liquid for different mass transfer correlation

	Onda	Van Krevelen	Shi	Billet	Zech
% Error for liquid	9.39	14.65	9.49	9.40	9.45
% Error for air	5.15	68.00	6.59	5.42	6.10

4.7 Conclusion

In this chapter, a finite difference scheme was used to solve energy conservation for a packed-bed condenser. The results obtained from the solver conclude that there is still a relatively important uncertainty for the result amongst the considered correlations. Every correlation has a specific limit or range of validity. Also, it can be clearly stated that for the conditions considered, Onda and Billet correlations are the preeminent choices based on the experimental and comparative studies performed. The lack of fitted coefficient in the Van Krevelen coefficient and

the need to fit data to the experiment for the other correlations, highlight the need for the validated coefficient for different packed-bed material microstructure and other parameters needed.

CHAPTER 5 : Optimization of Direct Contact Cross Flow Packed Bed Condenser

5.1 Introduction

A new shape for the packed bed, with a cross-section that increases along with the horizontal air-vapor flow, is proposed to improve performance. A two-dimensional mathematical model is also developed to accommodate the more complex geometry and estimate performance. A cubic system was studied and compared with a wedge geometry in which the cross-section area of air-vapor at the inlet was half of the area at the outlet. Computational results show that, for the same volume of the packed bed, the wedge-shaped crossflow condenser can be more effective in terms of water production. Besides, another study has been done in this chapter using GA (genetic algorithm) to find optimized rectangular shape considering the same mass flux of air/vapor. These analyses can give us a brief idea of building a lab-scale experimental setup.

5.2 Variables

а	specific area of packing material (m ² /m ³)	subsci	ript
C_p	specific Heat(kJ/kg)	mix	mixture
G	Air mass flux (kg/ m ² s)	fg	fluid-gas
m	mass flow rate(kg/s)	v	vapor
h	enthalpy(kJ/kg)	w	wetted area
т	liquid mass flux (kg/m ² s)	а	air/vapor
P	total pressure of the system(kPa)	L	liquid
U	overall heat transfers co-efficient(W/m ² K)	pack	packing material
T	temperature(°C/K)	G	air/vapor
ω	humidity ratio (kg/kg)	С	cold liquid

5.3 Mathematical Model for Wedge Shape

In the following, the system being studied is assumed to be in steady state, with no heat losses, and relative humidity of 100 percent at the inlet. Conservations of mass and energy are used to derive the governing equations. Figure 5-1 represents the control volume for a rectangular control volume. The resulting equations to estimate the temperature of air, liquid water, and the humidity ratio are:

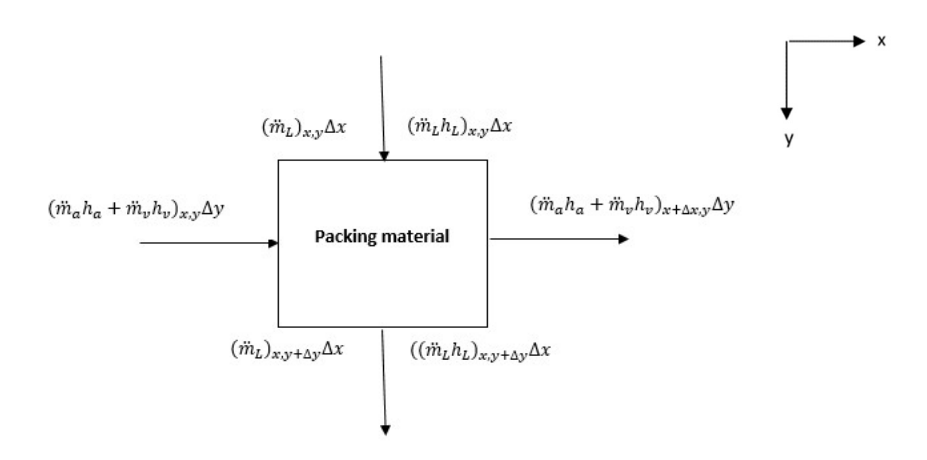


Figure 5-1. Control volume used to derive the equations used for modeling the crossflow packed bed condenser

The resulting equations to estimate the temperature of the air, liquid water, and the humidity ratio are:

$$\frac{\partial T_a}{\partial x} = \frac{1}{C_{Pmix}(1+\omega)\ddot{m}_a} \left[-\ddot{m}_a \frac{\partial \omega}{\partial x} (h_v - h_{fg}) + U_G(a - a_w) (T_{pack} - T_a) + Ua_w (T_L - T_a) \right]$$
 (5-1)

$$\frac{\partial T_L}{\partial y} = \frac{1}{c_p \ddot{m}_L} \left[-\frac{\partial w}{\partial x} (h_{fg} - h_L) - U a_w (T_L - T_a) - U_L a_w (T_L - T_{pack}) \right]$$
 (5-2)

$$\frac{\partial w}{\partial x} = \frac{\partial T_a}{\partial x} \frac{P}{P - P_{sat}(T_a)} \omega (b - 2cT_a + 3dT_a^2)$$
(5-3)

Eqs (5-1), (5-2) and (5-3) have been solved utilizing the Gauss-Seidel finite differences method. The constants are b=0.0723669, c=2.78793x10⁻⁴, d=6.76138x10⁻⁴ in Eq. (5-3). As mass flux of air/vapor changes as cross-sectional area changes from inlet to outlet, to consider the change of mass flux in a wedge shape, a new equation has been introduced,

$$\ddot{m}_{a} = \left[\left(\frac{Area_{inlet}}{Area_{outlet}} - 1 \right) * x + 1 \right] * \ddot{m}_{a,inlet}$$
(5-4)

Other vital parameters such as U_G , U, U_L are found in Eckert and Goldstein [79]. The results obtained are for the following variables: temperature of the air, liquid, and humidity ratio in the entire domain. Water production and effectiveness can be calculated using

$$m_{cond} = m_{a,in} * \omega_{in} - m_{a,out} * \omega_{out}$$
 (5-5)

$$\varepsilon = \frac{\omega_{in} - \omega_{out}}{\omega_{in} - \omega_{sink}} \tag{5-6}$$

Where $m_{a,in}$ and $m_{a,out}$ are the inlet of mass flow rate(kg/s) and outlet of mass flow rate(kg/s) respectively. The effectiveness is defined here as the ratio of actual production to the theoretical maximum possible production. The outlet humidity ratio has been calculated using the area-weighted average. In Eq. (5-6), ω_{sink} is assumed to be the humidity ratio of the inlet of liquid temperature as it is the minimum possible humidity ratio in the system.

5.4 . Effect of Packed Bed Shape

A wedge-shape condenser has been considered in solving the above equations in which the cross-section increases in the air flow direction, as shown in Figure 5-2. Four cases have been analyzed to identify if a wedge shape condenser can be more effective than a regular shape direct contact crossflow condenser:

Case 1: maintaining the same mass flux at the inlet of air/vapor. (Inlet air mass flux =1.02 kg/m²s, Inlet liquid mass flux=2.05 kg/m²s, inlet air temperature = 50°C and inlet liquid temperature= 15°C)

Case 2: maintaining same mass flow rate at the inlet of air/vapor and the same volume of packing (inlet air mass flow rate =0.306 kg/s, inlet liquid mass flux =2.05 kg/m²s, inlet air temperature = 50°C and inlet liquid temperature= 15°C)

Case 3: maintaining the same mass flux at the inlet of air/vapor. (Inlet air mass flux =0.5 kg/m²s, Inlet liquid mass flux=2.05 kg/m²s, inlet air temperature = 50°C and inlet liquid temperature= 15°C)

Case 4: maintaining same mass flow rate at the inlet of air/vapor and the same volume of packing (inlet air mass flow rate =0.15kg/s, inlet liquid mass flux =2.05 kg/m²s, inlet air temperature = 50°C and inlet liquid temperature= 15°C)

To ensure the accuracy of the computational results, a grid independence study has been also performed for case 1. Seen from Table 5-1 increasing nodes above 101x101 results in only about 0.13 % difference in the outlet temperature of the air, and around 0.1% for that of outlet liquid temperature. Further simulations were thus conducted using 101x101 nodes.

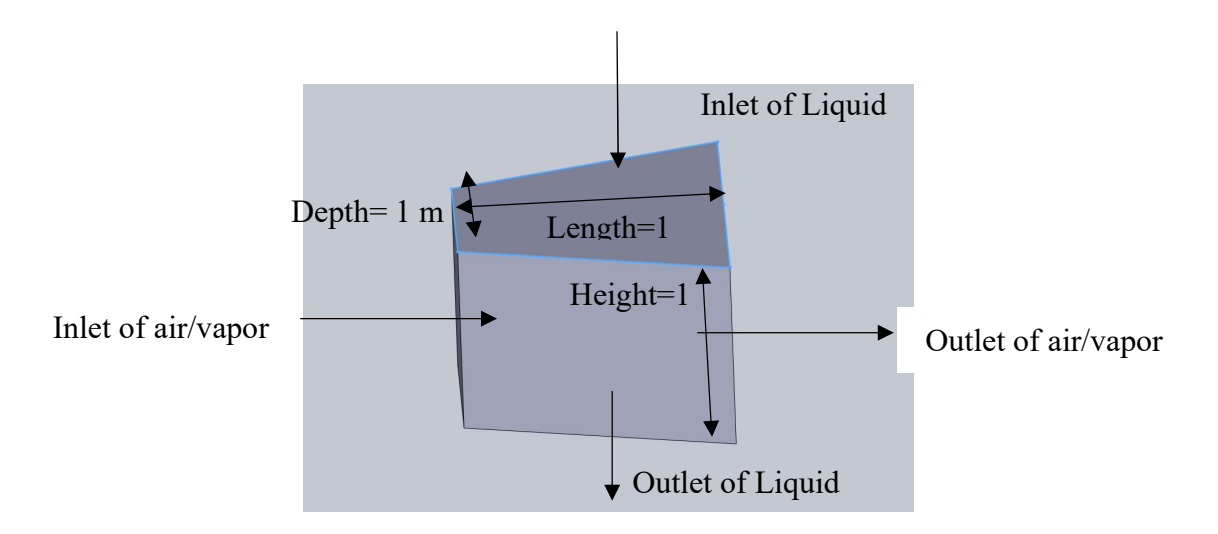


Figure 5-2. A simplified diagram of wedge shape packed bed condenser

Table 5-1. Summary of mesh independence study for case 1 study, boundary conditions at the inlet $\ddot{m}_1 = 2.05 \text{kg/m}^2 \text{s}$, $\ddot{m}_2 = 1.02 \text{ kg/m}^2 \text{s}$ and, $\ddot{m}_3 = 1.02 \text{kg/s}$, $\ddot{T}_{\text{Liplet}} = 15 \,^{\circ}\text{C}$ and $\ddot{T}_{\text{a inlet}} = 50 \,^{\circ}\text{C}$

mict me 2.03kg/m	. 5, 111 _a	1.02 Kg/	m s and, m	a 1.02Kg/3	, L,iniet	15 C t	ind ra,iniet	30 C
Nodes number	21x21	51x51	101x101	151x151	21x21	51x51	101x101	151x151
Area _{inlet} /Area _{outlet}	Liquid	outlet te	mperature(C)	Air out	let tempe	erature(°C)	
0.5	26.34	25.28	24.91	24.91	39.41	38.24	37.85	37.90
0.6	26.99	25.88	25.50	25.50	39.82	38.64	38.26	38.31
0.7	27.57	26.41	26.00	25.99	40.16	38.97	38.57	38.63
0.8	28.05	26.84	26.42	26.42	40.42	39.22	38.88	38.84
0.9	28.47	27.22	26.80	26.79	40.63	39.44	39.10	39.10
1	28.83	27.33	27.12	27.10	40.81	39.52	39.20	39.26

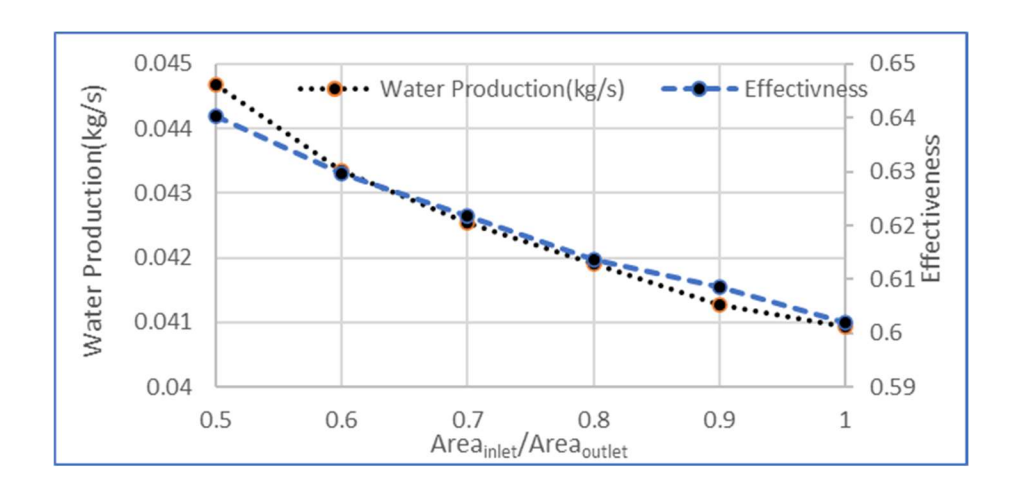


Figure 5-3. Effectiveness and water production of condenser for different wedge shapes for case $1 \ (\ddot{m}_L = 2.05 \ \text{kg/m}^2\text{s}, \ \ddot{m}_a = 1.02 \ \text{kg/m}^2\text{s})$

Figure 5-3 shows that effectiveness and water production increase as ratio of inlet and outlet area goes down to 0.5. The effectiveness increases for case 1 around 9-10 percent if a wedge shape direct contact condenser is used in a system with the same air mass flow rate. In wedge shape direct contact condenser, the mass flux of air/vapor decreases from inlet to outlet due to the increasing cross section. On the other hand, the liquid mass flux is maintained at the inlet vertically. Thus, the total mass flow rate of liquid at the inlet is higher for cases with lower ratio of inlet and outlet areas because of larger cross section areas. Besides, wedge shape packed bed has a higher

volume hence more contact area than a rectangular cuboid due to the new geometry. All above factors together yield in higher effectiveness and water production than a cubic crossflow condenser for Case 1.

Table 5-2 suggests that if the same volume of packing material is considered, having a depth at the inlet of 0.3 m and at the outlet of 1.7 m, length of 1m, and height of 1m, compared with a rectangular cuboid shape with dimensions of 1 m³ and same mass flow rates, then the wedge shape direct contact crossflow condenser has better water production and effectiveness.

Table 5-2. Performance comparison for case 2. The boundary conditions for inlet air mass flow rate were 0.306 kg/s, and the inlet liquid mass flux was 2.05 kg/m²s

	Wedge =1m ³)	Shape	(Volume	Regular shape (Volume = 1 m ³)
Liquid Temperature (°C)		21.553		19.762
Air Temperature(°C)		34.90		35.8
Humidity Ratio (kg/kg)		0.0363		0.0377
Water Production (kg/s)		0.0153		0.01487
Effectiveness		0.66		0.64

Case 3 is as same as case 1. The mass flow rate of case 3 is 0.51kg/s. From Figure 5-4, it can be depicted that effectiveness and water production improves around 6-7 percent. Therefore, it can be expected that geometric change has a great influence on improvement in system

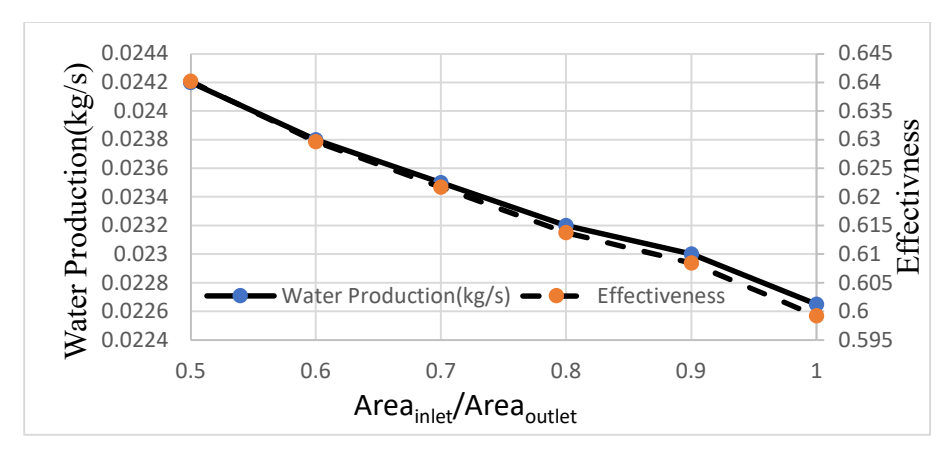


Figure 5-4. Effectiveness and water production of condenser for different wedge shapes for case $1 \ (\ddot{m}_L = 2.05 \ \text{kg/m}^2 \text{s}, \ \ddot{m}_a = 0.5 \text{kg/m}^2 \text{s})$

In case 4 we considered the same mass flow rate at the inlet and the same volume of packing. The length of the wedge shape is 1 m, height is 1 m, depth at the inlet is 0.3 m and depth at the outlet is 1.7 m. The dimension of the rectangular cuboid is 1 m³. Table 5-3 shows effectiveness improves around 3% whenever a wedge shape direct contact cross flow packed bed condenser is used.

Table 5-3. Performance comparison for case 2. The boundary conditions for inlet air mass flow rate were 0.15 kg/s, and the inlet liquid mass flux was 2.05 kg/m²s

	Wedge Shape (Volume =1m ³)	Regular shape (Volume =1
		m^3)
Liquid Temperature (°C)	18.82	17.68
Air Temperature(°C)	32.81	33.5
Humidity Ratio (kg/kg)	0.0320	0.0332
Water Production (kg/s)	0.008145	0.007965
Effectiveness	0.72	0.70

5.5 Outcome

Concluded from the above-mentioned discussions, a wedge shape crossflow packed bed condenser is more effective than a conventional square-shaped packed bed condenser if the liquid mass flux can be well maintained from the top. It can be also stated from the analysis and

observations that this research can be helpful to design an optimized packed bed dimension for direct contact cross flow packed bed condenser

5.6 Maximizing Water Production using GA (genetic algorithm)

In this section, we will try to develop an objective function that will give the highest water production and optimized shape. For this analysis, the same mass flux is considered at the inlet. A single objective function has been developed and optimization has been done using GA. A brief detail of how genetic algorithm works is given below:

5.7 Genetic Algorithm

There have been many used algorithms such as particle swarm optimization, bat algorithm, harmony search to find an optimized solution of an objective function. Of them, the Genetic algorithm is considered one of the most popular algorithms[80]. It can be used for DNA analysis, business purpose, vehicle routing, neural network, etc. Genetic Algorithm has been used to get the optimized rectangle shape of the crossflow packed bed condenser. It is based on Darwin's theory which falls under the category of evolutionary algorithm. [38],[81]. Evolution biology is a concept of natural genetics and natural selections. Jim Holland introduced the first genetic algorithm in 197 [82]. GA can converge into accurate enough solutions in a fast way it can reach into near-optimal solution within a short amount of time. Most of the problem tends to get stuck into local optimum but the genetic algorithm searches for all possible solutions for maximum and minimum. therefore, it hardly gets stuck into local optimum. Therefore, we have decided to use the GA algorithm to find the optimized shape of cross packed bed condenser with the highest water production.

There are mainly fundamental 5 phases of genetic algorithm which is well discussed by Albadr et al[83]. Each phase is described below:

- ➤ Initial Population: It is a set of possible solutions of objective functions. Variables are defined as Genes and Genes that create solutions are called Chromosome(solutions)

 Here, usually binary values (0 and 1) are used. Genes are encoded in the chromosome.
- ➤ **Fitness Function**: Fitness function can be also called evaluation function as it predicts how accurate the solution is compared with optimum soliton. It gives a fitness score to each individual.
- > Selection: Whenever we have a calculation of fitness values, it helps to pass genes to the next generation. A higher fitness value has a higher chance of reproduction.

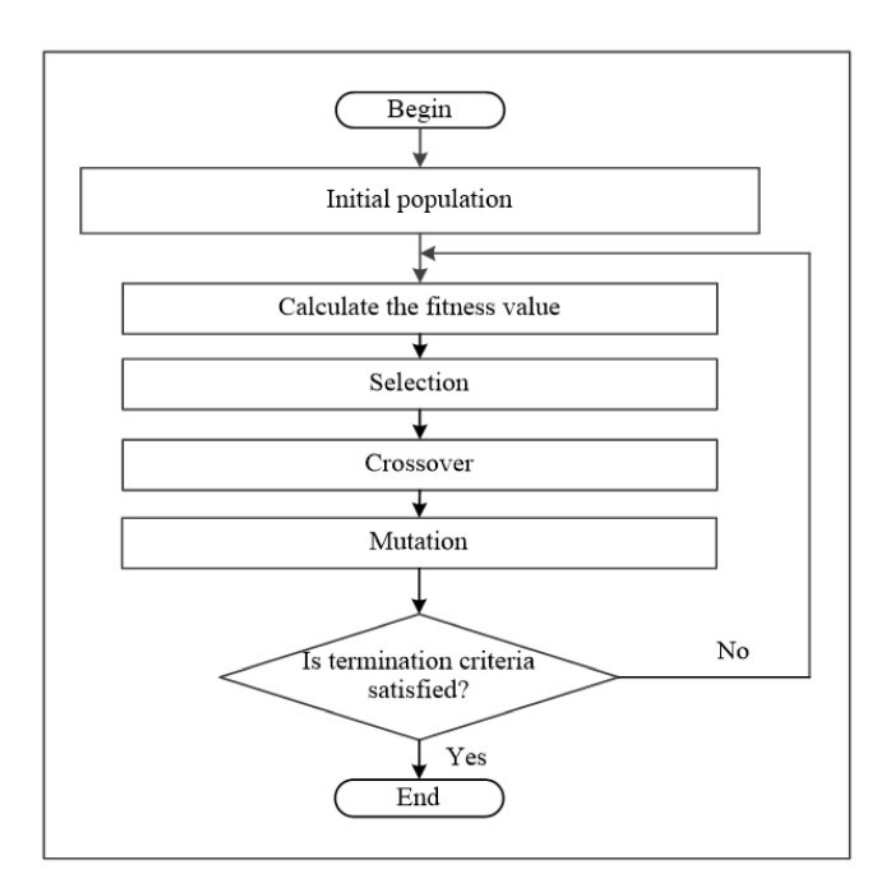


Figure 5-5. Flow chart of genetic algorithm[83]

➤ Crossover: Crossover is considered one of the most important stages of GA. In this, more than one parent is selected, and one or more off-springs are produced using the genetic

material of the parents. Offspring means interchanging genes of parents to create superior String. There are various types of crossovers such as one point cross over, multi over cross over, Uniform cross over, etc. However, Results from cross-over are added to the population.

- > **Mutation**: Mutation helps to control diversity within the population so that it cannot have premature convergence. It is essential for convergence.
- ➤ **Termination:** The GA algorithm terminates when it does not produce any new population and produced new offspring is not significantly differ from the previous generation. It converges then and gives the final solution

5.8 Development of Objective Function

A single objective function is developed with some constraints. As we aim to maximize water production by optimizing length and height, the equation of water production is stated below:

Objective function

$$m_{cond} = \ddot{m}_a * (\omega_{in} - \omega_{out}) * A_c \tag{5-7}$$

Constraints

Depth= 1 m

0.1 < L < 2.5

0.1 < H < 2.5

Volume = L * H * Depth= $(0.5 \sim 2) \text{ m}^3$

Here, several cases have analysis by changing volume constraints. It has been analyzed what will be optimized dimension whenever volume will be equal to 0.5,1,1,5 and 2 and limit of the length is 0.1 to 2.5 and limit of height is 0 to 2.5. GA algorithm has been adopted with two different boundary conditions and each boundary condition has four volume constraints. Table 5-4

depicts that if an optimized shape is used, higher water production can be achieved. For example, if a packed bed having L=1 m, H=1 m, and Depth =1 m is developed, Water production is 0.0409kg/s. But a packed bed having L= 1.1842 m, H=0.8442 m, and depth =1 m is used, water production is 0.0423 kg/s. Therefore, it can be seen that water production has improved by 3.4 percent having an optimized shape.

Table 5-4. Optimized length and height for maximum water production (Inlet liquid mass flux =1.02 kg/m²s, air mass flux=2.05 kg/m²s, inlet air temperature =50°C and inlet liquid temperature = 15°C)

Volume constraint	Length (m)	Height(m)	Water
(m^3)			Production(kg/s)
0.5	1.0232	0.4886	0.0223
1	1.1842	0.8445	0.0423
1.5	1.3074	1.1473	0.0596
2	1.4232	1.4053	0.0759

Table 5-5 shows that a rectangle cuboid shape has water production of 0.0226 kg/s and an optimized rectangle shape can have water production of 0.0230 kg/ so it can be stated that if an optimized shape can be built, it will be more efficient.

Table 5-5. Optimized length and height for maximum water production (Inlet liquid mass flux =0.5kg/m²s, Air mass flux=2.05 kg/m²s, Inlet air temperature =50°C and Inlet liquid temperature = 15°C)

Volume (m ³)	Length (m)	Height(m)	Water
			Production(kg/s)
0.5	0.7432	0.6729	0.0121
1	1.0407	0.9609	0.0230
1.5	1.1579	1.2954	0.0331
2	1.2386	1.6147	0.0423

5.9 Conclusion

The analysis of this chapter shows that there are various ways to improve the effectiveness and water production of crossflow packed condensers. Wedge shape can be a very good approach to improve the effectiveness of crossflow packed bed condensers. GA optimization can also provide us with optimized dimensions. However, more intensive research is needed to improve the effectiveness and water production of crossflow packed condensers. Considering cylindrical crossflow packed condenser may have more efficiency than wedge shape and optimized shape.

CHAPTER 6 : Modeling and Experimental Validation of Direct Contact Crossflow Packed Beds Condenser Used in HDH Desalination system

6.1 Introduction

A modified two-dimensional mathematical model is proposed in this chapter that solves for the enthalpy values of the working fluids. The PDEs are solved using finite differences. To validate the model, an experimental condenser was built and tested. Water temperatures inside the test section at twenty-nine locations were measured, as well as the air vapor temperatures of five locations at outlet. The measured water and air-vapor temperatures agree with the simulation results with less than 5% error in most of the compared domain.

6.2 Nomenclature

a Specific area of packing material (m²/m³)

C_p Specific heat (kJ/kgK)

D Molecular diffusion coefficient (m²/s)

Depth Depth of packed bed (m)

Fr Froude number*

g Gravity (m²/s)

 h_v Enthalpy of vapor (kJ/kg)

 h_l Enthalpy of liquid (kJ/kg)

 h_{fg} Enthalpy of condensation(kJ/kg)

k Mass transfer co-efficient (m/s)

M Molecular vapor weight (kg/kmol)

m Mass flow rate (kg/s)

m Mass flux (kg/m²s)

Nu Nusselt Number* P Total pressure of the system (kPa) \dot{Q} Heat transfer rate (J/s) Re Reynolds number* R Universal gas constant (kJ/kmol K) Sc Schmidt number* T Temperature (°C or K) U Overall heat transfers coefficient (W/m^2K) We Webber Number* ρ Density(kg/m³) μ Dynamic viscosity (kg/ms) ω Humidity ratio (kg/kg) (g / kg of dry air) ϕ Relative Humidity σ_l Surface tension of liquid (N/m) σ_{pack} Surface tension of packing material (N/m) *See Appendix for definition of dimensionless number **Subscripts** a Air amb Ambient state cond Condensation exp Experimental G Air/Vapor mixture

GA Gas side parameter based on the specific area of packing material.

LA Liquid side parameter based on the specific area of packing material.

l Liquid phase

pack Packed beds

sat Saturation state of species

sim Simulation

v Vapor phase

w Wetted

6.3 Modified Enthalpy based Mathematical Model

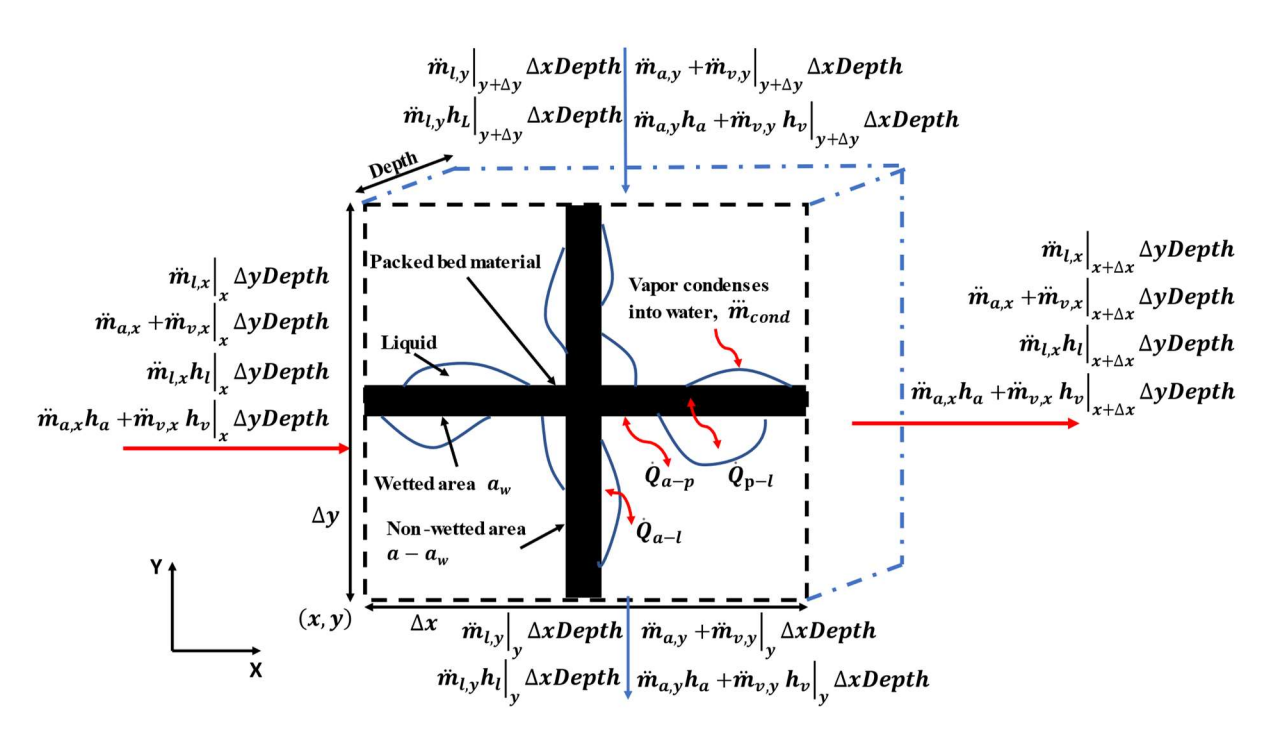


Figure 6-1. A representative control volume in a cross flow packed beds condenser showing the various phases (black = solid, blue = liquid, white = air/vapor mixture) and the transport processes occurring within (drawn by Dr Xu Tan)

In this section, a 2D steady state mathematical model is developed using the control volume shown in Figure 6-1. Hot air-vapor comes in horizontally from the left and cooling water drops vertically from the top. Air flow is assumed to be uniform with no y directional components, and

momentum equation is not considered. Gas components of air and vapor are considered as ideal gases. The relative humidity is considered 100 percent throughout the condensation process. The control volume in Figure 6-1 includes the packed beds where conservations of mass and energy are used through liquid side and gas side. The black cross represents the geometry of the packing material. As liquid droplets attach on the packing material, the specific surface area of the packed beds $(a, m^2/m^3)$ can be differed as wetted area $(a_w, m^2/m^3)$ where droplets are located and nonwetted area $(a - a_w, m^2/m^3)$ where liquid does not contact the packing material. In this control volume heat transfer takes place between liquid and the packing material through wetted area. The heat and mass transfer rates between liquid and air-vapor occur through their interface, and the interfacial area is considered same as the wetted area. In the end, there is also heat transfer between the packing material and air-vapor through non-wetted area.

6.3.1 Conservation of Mass

The mass conservation for liquid side can be initially described with Eq. (6-1).

$$\ddot{m}_{l,x}\big|_{x}\Delta y Depth - \ddot{m}_{l,x}\big|_{x+\Delta x}\Delta y Depth + \ddot{m}_{l,y}\big|_{y+\Delta y}\Delta x Depth - \ddot{m}_{l,y}\big|_{y}\Delta x Depth + (6-1)$$

$$\ddot{m}_{cond}\Delta x \Delta y Depth = \frac{\partial (m_{l})}{\partial t}$$

where \ddot{m}_l is the mass flux of liquid, $kg/(s \cdot m^2)$, that can have components in the x and y directions. In this case, water is assumed to only flow in y direction, hence $\ddot{m}_{l,y} = \ddot{m}_l$ after eliminating the x components. \ddot{m}_{cond} is the condensation rate $kg/(s \cdot m^3)$. The right-hand side of the equation stands for the changing rate of the total liquid mass in the control volume. Therefore, Eq. (6-1) can be simplified into Eq. (6-2) at steady state.

$$\frac{\partial \ddot{m}_{L,y}}{\partial y} = \frac{\partial \ddot{m}_{l}}{\partial y} = \ddot{m}_{cond} \tag{6-2}$$

Similarly, the mass conservation for gas side will include the mass flows over the boundaries, condensation, and the rate of change of air-vapor in the control volume $(m_a + m_v)$, described as Eq. (6-3).

$$\ddot{m}_{a,x} + \ddot{m}_{v,x} \Big|_{x} \Delta y Depth - \ddot{m}_{a,x} + \ddot{m}_{v,x} \Big|_{x+\Delta x} \Delta y Depth +$$

$$\ddot{m}_{a,y} + \ddot{m}_{v,y} \Big|_{y+\Delta y} \Delta x Depth - \ddot{m}_{a,y} + \ddot{m}_{v,y} \Big|_{y} \Delta x Depth - \ddot{m}_{cond} \Delta x \Delta y Depth =$$

$$\frac{\partial (m_a + m_v)}{\partial t}$$

$$(6-3)$$

Air-vapor is assumed to have only x component therefore Eq. (6-3) will be deducted into Eq. (6-4) for steady state.

$$-\frac{\partial \left(\ddot{m}_{a,x} + \ddot{m}_{v,x}\right)}{\partial x} = -\frac{\partial \left(\ddot{m}_{a} + \ddot{m}_{v}\right)}{\partial x} = \ddot{m}_{cond} \tag{6-4}$$

where \ddot{m}_a and \ddot{m}_v are mass flow flux, $kg/(s \cdot m^2)$. Through the condensation process, mass flow of air remains constant, and mass flow flux of vapor can be represented by $\ddot{m}_v = \ddot{m}_a \omega$. At last, the conservation of mass for gas and liquid is trimmed into Eq. (6-5).

$$-\ddot{m}_a \frac{\partial \omega}{\partial x} = \frac{\partial \ddot{m}_l}{\partial y} = \ddot{m}_{cond} \tag{6-5}$$

6.3.2 Conservation of Energy

Energy transfer rate on liquid side can be described with Eq. (6-6).

$$\ddot{m}_{l,x}\mathbf{h}_{l}\big|_{x+\Delta x}\Delta y Depth - \ddot{m}_{l,x}\mathbf{h}_{l}\big|_{x}\Delta y Depth + \ddot{m}_{l,y}\mathbf{h}_{l}\big|_{y+\Delta y}\Delta x Depth -$$

$$\ddot{m}_{l,y}\mathbf{h}_{l}\big|_{y}\Delta x Depth + \dot{Q}_{cond} + \dot{Q}_{a-l} + \dot{Q}_{p-l} = \frac{\partial (m_{l}\mathbf{h}_{l})}{\partial t}$$

$$(6-6)$$

The energy balance on the liquid side involves the enthalpy exchange rate through the boundary of the control volume, the heat related to condensation \dot{Q}_{cond} , heat transfer rate between the air-vapor and liquid \dot{Q}_{a-l} , and heat transfer rate between the packed beds and liquid \dot{Q}_{p-l} . As

mentioned previously, liquid mass flux only has component on y direction, and steady state is only considered this time. Therefore, Eq. (6-6) can be transformed into Eq. (6-7).

$$\ddot{m}_{l}h_{l}|_{y+\Delta y}\Delta x Depth - \ddot{m}_{l}h_{l}|_{y}\Delta x Depth + \ddot{m}_{cond}h_{fg}(T_{i})\Delta x \Delta y Depth +$$

$$U_{L}a_{w}(T_{pack} - T_{l})\Delta x \Delta y Depth + Ua_{w}(T_{a} - T_{l})\Delta x \Delta y Depth = 0$$

$$(6-7)$$

where h_{fg} is the latent enthalpy at the temperature of interface between air-vapor and liquid, U_L is the heat transfer coefficient between the liquid and packed beds, U is the heat transfer coefficient between the liquid and air-vapor. Eq. (6-7) is then derived into Eq. (6-8).

$$\frac{\partial (\ddot{m}_l \mathbf{h}_l)}{\partial y} - \ddot{m}_a \frac{\partial \omega}{\partial x} \mathbf{h}_{fg}(T_i) + U_L a_w (T_l - T_{pack}) + U a_w (T_l - T_a) = 0$$
 (6-8)

Expanding the first term in Eq. (6-8) and using Eq. (6-5), results in.

$$\ddot{m}_l \frac{\partial \mathbf{h}_l}{\partial \mathbf{v}} = \ddot{m}_a \frac{\partial \omega}{\partial \mathbf{x}} (\mathbf{h}_{fg}(T_i) - \mathbf{h}_l(T_l)) - U_L a_w (T_{pack} - T_l) - U a_w (T_a - T_l)$$
(6-9)

Using a similar approach, the energy balance on gas side can be initially expressed with

$$\ddot{m}_{a,x}\mathbf{h}_{a} + \ddot{m}_{v,x}\mathbf{h}_{v}\big|_{x}\Delta y Depth - \ddot{m}_{a,x}\mathbf{h}_{a} + \ddot{m}_{v,x}\mathbf{h}_{v}\big|_{x+\Delta x}\Delta y Depth + \tag{6-10}$$

$$\left.\ddot{m}_{a,\,y}\mathbf{h}_{a}+\ddot{m}_{v,\,y}\mathbf{h}_{v}\right|_{v+\Delta v}\Delta xDept\mathbf{h}-\left.\ddot{m}_{a,\,y}\mathbf{h}_{a}+\ddot{m}_{v,\,y}\mathbf{h}_{v}\right|_{v}\Delta xDept\mathbf{h}-\left.\dot{Q}_{cond}-\dot{Q}_{a-l}-\dot{Q}_{cond}\right|_{v+\Delta v}\Delta xDept\mathbf{h}$$

$$\dot{Q}_{a-p} = \frac{\partial (m_a h_a + m_v h_v)}{\partial t}$$

The first four terms in Eq. (6-10) are the enthalpy of air vapor exchange rate through the control volume. Since \dot{Q}_{cond} , \dot{Q}_{a-l} , and \dot{Q}_{p-l} are considered positive Eq. (6-6) during the condensation process on the liquid side, \dot{Q}_{cond} , \dot{Q}_{a-l} , and \dot{Q}_{p-l} will be negative on gas side. Air flow is assumed to only have horizontal component, so Eq. (6-10) can be simplified to Eq. (6-11).

$$-\frac{\partial (\ddot{m}_{a} \mathbf{h}_{a} + \ddot{m}_{v} \mathbf{h}_{v})}{\partial x} + \ddot{m}_{a} \frac{\partial \omega}{\partial x} \mathbf{h}_{fg}(T_{i}) - U_{L} a_{w} (T_{a} - T_{l}) - U_{G}(a)$$

$$-a_{w}) (T_{a} - T_{pack}) = \frac{\partial (m_{a} \mathbf{h}_{a} + m_{v} \mathbf{h}_{v})}{\partial t}$$
(6-11)

Expanding the first term in Eq. (6-11) with the assumption that air mass flow stays constant on x direction and substituting Eq. (6-2) at steady state yield Eq. (6-12) below

$$\ddot{m}_{a} \frac{\partial h_{a}}{\partial x} = -\ddot{m}_{a} \frac{\partial \omega}{\partial x} \left(h_{fg}(T_{i}) - h_{v}(T_{a}) \right) - \ddot{m}_{v} \frac{\partial h_{v}}{\partial x} - U_{L} a_{w} (T_{a} - T_{l}) - U_{G} (a - a_{w}) \left(T_{a} - T_{pack} \right)$$

$$(6-12)$$

In previous publications, enthalpies in the governing equations were further expanded by considering the specific heat coefficients of water, vapor, and air constant. Since the heat capacity of vapor increases as temperature rises, assuming the vapor heat capacity as constant may cause energy imbalanced in the final solution. Therefore, this chapter directly solves Eq. (6-5), Eq. (6-9), and Eq. (6-12). for the enthalpies of air and water (h_a and h_v) as variables. Eq. (6-9) is solved by finite difference backward scheme and Eq. (6-12) is solved by forward scheme. Both are solved in terms of Eq. (6-13).

$$A\vec{h} = \overline{F(h)}$$
 (6-13)

where A is a matrix of know constants, $\overline{F(h)}$ is a vector of known constants represents the right-hand side of Eq. (6-9) and Eq. (6-12). All fluid properties are found from properties tables of air and steam. Additional details are provided in Appendix A.

In addition, because the inlet air-vapor is already saturated in the experiments, the air-vapor further on is considered saturated all over the domain. Therefore, humidity ratio at each node can be calculated with Eq. (6-1). Accordingly, the derivative of humidity ratio can be obtained after the space is discretized.

$$\omega = \frac{\ddot{m}_v}{\ddot{m}_a} = \frac{0.622\phi P_{sat}(T_a)}{P - \phi P_{sat}(T_a)} \tag{6-14}$$

where ϕ is relative humidity, and it's 100% everywhere, P is pressure of air-vapor, and the pressure at air-vapor inlet is 1 atm. Pressure drop is estimated using following equation.

$$\frac{\Delta P}{L} = \frac{\ddot{m}_a^{1.4}}{\rho_g} \left[0.054 + 654.48 \left(\frac{\ddot{m}_l}{\rho_l} \right)^2 + 1.176 \times 10^7 \left(\frac{\ddot{m}_l}{\rho_l} \right)^4 \frac{\ddot{m}_a^4}{\rho_g^2} \right]$$
(6-15)

Onda's correlation is used to estimate mass transfer coefficients in this paper.[71] In 2021, Abedi et al.[68] analyzed different empirical correlations for a direct contact condenser with packed beds. They developed an experimental setup of counterflow direct contact condenser with same type of packed beds used in the paper. After a thorough comparison among several previous correlations of mass transfer coefficients, Onda's correlation stood out because it yielded the closest analytical prediction compared to the experimental results. Therefore, Onda's correlation is used to in this research to estimate mass transfer coefficients. The method calculating heat transfer coefficients among liquid, air-vapor, and packed beds is adopted from Eckert et al.[79].

6.4 Experimental Setup

To validate the mathematical model and analyze the temperature pattern of liquid throughout the packed beds, a laboratory-scale crossflow direct contact packed beds condenser setup was built. Figure 6-2 is a schematic diagram and provide a pictorial view of the system. The dimension of heat transfer area of the packed beds (Length × Height × Depth) was 0.4 m × 0.3m × 0.2m. Dry compressed air came from the air facility of laboratory. A steam generator of 7.5 kW was installed to create steam continuously. Air and steam directly merged from the inlet pipe where packed beds were inserted to enhance the mixing. At the beginning, size 4 NPT pipe was used, and the channel was gradually reformed to rectangular shape to Height × Depth of 0.3m × 0.2m. Insulation was installed to reduce heat loss so that the temperature profile of the air vapor could be more uniform.

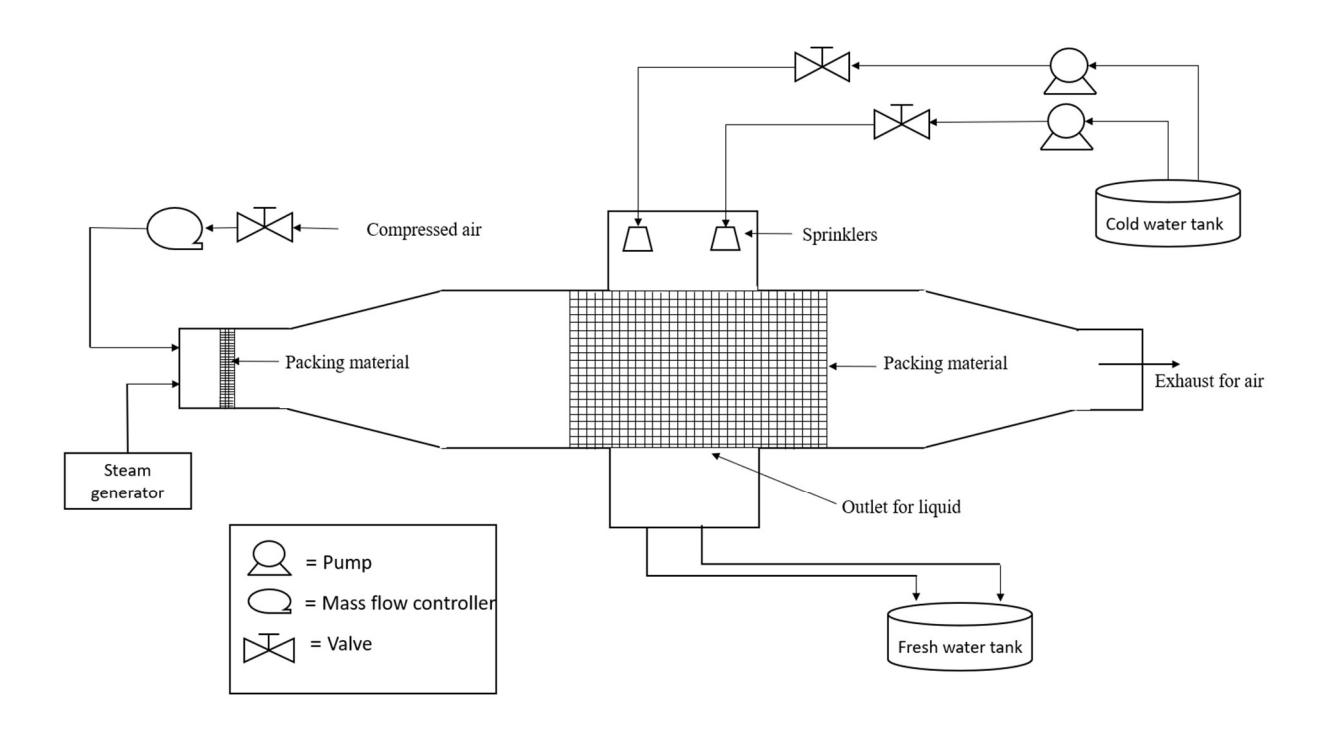


Figure 6-2. Schematic diagram of the direct contact cross flow packed beds condenser facility

Two square pattern spray nozzles were used at the cooling water inlet. The square pattern spray nozzle is designed to allow a flow capacity of 37.85ml/s at 20 psi with a 65-degree angle. Two spray nozzles were properly placed above the packed beds so that cooling water can be evenly distributed at the top. Two pumps were installed to draw cooling water from the storage tank, and heated water was collected from the bottom to another storage tank. Two water valves were used to control water flow rate into the condenser. The packed beds are made of polypropylene and manufactured by Lantec Products, Inc. The packing material was cut to proper size so it could steadily sit inside the chamber as in Figure 6-3. The specific area to volume ratio of the packing material is 267 m²/m³. The effective packing diameter is 0.017m and the void fraction is 87.8%. The casing of the main chamber was built with transparent polycarbonate sheets so that the condensation process would be visible during the experiment. The thickness of polycarbonate plastic is 1/4" and it can withstand temperatures from -40°C to 100°C.

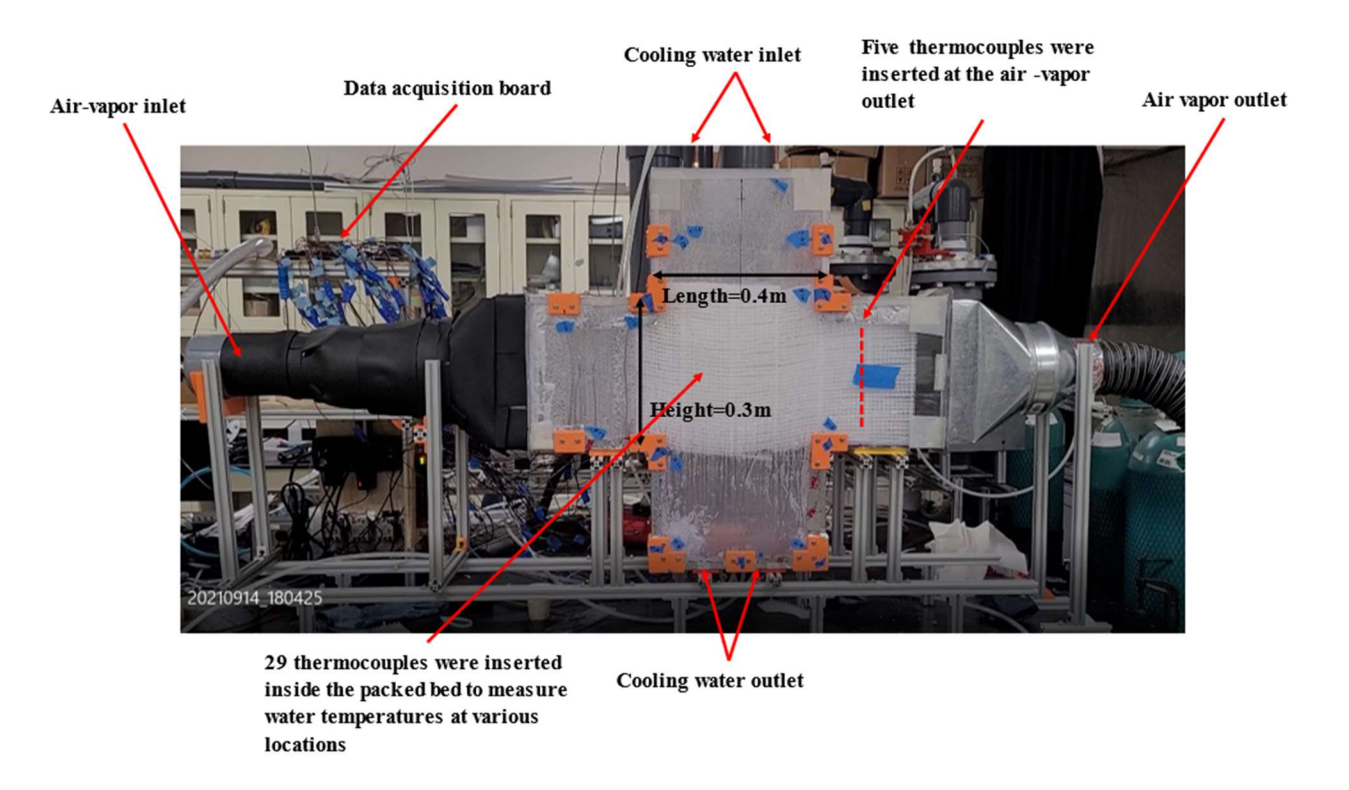
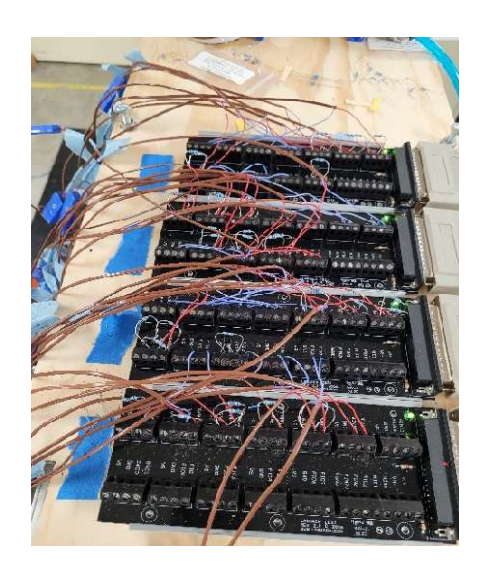


Figure 6-3. A laboratory-scale experimental setup, shown above, of direct contact crossflow packed beds condenser was used to validate the mathematical model using 29 thermocouples located in the packed bed

Data acquisition and control system was set up with LabJack T7 pro DAQ and programmed with LabVIEW. Air flowrate was measured and controlled with an ALICAT 1000 SLPM flow controller. Type T thermocouples were calibrated to measure the temperatures of air-vapor and cooling water at inlets and outlets. Specially, many thermal couples were inserted deep inside packed beds at various locations to compare with the water temperature contour calculated by 2D mathematical model. Gems Turbine Flow Sensors were used to measure the cooling water flow rates. The specifications of the instrument are presented in Table 6-1.



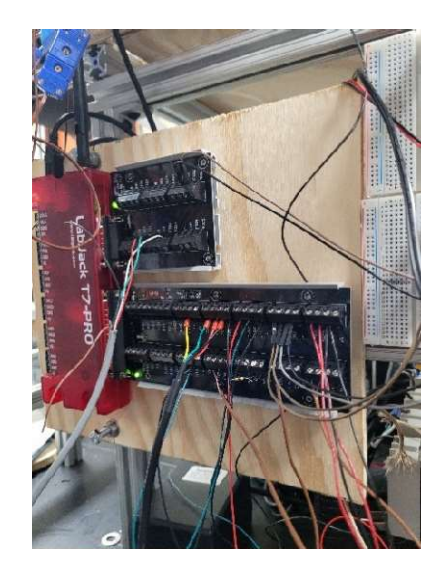


Figure 6-4. Data acquisition Board for storing data

Table 6-1. Specification of the instrument used for measurement

Sensors	Ranges	Uncertainty
1/8" Type T thermocouples	-325 -700°F	±0.3°C or ±0.75%
ALICAT air flow controller	1000 SLPM	±0.8% of reading ±0.2% of full scale
Water flow sensor	0.13 - 1.3 GPM	$\pm 3\%$
Ruler		±0.5mm

6.5 Experimental and Simulation Result Analysis

6.5.1 Experimental Method

The condenser was tested while the flow rates and temperatures of cooling water were kept constant. Four cases were investigated by adjusting dry air mass flow rate and inlet air-vapor temperature. Table 6-2 lists the inlet boundary conditions for the four cases. Two spray nozzles were used to cover the top surface of the packed beds, and the positions of the nozzles were manually adjusted so that each one could cover half of the surface (0.2m×0.2m). Since the flow rates of the cooling water were manually controlled with valves, it was impossible to keep the flow rate identical within the accuracy of the sensors. Therefore, two flowrates were individually recorded and input as the boundary conditions for the simulation.

Table 6-2. Boundary conditions for four cases studied

	Dry air flow	Inlet air-vapor	Inlet cool	ing water	Inlet cooling water
	flux, $kg/(m^2 \cdot s)$	temperature, °C	flow flux,	$kg/(m^2 \cdot s)$	temperature, °C
Case 1	0.134	43.4	0.50	0.48	21.8
Case 2	0.117	45.5	0.49	0.48	21.8
Case 3	0.100	48.4	0.50	0.48	21.8
Case 4	0.084	51.1	0.51	0.49	21.8

Figure 6-5 illustrates how boundary conditions of mass fluxes of air and cooling water are exerted. The mass flux of air is assumed to be evenly distributed, while two uniform mass fluxes of cooling water are applied on the top covering halves of the area.

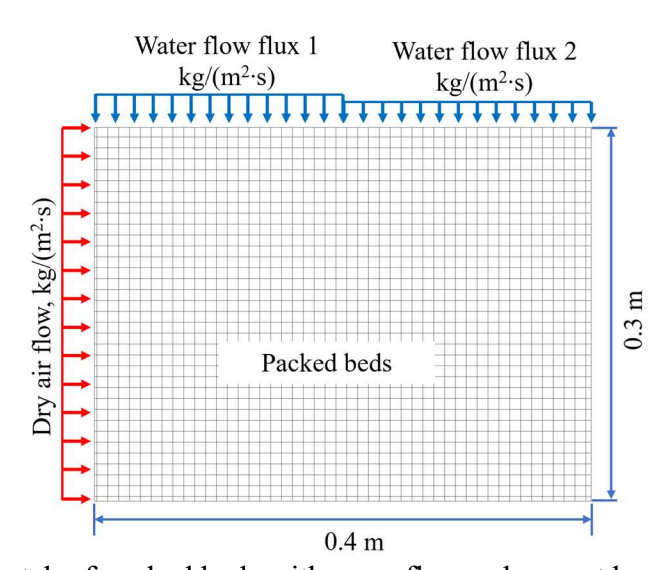


Figure 6-5. Sketch of packed beds with mass fluxes shown at boundaries

6.6 Results and Analysis

6.6.1 Temperature Based Results

In this section, both temperatures based, and enthalpy-based solution will be analyzed. It will be shown that enthalpy-based solution matches better than temperature-based solution as specific heat is constant that results in energy imbalance.

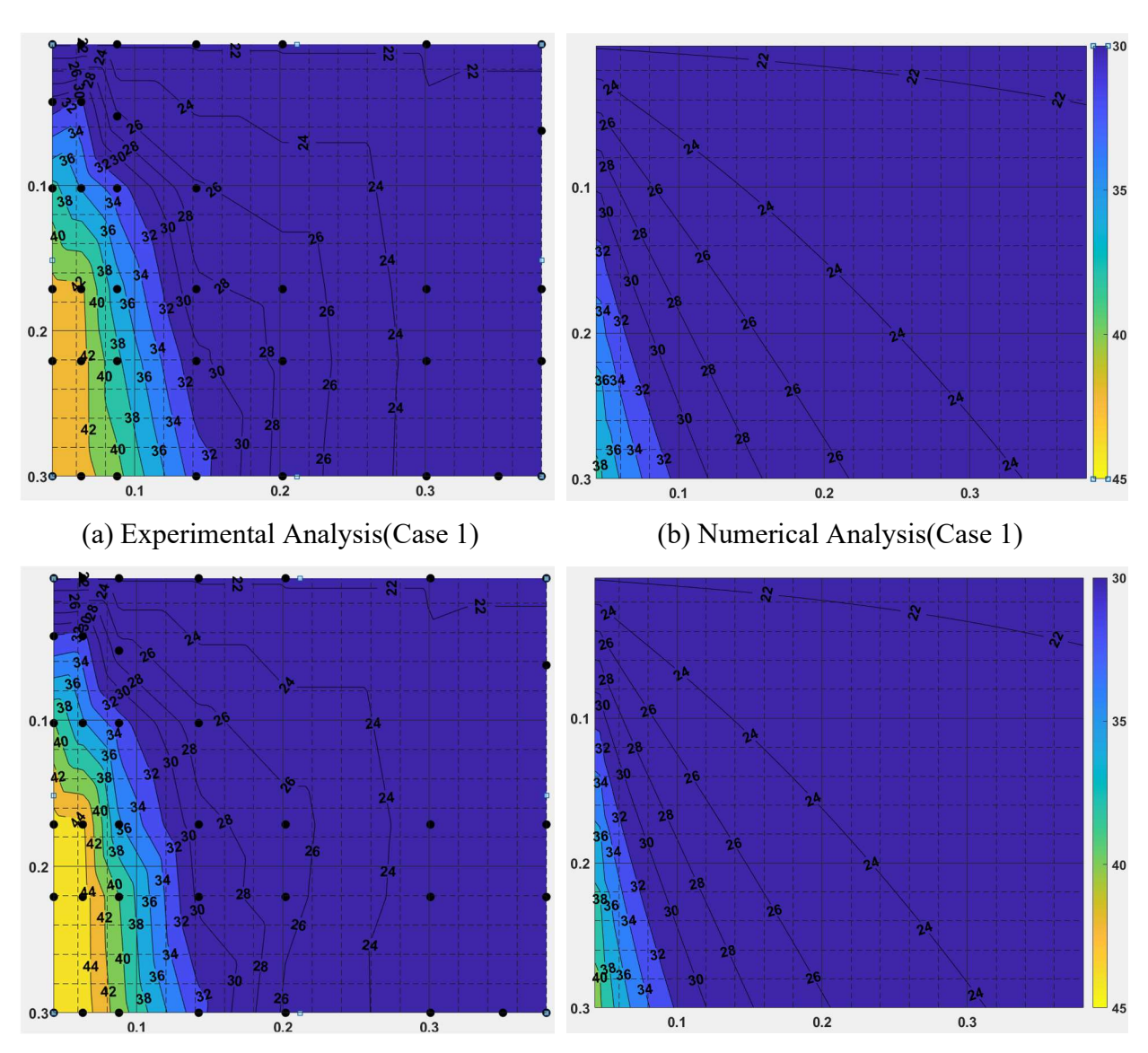
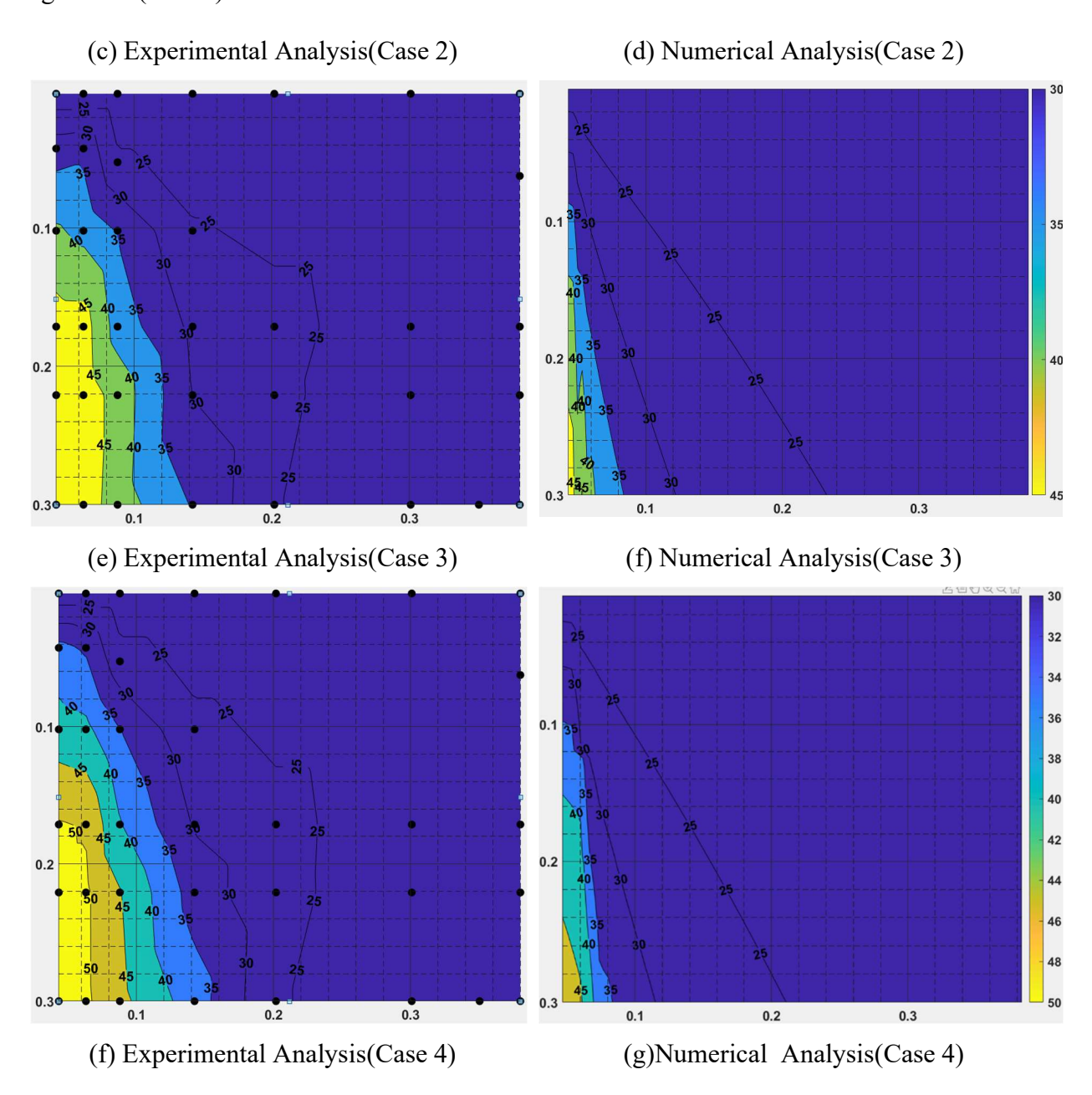


Figure 6-6. Comparison of experimental and numerical analysis for defined 4 cases in Table 6-2. Length is ranging from 0-0.4 m and height is ranging from 0 to 0.3 m

Figure 6-6 (cont'd)



It can be analyzed from Figure 6-6 that in the bottom left corner the value of temperature of liquid is higher than numerical analysis. In this region the error goes up to around 20 percent. Enthalpy based solution can reduce the error by 5 percent in the computational domain with adjusted boundary condition.

6.6.2 Enthalpy Based Results and Analysis

Figure 6-7 presents water temperature contours for all 4 cases across the 2D area of the packed beds. Solid lines are isotherms obtained from simulation results, and the red circles are the locations of thermocouples inserted in the packed beds along with measured temperature values. The diameters of the circles are 1/8", proportionally shown with respect to the X and Y axes ticks. Figure 6-8 includes air-vapor temperature contours filled with colors for 4 cases over the domain obtained from simulations only.

The variation trends of the water temperature of both simulations and experiments closely match each other. Vertically, water temperature increases as water drips through the packed beds because heat is transferred from air-vapor to water. However, water temperatures near the air-vapor inlet increase more dramatically than the temperatures near the air-vapor outlet. It can be expected since air-vapor temperatures decrease on x direction shown as in Figure 6-8, therefore heat transfer will be less effective further long. As a result, horizontally, water temperatures appear to decrease along the flow direction of air-vapor.

Water temperature contours for 4 cases, ${}^{\circ}C$ Case 1 Case 2 0.3 0.2 0.1 € 0.0 Case 3 Case 4 **≻** 0.3 25 0.2 . 22.5 0.1 0.0 0.2 0.4 0.2 0.0

Figure 6-7. Water temperature contours of four cases studied. The water temperatures of both simulations and experiments closely match each other. Vertically, water temperature increases as water drips through the packed beds, horizontally, water temperatures appear to decrease along the flow direction of air-vapor. The red numbers above represent the measured temperatures

X, m

0.4

0.0

Similarly, the temperatures of air-vapor near the cooling water inlet horizontally decreases faster than the temperatures near the bottom of the packed beds. This appears reasonable because cooling water temperatures are warmer as cooling water falls through the packed beds. Consequently, water closer to the bottom will have less ability to condense the air-vapor. The pattern of water temperatures from experimental results matches the trends of simulation results although errors can be observed in Figure 6-7. Figure 6-9 includes 4 maps of errors for each case comparing the experimental measurement and simulation results. Locations of each thermocouple were used to obtain the simulation results through 2D interpolation. Then, local errors were calculated with Eq. (6-16).

$$Error\% = \frac{T_{sim} - T_{exp}}{T_{exp}} \tag{6-16}$$

where T_{sim} is the temperature from simulation, and T_{exp} is the temperature measured from experiment. Therefore, the error could be either negative or positive if the simulation under or overestimates the local temperature. In the end, the contour maps of error are obtained through linear 2D interpolation based on the available values and locations.

At most of the locations, the simulation results agree with the experimental results within 5% error. However, three regions may have errors more than 10% in some cases, and all of them are located within the isotherm lines between 30°C and 26°C in Figure 6-7. Among these three regions, in a region at the top left of the packed bed, the simulation results are below the local water temperatures by more than 10%.

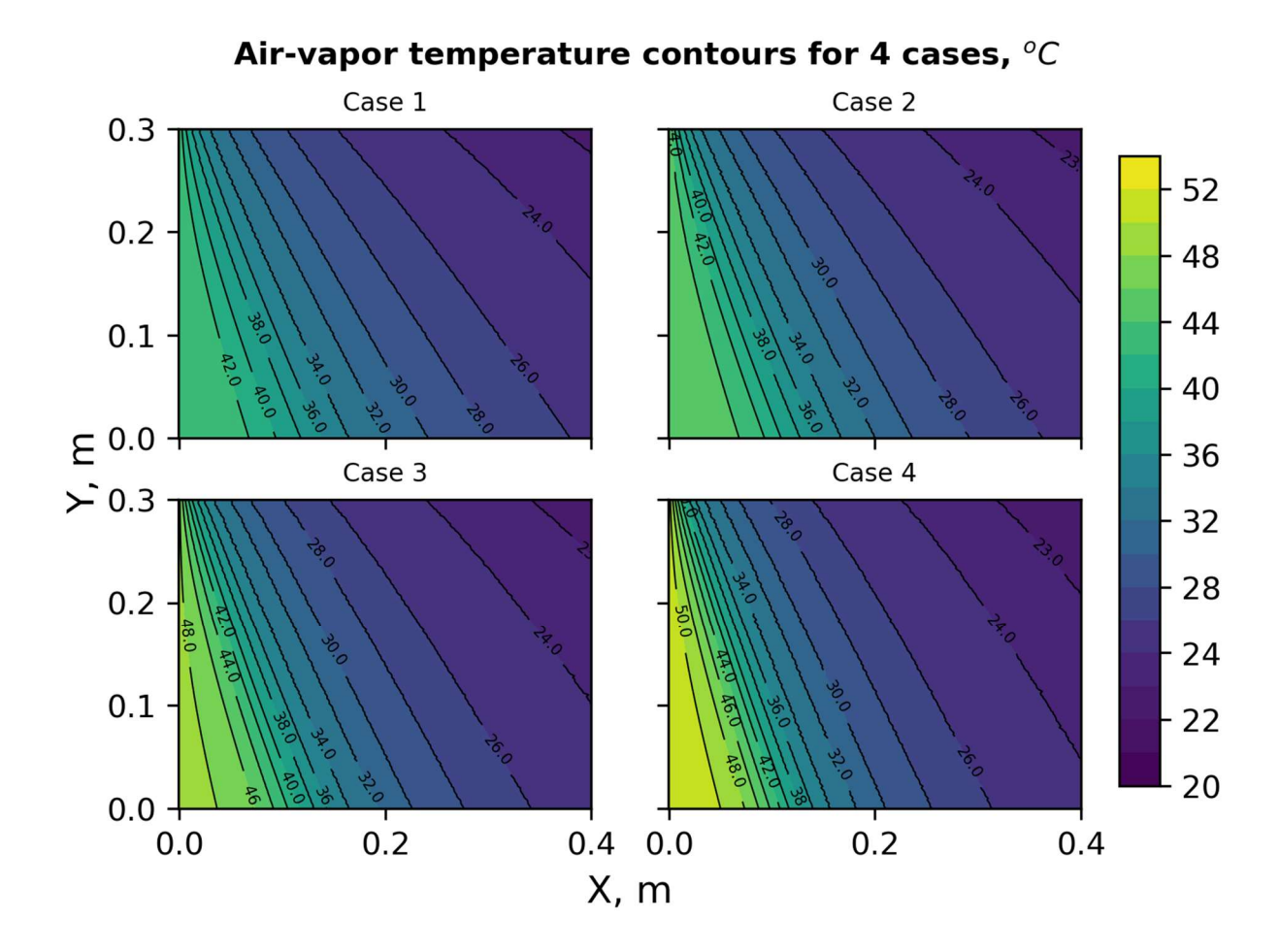


Figure 6-8. Temperature contours of air-vapor for the four studied cases. Air-vapor temperatures decrease on x direction, and the temperatures of air-vapor near the cooling water inlet horizontally decreases faster than the temperatures near the bottom of the packed beds

Percentage of error for water temperature map, %

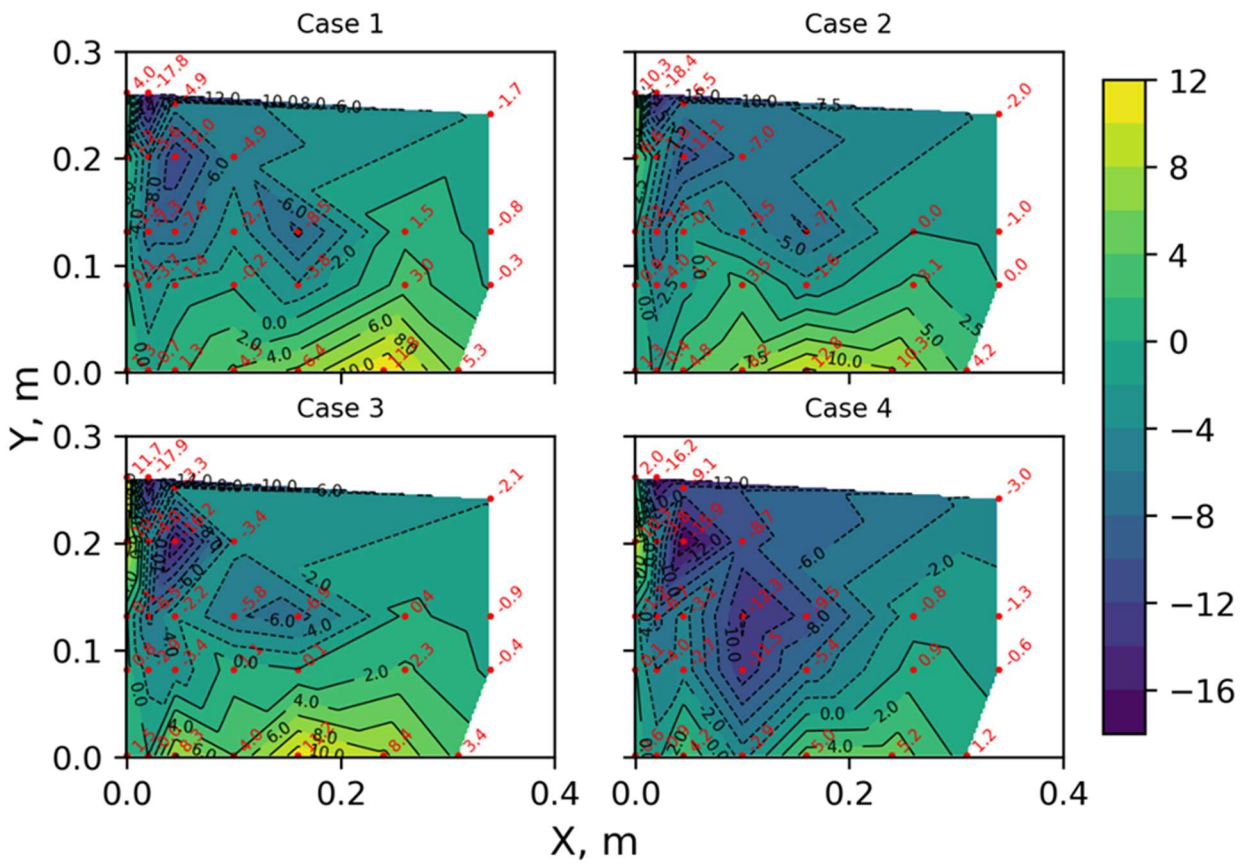


Figure 6-9. Error maps comparing analytical and experimental results. The simulation results agree with the experimental results within 5% error in most areas. However, three regions may have errors more than 10% in some cases, and all of them are located within the isotherm lines between 30°C and 26°C in Figure 6-7. Among these three regions, at the top left of the packed bed , the simulations always underestimate the local water temperatures by more than 10% (by Dr Xu Tan)

Near the top left corner of the condenser is also the edge of the cooling water spray. The water spray near the edge could have severe bouncing and splashing between the side wall and top packed beds surface. Therefore, the flow flux is likely not uniform as assumed previously. To verify this assumption, the boundary condition of cooling water mass flux near the left corner was manually adjusted shown as Figure 6-10. The local mass flux was tuned up and down based on the positive and negative errors at the top left of the domain. Although it is not known how much cooling water mass flux fluctuates near the corner, the mass flux was tuned up to 1.5 times of its original value in the first 0-1.5cm region, while in the adjacent region (1.5-3cm), the mass flux

was tuned down to half of its original value. Four cases were simulated again based on the new boundary conditions, and the new maps of errors are presented in Figure 6-11.

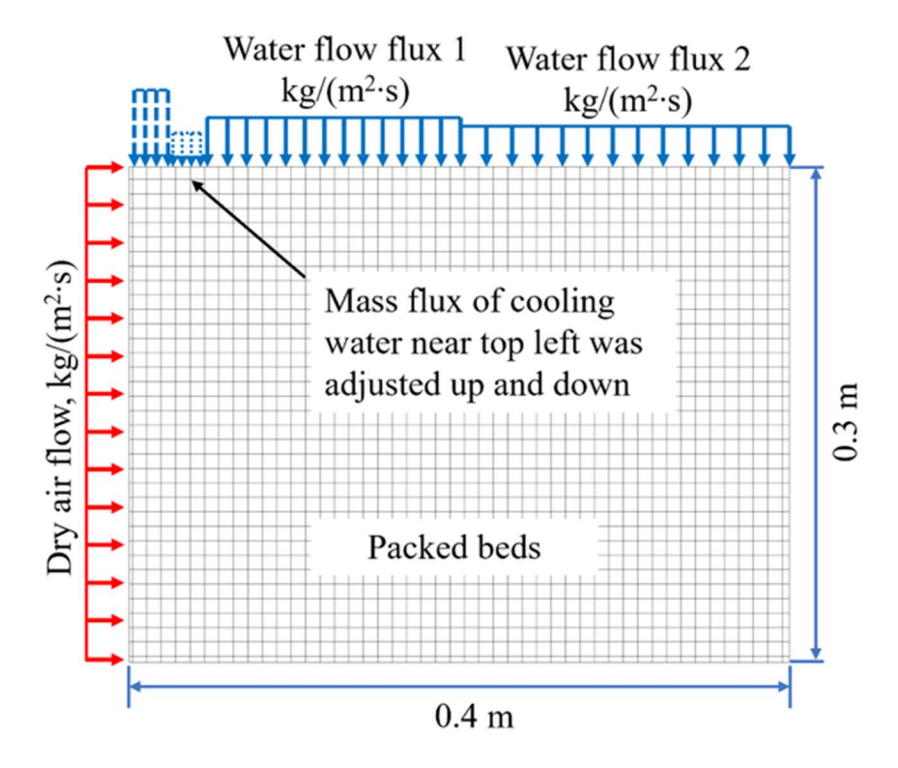


Figure 6-10. Adjusted cooling water boundary condition. Although it is not known how cooling water mass flux fluctuates near the corner, the mass flux was tuned up to 1.5 times of its original value in the first 0-1.5cm region, while in the adjacent region (1.5-3cm), the mass flux was reduced or tuned down to half of its original value

Apparently, as seen in the figure, the errors are significantly reduced for all cases. Not only the errors at top left region are remarkably reduced to less than 10%, errors at other locations also are also improved. Although the actual values of flow flux of cooling water near top left region are unknown, this suggests that the assumption of variations in the flux is as a cause of errors around the inlet region is reasonable. What's more important, it can further indicate that the mathematical model works properly, and it can provide accurate detailed prediction with correct inlet boundary conditions

Percentage of error for water temperature map, %

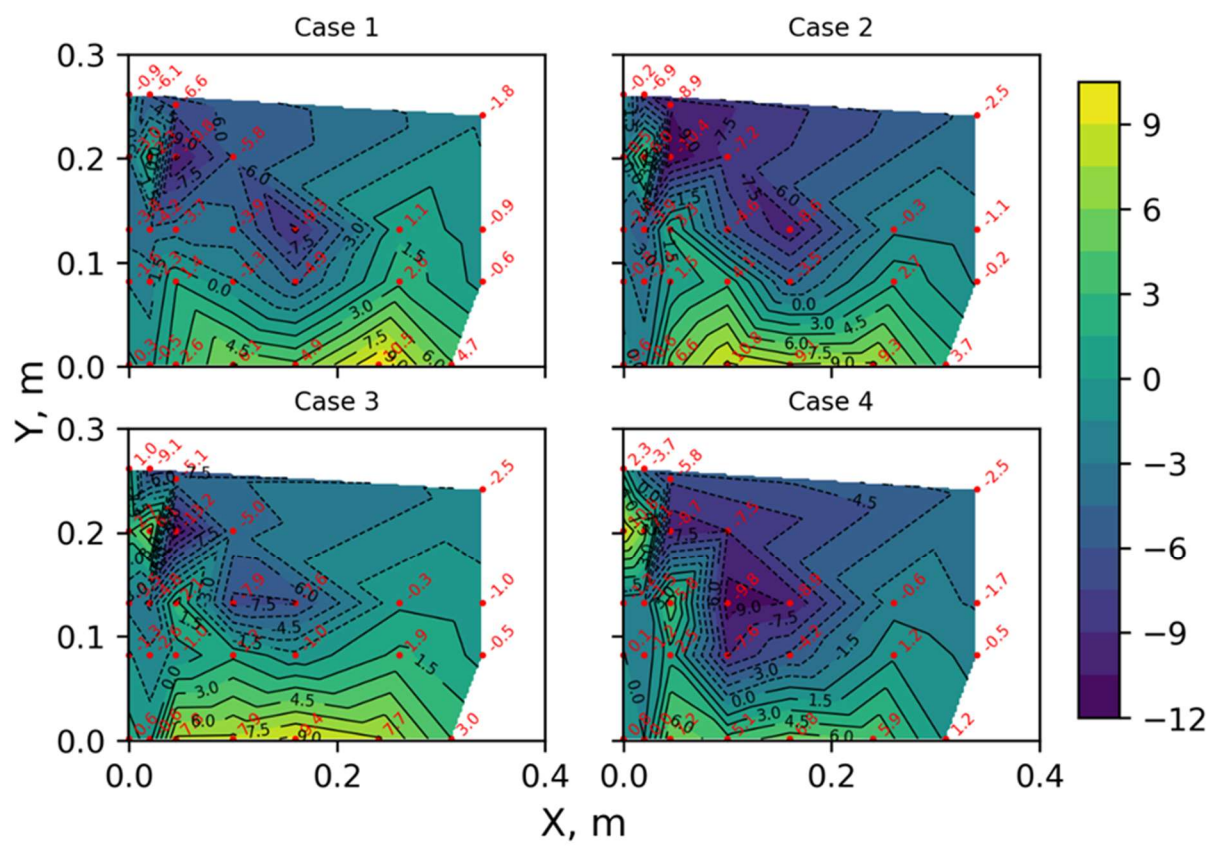


Figure 6-11. Error maps between the analytical and experimental results after the cooling water boundary condition is adjusted. For each case, the errors are significantly improved. Not only the errors at top left region are remarkably reduced to less than 10%, errors at other locations also are also improved

In addition to water temperature data, five measurements of air-vapor temperature were obtained at the outlet where thermocouples did not contact the cooling water. The analytical and experimental results of four cases are presented in Figure 6-12. In this figure, the red dots are measured temperature along vertical locations, and the dash lines represent the theoretical simulations. In all four cases, the first four experimental points from the top are all very close to the simulation results, except the last temperatures measured at the bottom of the air-vapor flow channel. Instead of calculating the errors of each point, the area weighted temperatures are used to compare the simulation and experiment. The area weighted temperature is calculated by Eq.(6-17).

$$\frac{\sum_{i=1}^{n} T_{i} A_{i}}{\sum_{i=1}^{n} A_{i}} \tag{6-17}$$

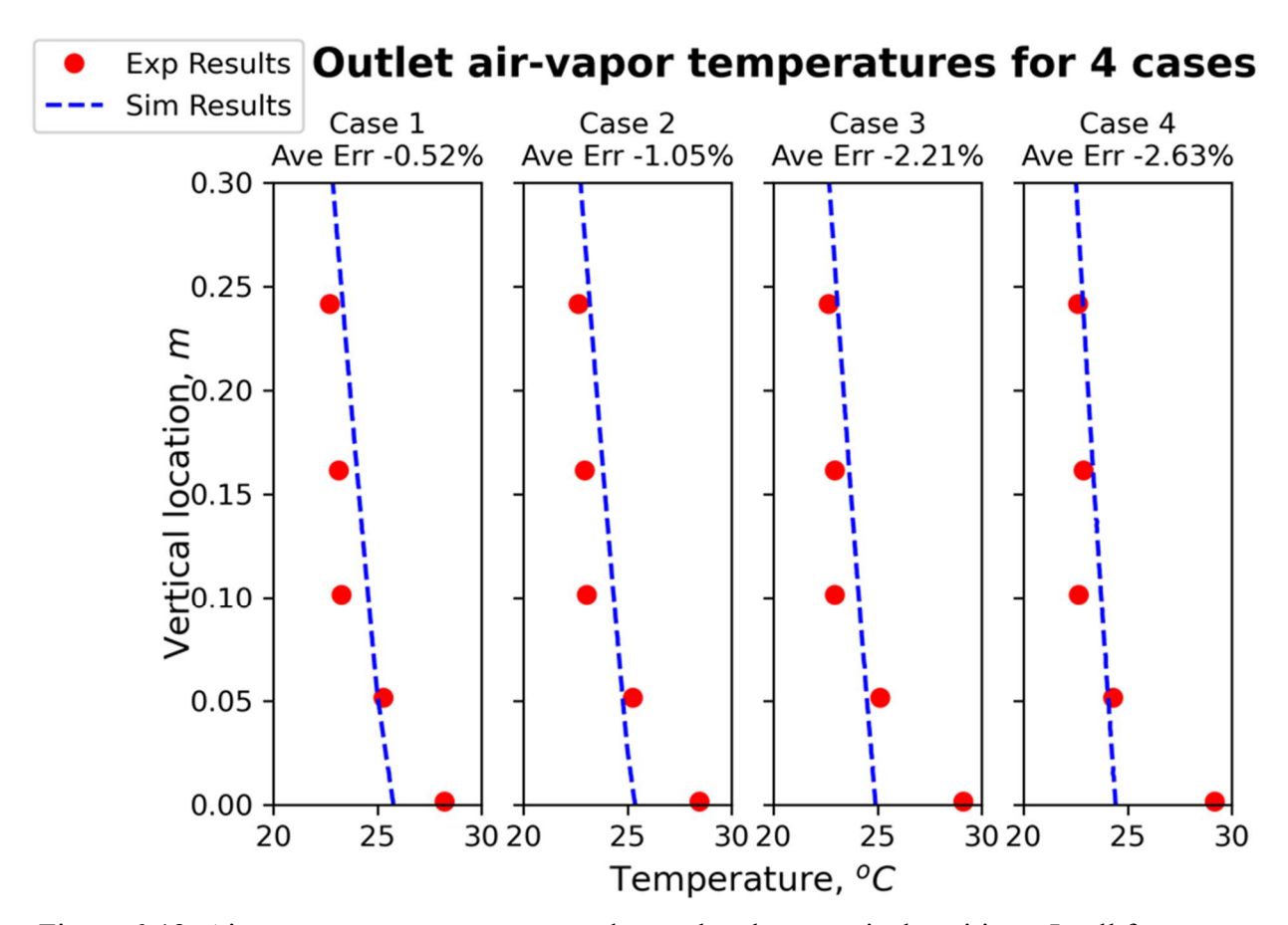


Figure 6-12. Air vapor temperature measured at outlet along vertical positions. In all four cases, the first four experimental points from the top are all very close to the simulation results, except the last temperatures measured at the bottom of the air-vapor flow channel. However, the area weighted average temperatures from the simulation resides within 5% error of the experimental results

From Figure 6-12, although the temperature at the bottom of the outlet air flow channel significantly deviates from the simulated curve, the area weighted average temperatures from the simulation resides within 5% error of the experimental results. One possible reason for the high temperature at the bottom of channel may associated with a boundary layer of the air-vapor near the solid surface. The stagnation of airflow at the bottom could possibly lead to higher temperature in the region compared to the central area of the airflow.

6.7 Summary and Conclusion

A two-dimensional mathematical model for heat and mass transfer in in a direct contact condense that directly solves for the enthalpies of air-vapor and water has been proposed. This model fills a vacancy in the literature. The resulting partial differential equations are provided with detailed derivations, and they can be solved using a simple finite differences scheme.

To validate the 2D mathematical model, a lab-scale crossflow condenser was built and tested. Four cases of different boundary conditions were investigated. Water temperatures throughout the 2D domain were measured and the compared with the simulation results. In addition, air-vapor temperatures at the outlet of the condenser were also compared with the simulation. Results show that the analytical solutions of both cooling water and air-vapor coincide with the experimental results within 5% error. However, some regions between isotherm lines of 30°C and 26°C may have errors larger than 10%, especially in the top left region. A non-uniform flow flux near the left corner, likely due to the water droplets splashing and bouncing, might have caused such errors in the region. Therefore, the simulations were performed again by varying the mass flux at the left edge of water spray. As a result, the errors over the whole domain were improved. This indicates that the mathematical model proposed in this chapter can provide accurate predictions of crossflow direct contact packed beds condensers if the inlet conditions are given accurately enough.

Outlet temperatures of air-vapor at five different vertical locations were measured and compared to the simulations results. In all four cases, the first four experimental points from the top are all very close to the simulation results, except the last temperatures measured at the bottom of the air-vapor flow channel that is significantly higher than the simulation results. This could be boundary layer effect of air-vapor that the stagnation of airflow at the bottom could possibly lead

to higher temperature in the region compared to the central area of the airflow. However, in general, the area weighted average of temperatures from the simulation resides within 5% error of the experimental results.

The two-dimensional steady state mathematical model for direct contact crossflow condenser has been successfully validated. This provides a reference for researchers who continue studying HDH desalination systems using crossflow direct contact packed beds condensers as dehumidifiers. The model will also be useful to identify the optimal parameters of direct contact crossflow packed beds condensers which include dimensions and working conditions.

CHAPTER 7: Modeling of Compact Crossflow Cylindrical HDH system: Condenser

Performance Analysis

7.1 Context

In this chapter a novel design of a compact crossflow cylindrical HDH system is presented that can be built and scaled easily. The focus of this research study is on a compact crossflow packed condenser utilizing perforated air tubes to diffuse humidified air radially. Cooling water then drips vertically through the packed bed and meets humidified air. To analyze the performance, a two-dimensional steady-state conservation equation has been developed. The coupled PDEs are solved numerically to predict water temperature, air/vapor temperature, humidity ratio, and effectiveness of the condenser. Additionally, several designs have been proposed and shown that they can reach effectiveness above 0.90 in most operating boundary conditions.

A compact crossflow cylindrical HDH system in which the evaporator and condenser are integrated with no piping is demonstrated in Figure 7-1 and Figure 7-2. The air enters the evaporator through the perforated tube. Then, it picks up the vapor from heated saline water. This warm humid air then goes to the condenser where freshwater is condensed out from the air-vapor mixture. The evaporator and condenser are filled with a packed bed. In addition, the evaporator and condenser are separated by a perforated divider. One of the advantages of this compact HDH system is that as air flows radially through the perforated tube, the mass flux of air/vapor decreases. Therefore, it gets more residence time to get in contact with cooled water. It increases the effectiveness of the overall system.

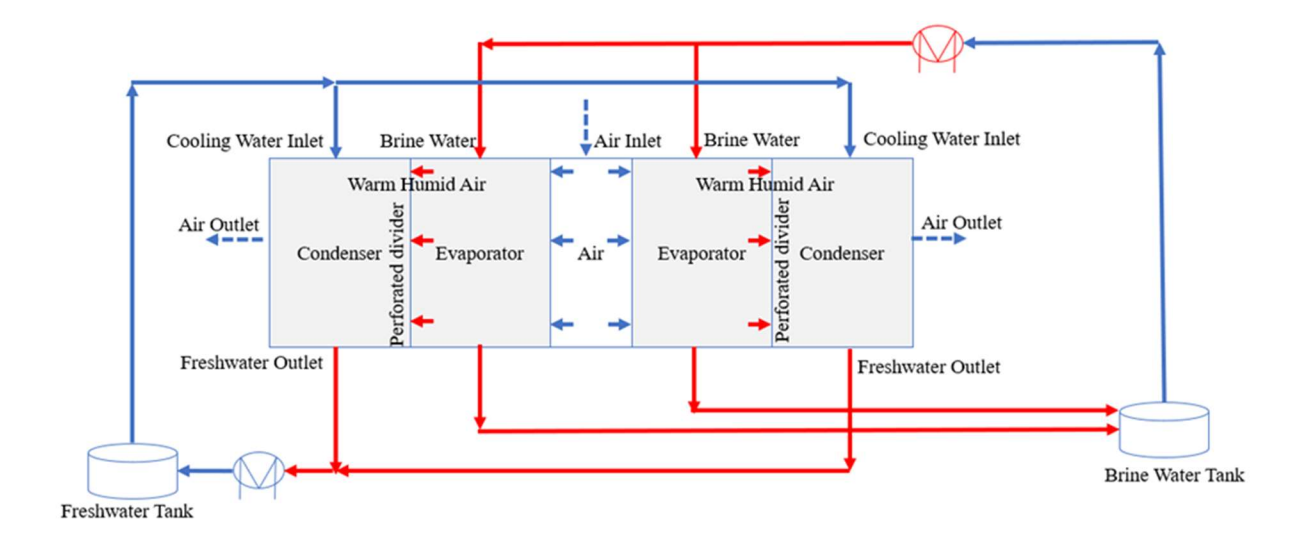


Figure 7-1. 2D view of the proposed compact crossflow cylindrical crossflow HDH system consisting of perforated tubes for airflow, evaporator, and condenser. The blue line represents the cooled air/water, and the red line presents the hot air/water

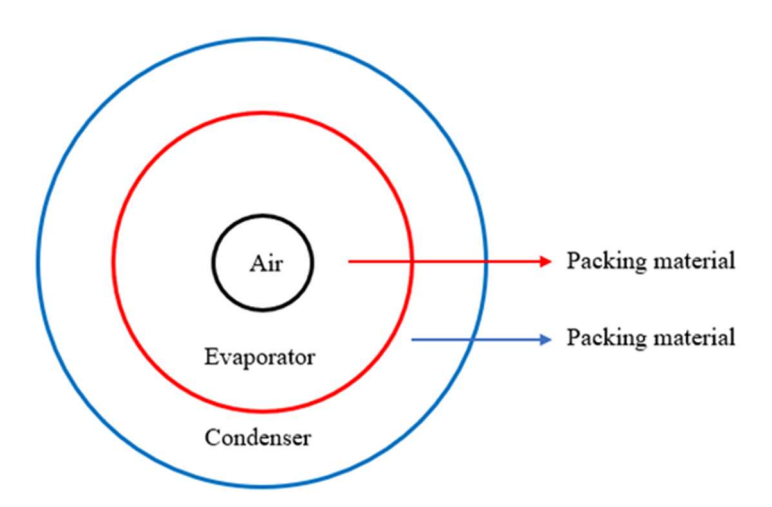


Figure 7-2. Top view of the proposed crossflow cylindrical HDH system consisting of three perforated tubes for airflow, evaporator, and condenser

Some of the other advantages of this compact crossflow cylinder are that it can be readily available with a standard tube. It is easily scalable due to its compactness and will be simple to construct. In summary, the new compact crossflow HDH system is only three simple perforated

tubes that consist of an evaporator and condenser and a perforated tube for airflow. No complex piping system will be needed. Therefore, it can be easily accommodated in industrial places like solar draft towers as well as in solar chimneys to produce fresh water.[84]

This chapter specifically focuses on the condenser design. A two-dimensional steady-state formulation has been presented for the crossflow cylindrical condenser using a packed bed. The mathematical model has been solved by the finite difference method. Several designs are proposed and performance analyses between designs are compared. A comparison of several designs' effectiveness and water output is provided. Additionally, it is shown that the new compact design is more effective under most working circumstances.

7.2 Nomenclature

a Specific area of packing material (m²/m³)

C_p Specific heat (kJ/kgK)

D Molecular diffusion coefficient (m²/s)

Fr Froude number*

g Gravity (m²/s)

 h_v Enthalpy of vapor (kJ/kg)

 h_l Enthalpy of liquid (kJ/kg)

 h_{fg} Enthalpy of condensation(kJ/kg)

k Mass transfer co-efficient (m/s)

M Molecular vapor weight (kg/kmol)

m Mass flow rate (kg/s)

 \ddot{m} Mass flux (kg/m²s)

Nu Nusselt Number*

```
P Total pressure of the system (kPa)
\dot{Q} Heat transfer rate (J/s)
r Radial Direction(m)
Re Reynolds number*
R Universal gas constant (kJ/kmol K)
Sc Schmidt number*
T Temperature (°C or K)
U Overall heat transfers coefficient (W/m^2K)
We Webber Number*
z Depth of packed bed (m)
ρ Density(kg/m<sup>3</sup>)
μ Dynamic viscosity (kg/ms)
ω Humidity ratio (kg/kg) (g / kg of dry air )
\phi Relative Humidity
\sigma_l The surface tension of a liquid (N/m)
\sigma_{pack} The surface tension of packing material (N/m)
*See Appendix for definition of dimensionless number
Subscripts
a Air
amb Ambient state
cond Condensation
G Air/Vapor mixture
```

GA Gas side parameter based on the specific area of packing material.

LA Liquid side parameter based on the specific area of packing material.

l Liquid phase

pack Packed beds

sat Saturation state of species

v Vapor phase

w Wetted

7.3 Mathematical Model Formulation

The condensation depends on the inlet liquid and air temperature, humidity ratio, and ratio of liquid-to-air mass flux. Condensation occurs when cold water contacts hot air/vapor mixture. The flow path of the air and water stream is shown in Figure 7-3. To derive the equation for steady-state operation, several assumptions are made. Both air and water vapor have been considered ideal gas. At the liquid/vapor interface, heat flows from the liquid to the air, and at the liquid/solid contact, it flows from the liquid to the packed bed. The analysis takes airflow to be uniform. As a result, the momentum equation is not considered. The bed is regarded as porous media. It is assumed that the system is axisymmetric. At the inlet and throughout the condensation, the relative humidity is taken to be 100%.

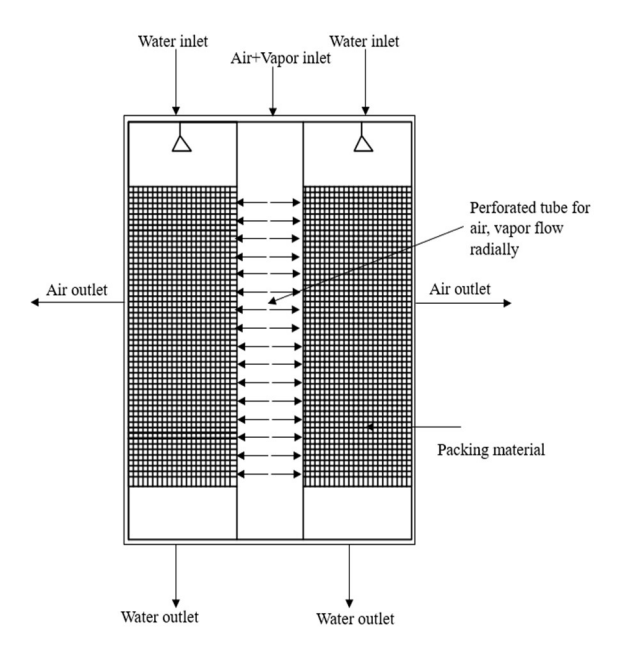


Figure 7-3. Schematic diagram of compact crossflow cylinder illustrating flow direction air/vapor and water stream

A control volume for liquid is shown in Figure 7-4 to apply the conservation of mass and energy. For cylindrical coordinates, it results in,

$$\ddot{m}_{L,r}rd\theta dz - (\ddot{m}_{L,r} + \frac{\partial \ddot{m}_{L,r}}{\partial r}dr)(r + dr)d\theta dz + \ddot{m}_{L,z}rd\theta dr + \frac{\partial \ddot{m}_{L,z}r}{\partial z}dz)drd\theta$$

$$= -\ddot{m}_{cond}rdrd\theta dz$$
(7-1)

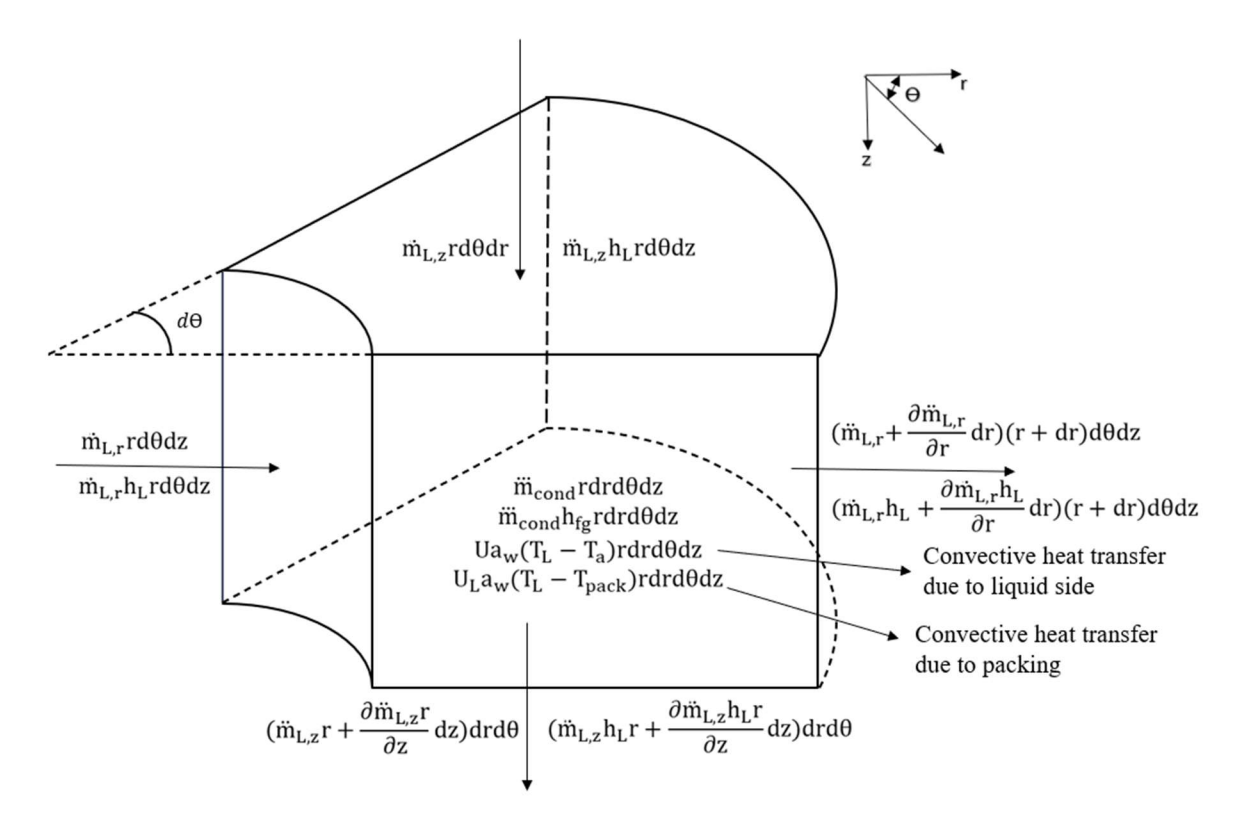


Figure 7-4. Control volume analysis of mass and energy flow in cylindrical coordinates for liquid On the liquid side, it can be represented similarly by using the principle of conservation of energy as,

$$\ddot{m}_{L,r}h_{L}rd\theta dz - \left(\ddot{m}_{L,r}h_{L} + \frac{\partial \ddot{m}_{L,r}h_{L}}{\partial r}dr\right)(r+dr)d\theta dz + \ddot{m}_{L,z}h_{L}rd\theta dz - (\ddot{m}_{L,z}h_{L})drd\theta dz + \frac{\partial \ddot{m}_{L,z}h_{L}r}{\partial z}dz)drd\theta + \frac{\partial \ddot{m}_{L,z}h_{L}r}{\partial z}dz)drd\theta - Ua_{w}(T_{L})drd\theta dz - U_{L}a_{w}(T_{L} - T_{pack})rdrd\theta dz$$

$$= -\ddot{m}_{cond}h_{fg}rdrd\theta dz$$
(7-2)

In Eq.(7-1) and Eq.(7-2), $\ddot{m}_{L,r}$ is the mass flux of liquid in the r direction and $\ddot{m}_{L,z}$ is the mass flux of liquid in the z-direction. \ddot{m}_{cond} is the rate of condensation. h_L represents the enthalpy of liquid and h_{fg} is the latent heat of condensation. Eq.(7-1) and Eq.(7-2) can be expressed as,

$$\frac{1}{r}\frac{\partial (\ddot{m}_{L,r}r)}{\partial r} + \frac{\partial \ddot{m}_{L,z}}{\partial z} = \ddot{m}_{cond}$$
 (7-3)

$$-\frac{\ddot{m}_{L,r}h_L}{r} - \frac{\partial \ddot{m}_{L,r}h_L}{\partial r} - \frac{\partial \ddot{m}_{L,z}h_L}{\partial z}$$

$$= -\ddot{m}_{cond}h_{fg} + Ua_w(T_L - T_a) + U_La_w(T_L - T_{pack})$$
(7-4)

To make the above equations simpler, liquid flow in the z-direction is regarded as negligible and only the radial direction is considered. Thus, Eq.(7-3) and Eq.(7-4) can be translated into,

$$\frac{\partial \ddot{m}_{L,z}}{\partial z} = \ddot{m}_{cond} \tag{7-5}$$

$$-\frac{\partial \ddot{m}_{L,z}h_L}{\partial z} = -\ddot{m}_{cond}h_{fg} + Ua_w(T_L - T_a) + U_L a_w(T_L - T_{pack})$$
(7-6)

In Eq.(7-6), the first term on the left-hand side depicts the change of liquid enthalpy along the z-direction, and the first term on the right-hand side accounts for the latent heat of condensation. The second term accounts for convective heat transfer due to air/vapor mixture, whereas the third term represents the convective heat transfer due to packing. Expanding the first term in Eq.(7-6) results in,

$$\frac{\partial h_L}{\partial z} = \frac{1}{\ddot{m}_{L,Z}} \left\{ \frac{\partial \ddot{m}_{L,Z}}{\partial z} \left(h_{fg} - h_L \right) - U a_w (T_L - T_a) - U_L a_w (T_L - T_{pack}) \right\}$$
(7-7)

Using a similar approach, a control volume for the air/vapor mixture is used to apply the conservation of mass and energy balance on the air/vapor side.

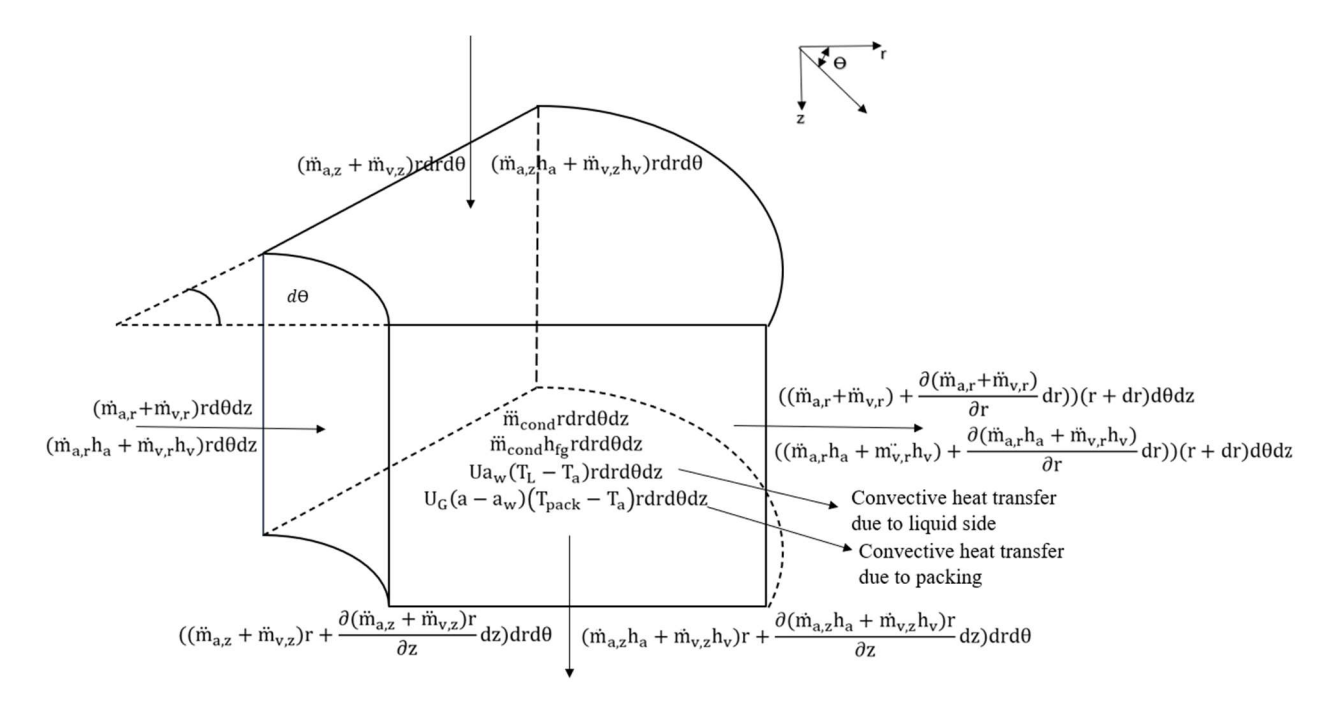


Figure 7-5. Control volume analysis of mass and energy flow in cylindrical coordinates for gas phase

The mass balance for the gas phase (air/vapor) mixture is written as,

$$(\ddot{m}_{a,r} + \ddot{m}_{v,r})rd\theta dz - ((\ddot{m}_{a,r} + \ddot{m}_{v,r}) + \frac{\partial (\ddot{m}_{a,r} + \ddot{m}_{v,r})}{\partial r}dr))(r + dr)d\theta dz$$

$$+ (\ddot{m}_{a,z} + \ddot{m}_{v,z})rdrd\theta - ((\ddot{m}_{a,z} + \ddot{m}_{v,z})r$$

$$+ \frac{\partial (\ddot{m}_{a,z} + \ddot{m}_{v,z})r}{\partial z}dz)drd\theta = \ddot{m}_{cond}rdrd\theta$$

$$(7-8)$$

Similarly, the energy balance for the gas components is:

$$(\ddot{m}_{a,r}h_{a} + \ddot{m}_{v,r}h_{v})rd\theta dz - (\ddot{m}_{a,r}h_{a} + \ddot{m}_{v,r}h_{v}) + \frac{\partial (\ddot{m}_{a,r}h_{a} + \ddot{m}_{v,r}h_{v})}{\partial r}dr))(r$$

$$+ dr)d\theta dz + (\ddot{m}_{a,z}h_{a} + \ddot{m}_{v,z}h_{v})rdrd\theta - ((\ddot{m}_{a,z}h_{a} + \ddot{m}_{v,z}h_{v})r$$

$$+ \frac{\partial (\ddot{m}_{a,z}h_{a} + \ddot{m}_{v,z}h_{v})r}{\partial z}dz)drd\theta + U_{G}(a - a_{w})(T_{pack}$$

$$- T_{a})rdrd\theta dz + Ua_{w}(T_{L} - T_{a})rdrd\theta dz = \ddot{m}_{cond}h_{fg}rdrd\theta dz$$

$$(7-9)$$

In Eq. (7-8) and Eq. (7-9), $\ddot{m}_{a,r}$ and $\ddot{m}_{v,r}$ is the mass flux of air and vapor in radial direction respectively. Similarly, $\ddot{m}_{a,z}$ and $\ddot{m}_{v,z}$ is the mass flux of air and vapor in the z-direction. \ddot{m}_{cond}

is considered a sink of mass as water vapor condenses. Eq.(7-8) and Eq.(7-9) can be further simplified into,

$$-\frac{\ddot{m}_{a,r}}{r} - \frac{\ddot{m}_{v,r}}{r} - \frac{\partial (\ddot{m}_{a,r} + \ddot{m}_{v,r})}{\partial r} - \frac{\partial (\ddot{m}_{a,z} + \ddot{m}_{v,z})}{\partial z} = \ddot{m}_{cond}$$
(7-10)

$$-\frac{\ddot{m}_{a,r}h_{a}}{r} - \frac{\ddot{m}_{v,r}h_{v}}{r} - \frac{\partial (\ddot{m}_{a,r}h_{a} + \ddot{m}_{v,r}h_{v})}{\partial r} - \frac{\partial (\ddot{m}_{a,z}h_{a} + \ddot{m}_{v,z}h_{v})}{\partial z}$$

$$= \ddot{m}_{cond}h_{fg} - U_{G}(a - a_{w})(T_{pack} - T_{a}) - Ua_{w}(T_{L} - T_{a})$$

$$(7-11)$$

In Eq.(7-10) and Eq.(7-11), gas flow in the z-direction is considered negligible. Thus, it can be simplified as,

$$-\frac{\ddot{m}_{a,r}}{r} - \frac{\ddot{m}_{v,r}}{r} - \frac{\partial \ddot{m}_{v,r}}{\partial r} - \frac{\partial \ddot{m}_{a,r}}{\partial r} = \ddot{m}_{cond}$$
 (7-12)

$$-\frac{\ddot{m}_{a,r}h_{a}}{r} - \frac{\ddot{m}_{v,r}h_{v}}{r} - \frac{\partial \left(\ddot{m}_{a,r}h_{a} + \ddot{m}_{v,r}h_{v}\right)}{\partial r}$$

$$= \ddot{m}_{cond}h_{fg} - U_{G}(a - a_{w})\left(T_{pack} - T_{a}\right) - Ua_{w}(T_{L} - T_{a})$$

$$(7-13)$$

In Eq. (7-13), the first three terms on the left side of the equation represent the enthalpy of air and vapor mixture, the first term on the right-hand side is the heat transfer related to the latent heat of condensation, the middle term is the heat transfer due to packing, and the last term represents heat transfer in from liquid to air. Replacing $\ddot{m}_v = \ddot{m}_a \omega$, $\ddot{m}_{a,r} = \frac{m_{a,r}}{2\pi rH}$ and expanding the last term in Eq.(7-13), Eq.(7-12), and (7-13) can be simplified into,

$$-\frac{m_{a,r}}{2\pi r H} \frac{\partial \omega}{\partial r} = \ddot{m}_{cond} \tag{7-14}$$

$$\frac{\partial h_a}{\partial r} = \frac{\partial \omega}{\partial r} (h_{fg} - h_v) - \omega \frac{\partial h_v}{\partial r} + \frac{2\pi r H}{m_{a,r}} U_G (a - a_w) (T_{pack} - T_a)$$

$$+ \frac{2\pi r H}{m_{a,r}} U a_w (T_L - T_a)$$
(7-15)

As in the condenser, air/vapor is saturated at the inlet and relative humidity is 100 percent throughout the condensation. Therefore, the humidity ratio is evaluated with the following equation.

$$\omega = \frac{0.622\emptyset P_{sat}(T_a)}{P - \emptyset P_{sat}(T_a)} \tag{7-16}$$

Pressure is considered atmospheric at the inlet and the equation for pressure drop is given in Appendix

This chapter directly solves Eq.(7-5), Eq.(7-7), Eq.(7-14), and Eq.(7-15) for the enthalpies of air and water (h_a, h_L) as variables. The finite differences method was used to solve these coupled PDEs. Eq.(7-15) was solved by the forward difference scheme and Eq.(7-7) was solved by the backward difference method. Both are solved in terms of Eq. (7-17)

$$K\vec{h} = \overline{T(h)} \tag{7-17}$$

Where K is the matrix of know constant, $\overline{T(h)}$ is a vector of know constants. Xu et al.[85] also followed a similar approach to solve coupled PDEs for rectangular crossflow packed bed systems. They developed an experimental setup and validated the solutions. Steamtable has been used to evaluate all the properties of air and steam. Onda's correlation has been used to calculate mass transfer coefficients of the liquid and gas sides [71]. Heat and mass transfer coefficient correlation has been evaluated by Eckert et al. [79]. In 2021, Abedi et al. [68] analyzed widely used different correlations to estimate mass transfer coefficients. They concluded that Onda's correlations had the closest match with experimental results among all the correlations.

7.4 Model Validation

Two cylinders with a bigger radius have been taken into consideration to verify the mathematical model. A cylinder with a radius of 100 meters for airflow and a cylinder with a radius of 101 meters for the condenser. When the radius being considered is this large (100 -101 m), there

is barely any change in the mass flux of air radially. As a result, it behaves like a typical rectangular shape. The mathematical model of the rectangular crossflow packed bed has been adopted by Xu et al. [85]. Their mathematical model and experimental results had good agreement with each other. The mathematical model for calculating air, and liquid temperature is given below:

$$\ddot{m}_L \frac{\partial h_L}{\partial y} = \ddot{m}_a \frac{\partial \omega}{\partial x} (h_{fg} - h_L) - U_L a_w (T_{pack} - T_L) - U a_w (T_a - T_L)$$
(7-18)

$$\ddot{m}_{a} \frac{\partial h_{a}}{\partial x} = -\ddot{m}_{a} \frac{\partial \omega}{\partial x} \left(h_{fg} - h_{v} \right) - \ddot{m}_{v} \frac{\partial h_{v}}{\partial x} - U_{L} a_{w} (T_{a} - T_{l})$$

$$- U_{G} (a - a_{w}) \left(T_{a} - T_{pack} \right)$$

$$(7-19)$$

The identical boundary condition was used to validate both designs. The detailed boundary condition is shown in Figure 7-6, and it includes the mass fluxes of liquid and air as well as the temperatures of the liquid and air entering the system.

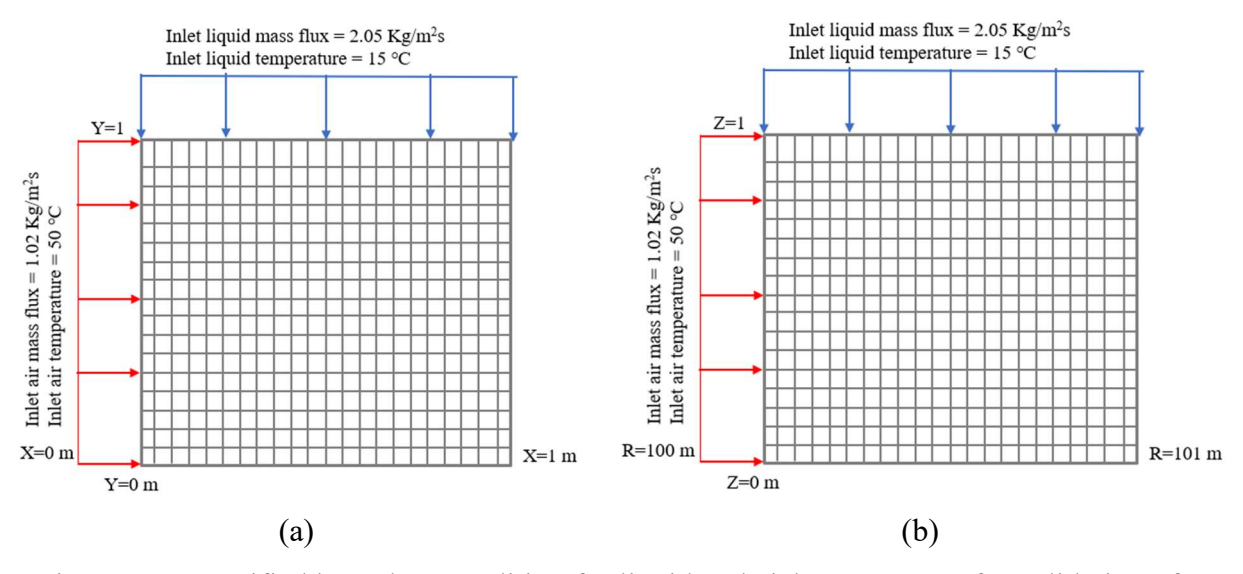


Figure 7-6. Specified boundary condition for liquid and air/vapor stream for validation of compact cylindrical crossflow packed bed condenser(a) rectangle shape crossflow packed bed condenser (b) cylindrical shape crossflow packed bed condenser

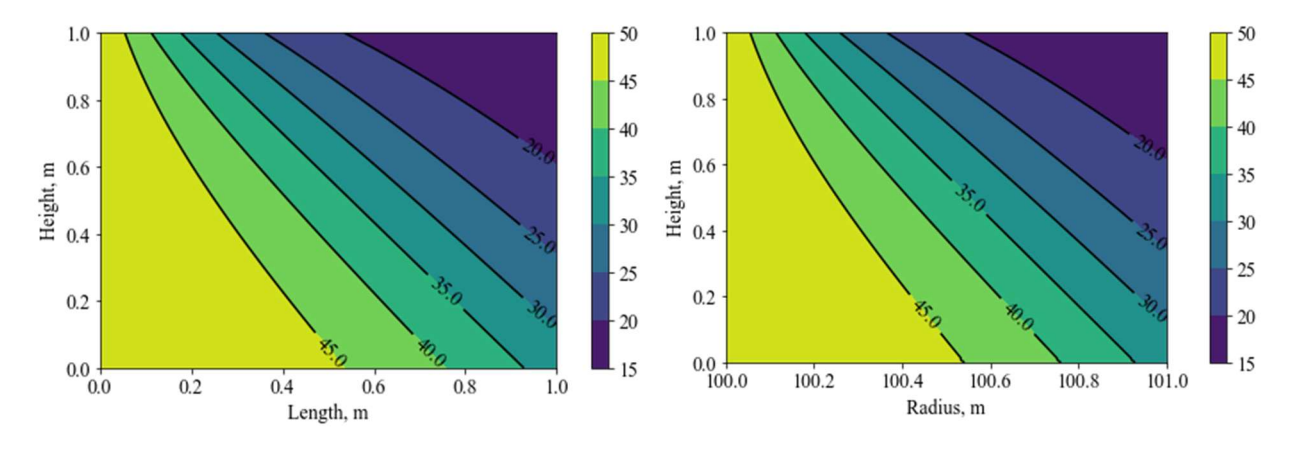
Grid independence was performed with 21x21 nodes, 51x51 nodes, 101x101 nodes, and 151x151 nodes to ensure the precision of the computational outputs of the mathematical model for

cylindrical compact design. Table 1 presents the findings. It can be seen that the temperature of liquid and air does not change significantly with increasing mesh size if nodes are raised above 151x151. Therefore, 151x151 nodes have been chosen for further simulation.

Table 7-1. A summary of grid independency study for inlet liquid temperature = 15° C, inlet air temperature = 50° C, inlet liquid mass flux = 2.05 kg/m^2 s, inlet air mass flux = 1.02 kg/m^2 s

Mesh Size	Liquid Temperature (°C)	Air Temperature (°C)
21x21	39.32	23.39
51x51	38.45	23.02
101x101	38.23	22.90
151x151	38.21	22.88
201x201	38.21	22.87

The contour of the liquid temperature and air temperature have been taken into consideration while comparing the outcomes of the new compact cylindrical crossflow condenser and traditional rectangular condenser.



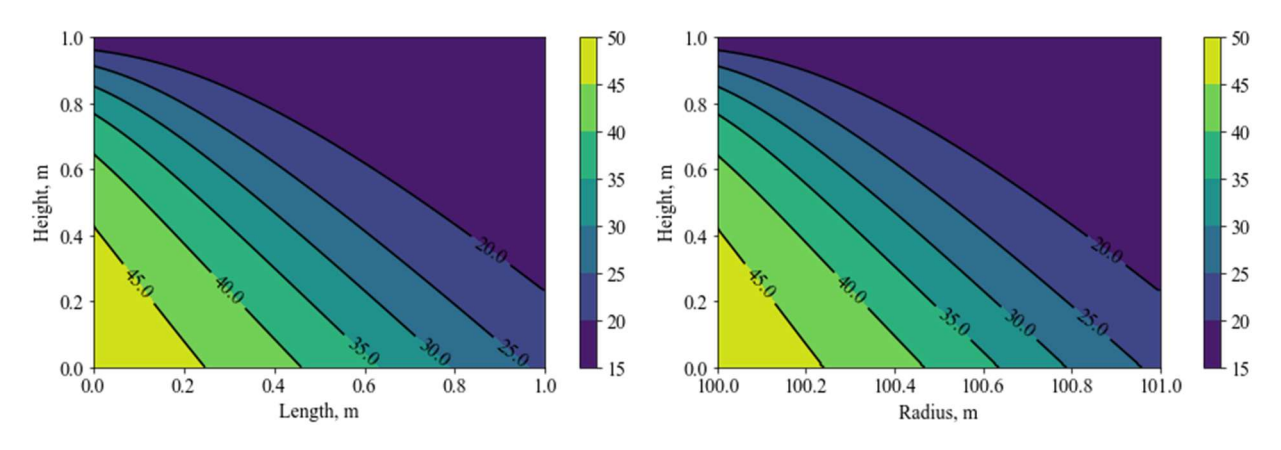
(a) Rectangular crossflow condenser

(b) Cylindrical crossflow condenser

Figure 7-7. Validation of air temperature represented above for liquid mass flux $2.05 \text{ kg/m}^2\text{s}$, air mass flux $1.02 \text{ kg/m}^2\text{s}$, liquid inlet temperature = 15°C , air inlet temperature = 50°C

Figure 7-7 represents the contour of air temperature for rectangular crossflow condenser and crossflow compact cylinder. It can be found that patterns for air temperature in both cases are

almost similar. When comparing the two contours' results, a maximum deviation of 0.12 to 0.15 percent was found, which is within acceptable bounds.



- (a) Rectangular crossflow condenser
- (b) Cylindrical crossflow condenser

Figure 7-8. Validation of liquid temperature represented above for liquid mass flux $2.05 \text{ kg/m}^2\text{s}$, air mass flux $1.02 \text{ kg/m}^2\text{s}$, liquid inlet temperature = 15°C , air inlet temperature = 50°C

In both designs, the domain-wide liquid temperature contour is shown in Figure 7-8. The maximum deviation of 0.50 % in liquid temperature from rectangular shape crossflow has been measured.

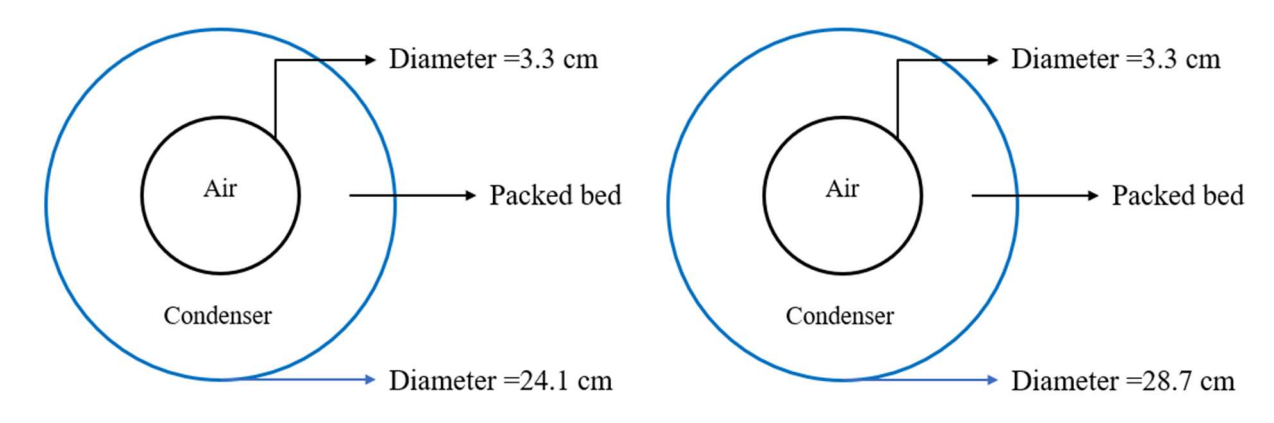
Based on the analysis presented above, the mathematical model for a cylindrical compact crossflow condenser can be used for further analysis.

7.5 Design Proposal and Analysis

7.5.1 Proposed Design

In this section, two designs have been proposed based on the pipes that are available in the industry. As was previously mentioned, one of the major benefits of its compact design is that it doesn't need complex piping and can fit in a variety of industrial spaces. The dimensions of the pipe sizes that are accessible on the market have been studied. For airflow, a pipe size of 1 is selected. It will have holes cut into it. A perforated tube can be designed in the future to guarantee the desired flow rate. Pipe sizes 10 and 12 with a height of 0.5 m are considered while designing

a condenser. It will be also perforated to ensure for airflow at outlet. A thorough breakdown of the two designs is shown in Figure 7-9.



- (a)Design 1 (Pipe size 10 perforated tube for condenser and pipe size 1 for perforated tube for airflow)
- (b)Design 2 (Pipe size 12 perforated tube for condenser and pipe size 1 for perforated tube for airflow)

Figure 7-9. Proposed design for compact crossflow packed bed condenser for analysis

Both pipes can be CPVC. Polypropylene packing has been used for simulation. The specific area of the packing material is 267 m²/m³. The packed bed specific heat capacity is 2.35 kJ/Kg/K, the density is 850 kg/m³ and the void fraction is 87.8%. Several boundary conditions have been considered with different mass flux ratios of liquid to air, and inlet temperature of liquid and air/vapor mixture. Common ideal experimental inlet conditions of cold liquid and humid air for an HDH system range from 15-20 °C and 45-65 °C respectively [19]. Total pressure has been considered 101.3 kPa. Table 2 depicts detailed boundary conditions with mass flux and inlet temperatures of liquid and air for analysis.

Table 7-2. Inlet conditions for analyzing the performance of two different types of compact crossflow packed bed condenser for (liquid mass flux of 1.02 kg/m²s, air mass flux of 1.02 kg/m²s) and for (liquid mass flux of 1.02 kg/m²s and air mass flux of 0.75 kg/m²s)

Case Number	Inlet liquid temperature (°C)	Inlet air temperature (°C)
1	15	65
2	15	60
3	15	55
4	15	50
5	15	45
6	17.5	65
7	17.5	60
8	17.5	55
9	17.5	50
10	17.5	45
11	20	65
12	20	60
13	20	55
14	20	50
15	20	45

7.5.2 Results and Analysis

In this part, the two suggested designs' performance analyses are discussed. To compare the effectiveness and freshwater production between the two designs, 15 cases are considered for each mass flux ratio of liquid to air in Table 7-2. The computed output liquid, air temperature, and humidity ratio for designs 1 and 2 are displayed in Tables 3 and 4, respectively. At the domain's outlet, the weighted area average of temperature and humidity ratio was determined

Table 7-3. Outlet condition for design 1 based on simulation (liquid mass flux of $1.02~kg/m^2s$, air mass flux of $1.02~kg/m^2s$) (Inlet conditions of each case number are defined in Table 7-2)

Case Number	Outlet liquid temperature (°C)	Outlet air temperature	Humidity Ratio
		(°C)	(kg/kg)
1	33.87	44.94	0.0564
2	31.5	29.12	0.0282
3	28.89	20.91	0.0161
4	26.30	17.02	0.0122
5	23.9	15.73	0.0111
6	35.19	44.11	0.0655
7	32.9	33.29	0.0353
8	30.51	25.17	0.021
9	28.5	20.65	0.0154
10	25.75	18.76	0.0136
11	36.52	46.75	0.745
12	34.40	36.93	0.0428
13	32.1	29.13	0.0265
14	29.77	24.12	0.0194
15	27.57	21.91	0.0166

Table 7-4. Outlet condition for design 2 based on simulation (liquid mass flux of 1.02 kg/m²s, air mass flux of 1.02 kg/m²s) (Inlet conditions of each case number are defined in Table 7-2)

Case Number	Outlet liquid temperature (°C)	Outlet air temperature	Humidity Ratio
		(°C)	(kg/kg)
1	34.18	32.11	0.0355
2	31.34	21.7	0.0173
3	27.85	18.5	0.0145
4	25.92	15.63	0.0111
5	23.57	15.3	0.0109
6	35.54	36.46	0.0441
7	32.94	26.2	0.023
8	30.25	20.59	0.0154
9	27.72	18.56	0.0134
10	25.44	17.94	0.0129
11	36.93	40.31	0.0533
12	34.48	30.53	0.0295
13	31.95	24.49	0.0198
14	29.52	21.76	0.0165
15	27.31	20.73	0.0154

Freshwater production has been estimated by using the following equation,

$$\dot{m}_w = \dot{m}_a(\omega_{in} - \omega_{out}) \tag{7-20}$$

Where \dot{m}_w is freshwater production in g/s, \dot{m}_a is the mass flow rate of air in g/s, ω_{in} is inlet humidity ratio and ω_{out} is outlet weighted area average humidity ratio.

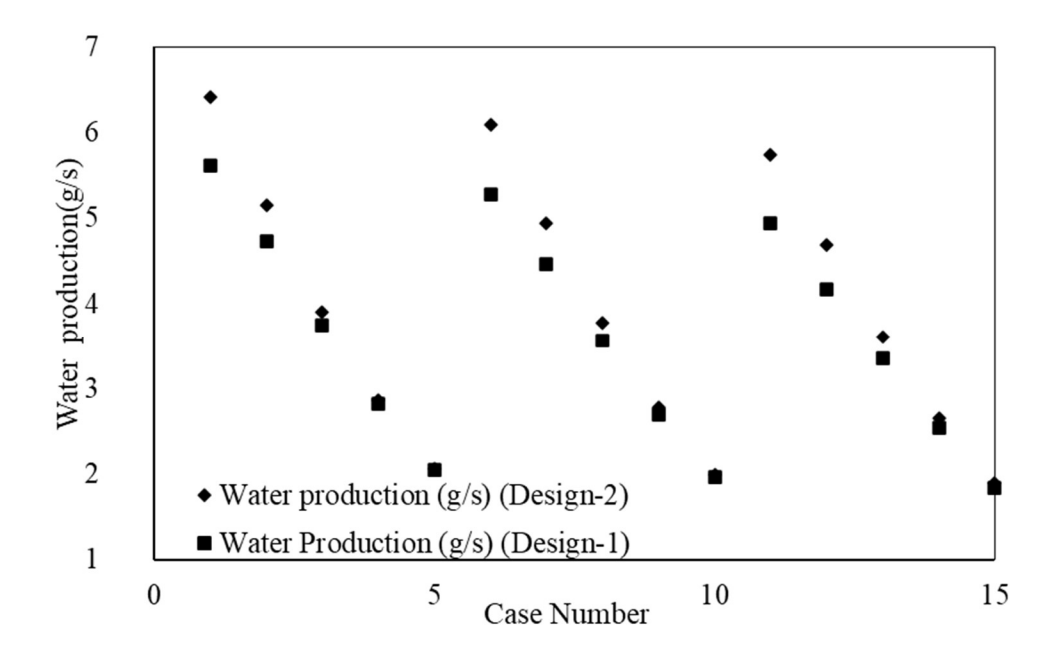


Figure 7-10. Comparison of freshwater production between two proposed designs obtained numerical simulation. The inlet liquid mass flux is $1.02 \text{ kg/m}^2\text{s}$, air mass flux of $1.02 \text{ kg/m}^2\text{s}$. (Inlet conditions of each case number are defined in Table 7-2)

To estimate the effectiveness of the two condensers, the following equation has been used.

$$\epsilon = \frac{\omega_{in} - \omega_{out}}{\omega_{in} - \omega_{minimum}} \tag{7-21}$$

In Eq. (7-21), ω_{in} is the inlet humidity ratio, ω_{out} is the outlet humidity ratio, $\omega_{minimum}$ is the minimum possible humidity ratio in the system which is calculated from the inlet temperature of the liquid.

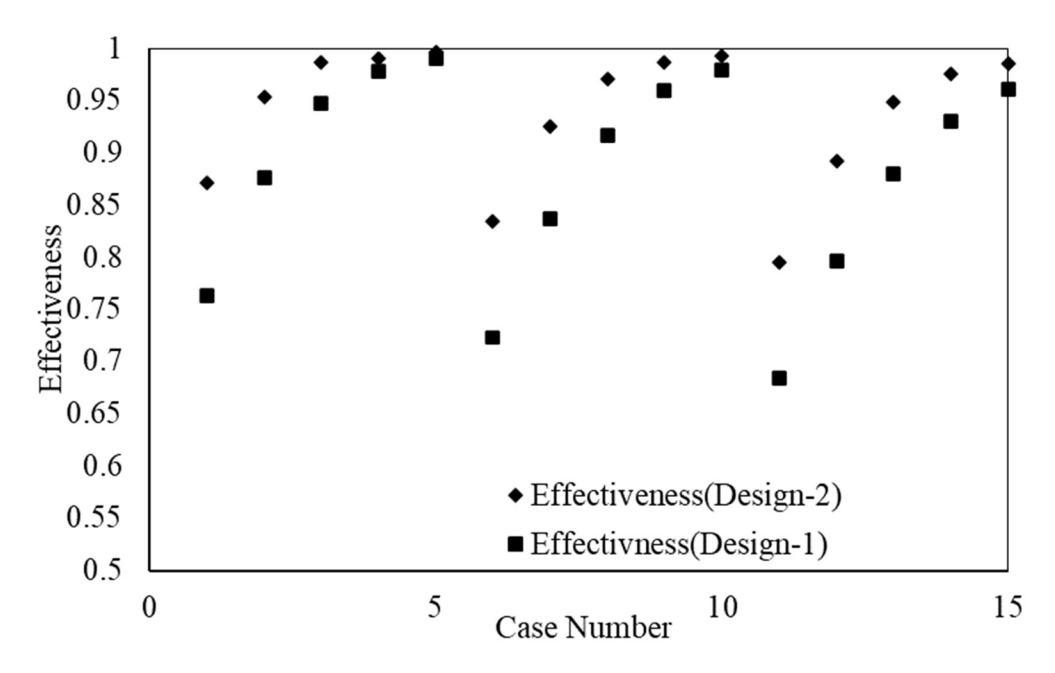


Figure 7-11. Comparison of effectiveness between two proposed designs obtained numerical simulation. The inlet liquid mass flux is 1.02 kg/ m²s, air mass flux of 1.02 kg/ m²s. (Inlet conditions of each case number are defined in Table 7-2)

Figure 7-10 shows that freshwater production in several cases is between 10-20 % higher in design 2 than in design 1. In addition, it can be seen from that design 2 has significantly higher effectiveness when the inlet air temperature is high. The decreased effectiveness can be attributed to two possible cases. Firstly, design 1 packs more compactly than design 2 does. Secondly, one of the benefits of this novel crossflow compact design is that as air and vapor flow radially from inlet to outlet, their mass flux reduces though mass flow rate of air is same throughout the domain. On the contrary, the sprinkler maintains a vertical liquid mass flux at the input. Thus, the ratio of liquid mass flux to air/vapor mixture increases as the air/vapor mixture moves from the intake to the outlet. Both designs have a liquid-to-air mass flux ratio of 1 at the inlet. But at the outlet, the ratio for design 1 is 10, and design 2 is 17. Due to these circumstances, Design 2 is more effective than Design 1.

Similarly, another analysis has been conducted by keeping the inlet liquid-to-air mass flux ratio around 1.33. Table 7-5 and Table 7-6 represent the computed outlet weighted area average temperature of the liquid, air, and humidity ratio.

Table 7-5. Outlet condition for design 1 based on simulation (liquid mass flux of 1.02 kg/m²s, air mass flux of 0.75 kg/m²s) (Inlet conditions of each case number are defined in Table 7-2)

Case Number	Outlet liquid temperature (°C)	Outlet air temperature	Humidity Ratio
		(°C)	(kg/kg)
1	31.07	34.17	0.0387
2	28.81	22.59	0.0183
3	26.44	17.00	0.0122
4	24.41	15.52	0.0110
5	22.23	15.20	0.0107
6	32.70	38.74	0.0488
7	30.53	27.58	0.0247
8	28.32	21.15	0.016
9	26.20	18.69	0.0135
10	24.24	17.93	0.0129
11	34.10	42.28	0.0583
12	32.12	32	0.0319
13	30.07	25.22	0.0207
14	28.05	22.01	0.0167
15	26.2	20.80	0.0154

Table 7-6. Outlet condition for design 2 based on simulation (liquid mass flux of $1.02 \text{ kg/m}^2\text{s}$, air mass flux of $0.75 \text{ kg/m}^2\text{s}$) (Inlet conditions of each case number are defined in Table 7-2)

Case Number	Outlet liquid temperature (°C)	Outlet air temperature	Humidity Ratio
		(°C)	(kg/kg)
1	31.12	24.41	0.0210
2	28.52	16.92	0.0122

Table 7-6 (cont'd)

3	26.06	15.4	0.0109
4	23.87	15.19	0.0108
5	21.96	15.13	0.0107
6	32.75	29.49	0.0288
7	30.32	21.15	0.0161
8	27.97	18.4	0.0133
9	25.85	17.81	0.0127
10	23.97	17.67	0.0126
11	34.43	34.34	0.0377
12	30.85	25.60	0.0152
13	29.85	21.77	0.0165
14	27.80	20.61	0.0153
15	25.80	20.27	0.0149

As per Figure 7-12, in different cases, notably Cases 3,4,5,8,9,10,14, and 15, the freshwater production rate is roughly the same in both designs. In these cases, the inlet air temperature is less than in other specified cases. Thus, it is possible to estimate that both designs will produce almost the same amount of freshwater if the inlet air temperature is less than or equal to 55°C.

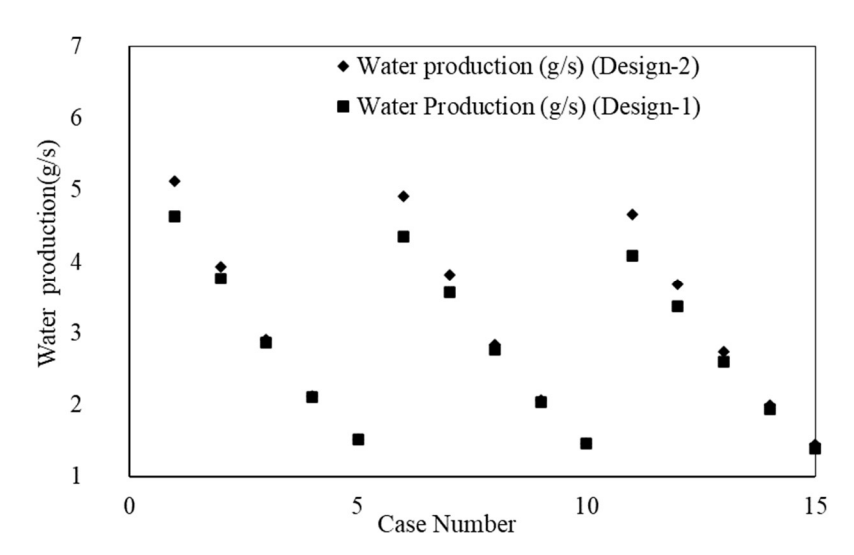


Figure 7-12. Comparison of water production between two proposed designs obtained numerical simulation. The inlet liquid mass flux is 1.02 kg/ m²s, air mass flux of 0.75 kg/ m²s. (Inlet conditions of each case number are defined in Table 7-2)

A similar trend is observed in Figure 7-13 for effectiveness. As explained before, design 2 has higher effectiveness due to having a higher volume of packing and a higher outlet liquid-to-air mass flux ratio. In design 1, the inlet mass flux ratio of liquid-to-air is 1.33. The outlet mass flux ratio of liquid-to-air is 10. For design 2, the outlet mass flux ratio of liquid-to-air is 17. Thus, it gets more time to condense vapor out of humid air.

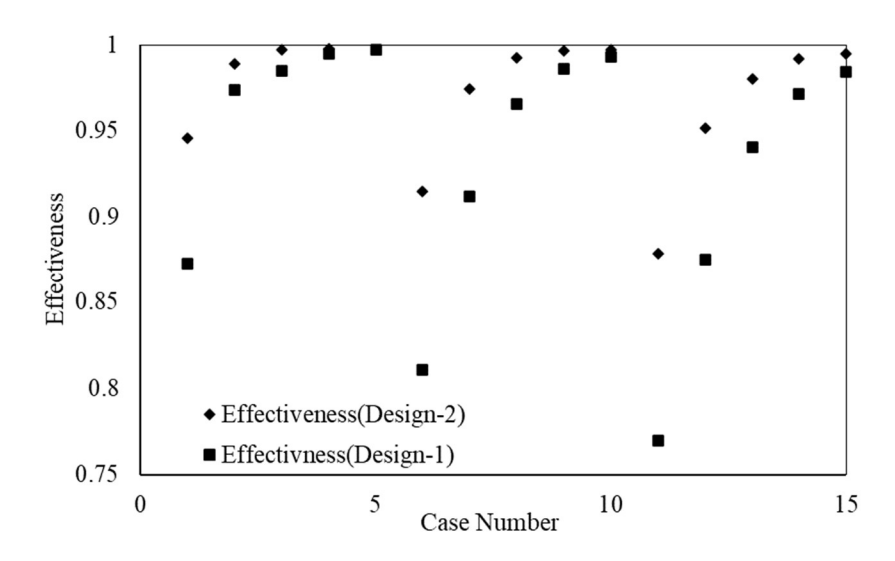


Figure 7-13. Comparison of effectiveness between two proposed designs obtained numerical simulation. The inlet liquid mass flux is 1.02 kg/ m²s, air mass flux of 0.75 kg/ m²s. (Inlet conditions of each case number are defined in Table 2)

From the above analysis, it can be said that both design 1 and design 2 have effectiveness above 0.80 in most of the mentioned cases. In 2006, Li et al. [17] analyzed both counterflow and concurrent direct contact packed bed condensers experimentally. For concurrent direct contact packed bed condensers, they found the highest effectiveness around 0.7. They attained a counterflow direct contact packed bed condenser threshold effectiveness of 0.8. In some specific boundary conditions, the efficacy of this novel design can reach 0.99. To analyze the model in detail, however, an experimental setup will be built in the future.

7.6 Conclusion

A novel design of a compact crossflow cylindrical HDH system is presented in this chapter to analyze the heat and mass transfer of the cylindrical condenser, a steady state 2D numerical model of the condenser is implemented. The mathematical model is simulated using the finite difference method. Several cases of air/vapor inlet and liquid temperatures are studied to evaluate the performance of the two proposed designs, two distinct scenarios for the mass flux of the input air are explored as well. It is found that design 1 is more compact than design 2 and the system has a larger liquid-to-air mass flux ratio, design 2 has performed better in both configurations. However, it can be seen in both cases, that in most of the cases two proposed designs can reach effectiveness above 0.90 at suitable operating conditions. The rate of freshwater production follows a similar pattern. Therefore, the proposed crossflow cylindrical setup can be a great alternative to the presently available direct contact HDH system due to its compactness, less piping system, and high effectiveness. In the future, it should be possible to design a lab-scale crossflow cylindrical condenser using the analyses and observations in this study to conduct an experimental performance evaluation.

CHAPTER 8: Summary, Conclusion, and Future Work

The performance of direct contact condensers is studied in detail throughout this thesis. These studies mostly focused on the direct contact crossflow HDH system. Crossflow packed bed condenser was the main component of studies. These studies will guide the way to solve water scarcity around the world by having an efficient heat exchanger.

In the second chapter, widely used desalination technologies were introduced. A basic HDH system was also introduced. A basic HDH system, consisting of shell and tube condenser and finned tube condenser, was discussed. The absence of prior work was mostly on direct contact packed bed condenser as well as configuration. This thesis covered the blank space of analyzing direct contact packed bed condenser with different configurations concentrating on crossflow.

In the third chapter, a mathematical model was developed with conservation of mass and energy for a crossflow system. Important parameters such effective heat transfer area, Nusselt number, Reynold's number appropriate for the packed bed were also incorporated into the simulations. Finite differences method was adopted to solve coupled PDE's. A comparative study of crossflow packed bed condenser and counter flow condenser was performed. It was found that in most of the considered cases counterflow direct contact condenser is slightly better than crossflow direct contact packed bed condenser. However, crossflow direct contact packed bed condenser still can be a good alternative to counterflow due to its simple installation and scalable opportunities.

In the fourth chapter, an explanation was provided as to why Onda's correlation works better than the other correlations for evaluating the mass transfer coefficients of the packed bed. A counterflow experimental setup was built in the lab and outlet liquid and air temperature was measured for different inlet liquid and air temperature. A wide range of empirical correlations for

packed bed developed by researchers was used. It has been found that Onda's correlations match well. Therefore, in this thesis, Onda's correlation was taken into account to evaluate the vital parameters of packed bed.

In fifth chapter, A wedge shape direct contact packed bed condenser was proposed, and four cases was analyzed, and it has been shown that a wedge shape can have around 8-10 percent than conventional shape direct contact condenser if inlet liquid mass flux can be maintained. In addition to, GA algorithm was adopted to have a basic idea of dimension of lab scale setup, and it has been concluded that a rectangular shape will have better effectiveness than square shape.

In sixth chapter, a lab scale experimental setup was discussed, and experimental results were compared with temperature-based solution. It has been found that temperature-based solution has drawback because air is considered as perfect gas. Therefore, an enthalpy based mathematical model was taken into consideration.

In seventh chapter, A new compact model of HDH system was proposed. A compact cylindrical HDH system which consists of three perforated tubes for airflow, evaporator, and condenser. This compact system will require less piping and it can be accommodated in various spaces such as in solar chimney, solar updraft tower etc. Condenser performance was analyzed, and it was shown that effectiveness can reach up to 0.99 in many boundary conditions.

This research study mostly focused on only one component of HDH system. However, these analyzes can lead us to develop a complete crossflow direct contact HDH system consisting of evaporator and condenser. Additionally, two designs of compact crossflow cylindrical HDH system were proposed in chapter 7 utilizing standard pipe available in the industry. A mathematical model was also proposed which can be investigated in detail by developing an experimental setup. Another significant finding of this thesis is that still there is no correlations for packed bed is

available which can predict the mass transfer coefficient with the range of error 5%. A new empirical correlation should thus be developed.

REFERENCES

- [1] M. Shatat, M. Worall, and S. Riffat, "Opportunities for solar water desalination worldwide: Review," *Sustainable Cities and Society*, vol. 9, pp. 67–80, Dec. 2013, doi: 10.1016/j.scs.2013.03.004.
- [2] F. Alnaimat, M. Ziauddin, and B. Mathew, "A review of recent advances in humidification and dehumidification desalination technologies using solar energy," *Desalination*, vol. 499, p. 114860, Feb. 2021, doi: 10.1016/j.desal.2020.114860.
- [3] H. Sharon and K. S. Reddy, "A review of solar energy driven desalination technologies," *Renewable and Sustainable Energy Reviews*, vol. 41, pp. 1080–1118, Jan. 2015, doi: 10.1016/j.rser.2014.09.002.
- [4] A. M. I. Mohamed and N. A. El-Minshawy, "Theoretical investigation of solar humidification—dehumidification desalination system using parabolic trough concentrators," *Energy Conversion and Management*, vol. 52, no. 10, pp. 3112–3119, Sep. 2011, doi: 10.1016/j.enconman.2011.04.026.
- [5] A. E. Kabeel, M. Abdelgaied, and Y. Zakaria, "Performance evaluation of a solar energy assisted hybrid desiccant air conditioner integrated with HDH desalination system," *Energy Conversion and Management*, vol. 150, pp. 382–391, Oct. 2017, doi: 10.1016/j.enconman.2017.08.032.
- [6] G. Wu, H.-F. Zheng, F. Wang, and Z.-H. Chang, "Parametric study of a tandem desalination system based on humidification-dehumidification process with 3-stage heat recovery," *Applied Thermal Engineering*, vol. 112, pp. 190–200, Feb. 2017, doi: 10.1016/j.applthermaleng.2016.10.078.
- [7] T. M. Missimer and R. G. Maliva, "Environmental issues in seawater reverse osmosis desalination: Intakes and outfalls," *Desalination*, vol. 434, pp. 198–215, May 2018, doi: 10.1016/j.desal.2017.07.012.
- [8] G. P. Narayan, M. H. Sharqawy, E. K. Summers, J. H. Lienhard, S. M. Zubair, and M. A. Antar, "The potential of solar-driven humidification—dehumidification desalination for small-scale decentralized water production," *Renewable and Sustainable Energy Reviews*, vol. 14, no. 4, pp. 1187–1201, May 2010, doi: 10.1016/j.rser.2009.11.014.
- [9] D. U. Lawal, M. A. Antar, and A. E. Khalifa, "Integration of a MSF Desalination System with a HDH System for Brine Recovery," *Sustainability*, vol. 13, no. 6, p. 3506, Mar. 2021, doi: 10.3390/su13063506.
- [10] F. Tahir and S. G. Al-Ghamdi, "Integrated MED and HDH desalination systems for an energy-efficient zero liquid discharge (ZLD) system," *Energy Reports*, vol. 8, pp. 29–34, Jun. 2022, doi: 10.1016/j.egyr.2022.01.028.

- [11] H. Xu, Y. Zhao, and Y. J. Dai, "Experimental study on a solar assisted heat pump desalination unit with internal heat recovery based on humidification-dehumidification process," *Desalination*, vol. 452, pp. 247–257, Feb. 2019, doi: 10.1016/j.desal.2018.11.019.
- [12] J. Wang, N. Gao, Y. Deng, and Y. Li, "Solar power-driven humidification—dehumidification (HDH) process for desalination of brackish water," *Desalination*, vol. 305, pp. 17–23, Nov. 2012, doi: 10.1016/j.desal.2012.08.008.
- [13] K. Bourouni, M. T. Chaibi, and L. Tadrist, "Water desalination by humidification and dehumidification of air: State of the art," *Desalination*, vol. 137, no. 1–3, pp. 167–176, May 2001, doi: 10.1016/S0011-9164(01)00215-6.
- [14] Y. Assouad and Z. Lavan, "Solar Desalination With Latent Heat Recovery," *Journal of Solar Energy Engineering*, vol. 110, no. 1, pp. 14–16, Feb. 1988, doi: 10.1115/1.3268230.
- [15] S. Al-Hallaj, M. M. Farid, and A. Rahman Tamimi, "Solar desalination with a humidification-dehumidification cycle: performance of the unit," *Desalination*, vol. 120, no. 3, pp. 273–280, Dec. 1998, doi: 10.1016/S0011-9164(98)00224-0.
- [16] R. H. Xiong, S. C. Wang, L. X. Xie, Z. Wang, and P. L. Li, "Experimental investigation of a baffled shell and tube desalination column using the humidification-dehumidification process," *Desalination*, vol. 180, no. 1–3, pp. 253–261, Aug. 2005, doi: 10.1016/j.desal.2005.01.007.
- [17] Y. Li, J. F. Klausner, R. Mei, and J. Knight, "Direct contact condensation in packed beds," *International Journal of Heat and Mass Transfer*, vol. 49, no. 25–26, pp. 4751–4761, Dec. 2006, doi: 10.1016/j.ijheatmasstransfer.2006.06.013.
- [18] J. F. Klausner, Y. Li, M. Darwish, and R. Mei, "Innovative Diffusion Driven Desalination Process," *Journal of Energy Resources Technology*, vol. 126, no. 3, pp. 219–225, Sep. 2004, doi: 10.1115/1.1786927.
- [19] F. Alnaimat, J. F. Klausner, and R. Mei, "Transient analysis of direct contact evaporation and condensation within packed beds," *International Journal of Heat and Mass Transfer*, vol. 54, no. 15, pp. 3381–3393, Jul. 2011, doi: 10.1016/j.ijheatmasstransfer.2011.03.048.
- [20] F. Alnaimat and J. F. Klausner, "Solar diffusion driven desalination for decentralized water production," *Desalination*, vol. 289, pp. 35–44, Mar. 2012, doi: 10.1016/j.desal.2011.12.028.
- [21] M. Zamen *et al.*, "Experimental investigation of a two-stage solar humidification—dehumidification desalination process," *Desalination*, vol. 332, no. 1, pp. 1–6, Jan. 2014, doi: 10.1016/j.desal.2013.10.018.
- [22] D. U. Lawal, M. A. Antar, A. Aburub, and M. Aliyu, "Performance assessment of a cross-flow packed-bed humidification-dehumidification (HDH) desalination system the effect of mass extraction," *dwt*, vol. 104, pp. 28–37, 2018, doi: 10.5004/dwt.2018.21876.

- [23] M. I. Zubair, F. A. Al-Sulaiman, M. A. Antar, S. A. Al-Dini, and N. I. Ibrahim, "Performance and cost assessment of solar driven humidification dehumidification desalination system," *Energy Conversion and Management*, vol. 132, pp. 28–39, Jan. 2017, doi: 10.1016/j.enconman.2016.10.005.
- [24] S. Hou, S. Ye, and H. Zhang, "Performance optimization of solar humidification—dehumidification desalination process using Pinch technology," *Desalination*, vol. 183, no. 1–3, pp. 143–149, Nov. 2005, doi: 10.1016/j.desal.2005.02.047.
- [25] A. Fouda, S. A. Nada, H. F. Elattar, S. Rubaiee, and A. Al-Zahrani, "Performance analysis of proposed solar HDH water desalination systems for hot and humid climate cities," *Applied Thermal Engineering*, vol. 144, pp. 81–95, Nov. 2018, doi: 10.1016/j.applthermaleng.2018.08.037.
- [26] Y. Zhao, H. Zheng, S. Liang, N. Zhang, and X. long Ma, "Experimental research on four-stage cross flow humidification dehumidification (HDH) solar desalination system with direct contact dehumidifiers," *Desalination*, vol. 467, pp. 147–157, Oct. 2019, doi: 10.1016/j.desal.2019.06.003.
- [27] P. Gabrielli *et al.*, "Combined water desalination and electricity generation through a humidification-dehumidification process integrated with photovoltaic-thermal modules: Design, performance analysis and techno-economic assessment," *Energy Conversion and Management: X*, vol. 1, p. 100004, Jan. 2019, doi: 10.1016/j.ecmx.2019.100004.
- [28] T. Hu, A. H. Hassabou, M. Spinnler, and W. Polifke, "Performance analysis and optimization of direct contact condensation in a PCM fixed bed regenerator," *Desalination*, vol. 280, no. 1–3, pp. 232–243, Oct. 2011, doi: 10.1016/j.desal.2011.07.008.
- [29] H. Müller-Holst, M. Engelhardt, and W. Schölkopf, "Small-scale thermal seawater desalination simulation and optimization of system design," *Desalination*, vol. 122, no. 2–3, pp. 255–262, Jul. 1999, doi: 10.1016/S0011-9164(99)00046-6.
- [30] M. F. A. Goosen *et al.*, "Solar energy desalination for arid coastal regions: development of a humidification—dehumidification seawater greenhouse," *Solar Energy*, vol. 75, no. 5, pp. 413–419, Nov. 2003, doi: 10.1016/j.solener.2003.07.007.
- [31] H. T. A. El-Dessouky, "Humidification-dehumidification desalination process using waste heat from a gas turbine," *Desalination*, vol. 71, no. 1, pp. 19–33, Jan. 1989, doi: 10.1016/0011-9164(89)87055-9.
- [32] A. Aburub, M. Aliyu, D. Lawal, and M. A. Antar, "EXPERIMENTAL INVESTIGATIONS OF A CROSS-FLOW HUMIDIFICATION DEHUMIDIFICATION DESALINATION SYSTEM," vol. 7, p. 12, 2017.
- [33] F. Merkel, "Verdunstungskühlung VDI, Forschungsarbeitten No. 275," " Kern, DQ," Process Heat Transfer", 1925.

- [34] H. Jaber and R. L. Webb, "Design of Cooling Towers by the Effectiveness-NTU Method," *Journal of Heat Transfer*, vol. 111, no. 4, pp. 837–843, Nov. 1989, doi: 10.1115/1.3250794.
- [35] J. F. Klausner, Y. Li, and R. Mei, "Evaporative heat and mass transfer for the diffusion driven desalination process," *Heat Mass Transfer*, vol. 42, no. 6, pp. 528–536, Apr. 2006, doi: 10.1007/s00231-005-0649-2.
- [36] C. Taylor and P. Hood, "A numerical solution of the Navier-Stokes equations using the finite element technique," *Computers & Fluids*, vol. 1, no. 1, pp. 73–100, Jan. 1973, doi: 10.1016/0045-7930(73)90027-3.
- [37] P. Dechaumphai and W. Kanjanakijkasem, "A Finite Element Method for Viscous Incompressible Thermal Flows," p. 8, 1999.
- [38] "Genetic Algorithms and Machine Learning," p. 5.
- [39] E. Jones, M. Qadir, T. H. van V. Michelle, S. Vladimir, and K. Seong mu, "The state of desalination and brine production. A global outlook," *Science of the Total Environment, 2019*, doi: doi:10.1016/j.scitotenv.2018.12.076.
- [40] M. Prajapati, "A comprehensive review of the geothermal integrated multi-effect distillation (MED) desalination and its advancements," *Groundwater for Sustainable Development*, p. 11, 2022.
- [41] T. Rajaseenivasan, K. K. Murugavel, T. Elango, and R. S. Hansen, "A review of different methods to enhance the productivity of the multi-effect solar still," *Renewable and Sustainable Energy Reviews*, vol. 17, pp. 248–259, Jan. 2013, doi: 10.1016/j.rser.2012.09.035.
- [42] M. Alhaj, A. Hassan, M. Darwish, and S. G. Al-Ghamdi, "A techno-economic review of solar-driven multi-effect distillation," *dwt*, vol. 90, pp. 86–98, 2017, doi: 10.5004/dwt.2017.21297.
- [43] A. Christ, K. Regenauer-Lieb, and H. T. Chua, "Thermodynamic optimisation of multi effect distillation driven by sensible heat sources," *Desalination*, vol. 336, pp. 160–167, Mar. 2014, doi: 10.1016/j.desal.2013.12.006.
- [44] A. de la Calle, J. Bonilla, L. Roca, and P. Palenzuela, "Dynamic modeling and simulation of a solar-assisted multi-effect distillation plant," *Desalination*, vol. 357, pp. 65–76, Feb. 2015, doi: 10.1016/j.desal.2014.11.008.
- [45] A. Akbarzadeh, P. Johnson, and R. Singh, "Examining potential benefits of combining a chimney with a salinity gradient solar pond for production of power in salt affected areas," *Solar Energy*, vol. 83, no. 8, pp. 1345–1359, Aug. 2009, doi: 10.1016/j.solener.2009.02.010.

- [46] A. Kumar and V. V. N. Kishore, "CONSTRUCTION AND OPERATIONAL EXPERIENCE OF A 6000 m2 SOLAR POND AT KUTCH, INDIA," p. 13.
- [47] H. Z. Tabor and B. Doron, "The Beith Ha'Arava 5 MW(e) Solar Pond Power Plant (SPPP)—Progress report," *Solar Energy*, vol. 45, no. 4, pp. 247–253, 1990, doi: 10.1016/0038-092X(90)90093-R.
- [48] T. A. Newell, R. G. Cowie, J. M. Upper, M. K. Smith, and G. L. Cler, "Construction and operation activities at the University of Illinois Salt Gradient Solar Pond," *Solar Energy*, vol. 45, no. 4, pp. 231–239, 1990, doi: 10.1016/0038-092X(90)90091-P.
- [49] M. R. Jaefarzadeh, "Thermal behavior of a small salinity-gradient solar pond with wall shading effect," *Solar Energy*, vol. 77, no. 3, pp. 281–290, Sep. 2004, doi: 10.1016/j.solener.2004.05.013.
- [50] O. M., G. A., and B. A., "SIMULATION OF THE TRANSIENT BEHAVIOUR OF A SALT GRADIENT SOLAR POND IN TUNISIA," *Renewable Energy*, vol. 14,Nos–4, pp. 69–76, 1998.
- [51] H. Liu, "Experiment and simulation study of a trapezoidal salt gradient solar pond," *Solar Energy*, p. 10, 2015.
- [52] M. Karakilcik, "Performance assessment of a solar pond with and without shading effect," *Energy Conversion and Management*, p. 10, 2013.
- [53] M. T. Ali, H. E. S. Fath, and P. R. Armstrong, "A comprehensive techno-economical review of indirect solar desalination," *Renewable and Sustainable Energy Reviews*, vol. 15, no. 8, pp. 4187–4199, Oct. 2011, doi: 10.1016/j.rser.2011.05.012.
- [54] A. Alkaisi, R. Mossad, and A. Sharifian-Barforoush, "A Review of the Water Desalination Systems Integrated with Renewable Energy," *Energy Procedia*, vol. 110, pp. 268–274, Mar. 2017, doi: 10.1016/j.egypro.2017.03.138.
- [55] S. Jiang, Y. Li, and B. P. Ladewig, "A review of reverse osmosis membrane fouling and control strategies," *Science of The Total Environment*, vol. 595, pp. 567–583, Oct. 2017, doi: 10.1016/j.scitotenv.2017.03.235.
- [56] S. Jain and S. K. Gupta, "Analysis of modified surface force pore flow model with concentration polarization and comparison with Spiegler–Kedem model in reverse osmosis systems," *Journal of Membrane Science*, vol. 232, no. 1–2, pp. 45–62, Mar. 2004, doi: 10.1016/j.memsci.2003.11.021.
- [57] J. Wang *et al.*, "A critical review of transport through osmotic membranes," *Journal of Membrane Science*, vol. 454, pp. 516–537, Mar. 2014, doi: 10.1016/j.memsci.2013.12.034.

- [58] M. Qasim, M. Badrelzaman, N. N. Darwish, N. A. Darwish, and N. Hilal, "Reverse osmosis desalination: A state-of-the-art review," *Desalination*, vol. 459, pp. 59–104, Jun. 2019, doi: 10.1016/j.desal.2019.02.008.
- [59] H. Tanaka, "Experimental study of a basin type solar still with internal and external reflectors in winter," *Desalination*, vol. 249, no. 1, pp. 130–134, Nov. 2009, doi: 10.1016/j.desal.2009.02.057.
- [60] . P. K. S., "ECONOMICS OF A HIGH PERFORMANCE SOLAR DISTILLED WATER PLANT," *IJRET*, vol. 03, no. 02, pp. 283–285, Feb. 2014, doi: 10.15623/ijret.2014.0302050.
- [61] Z. Haddad, A. Chaker, and A. Rahmani, "Improving the basin type solar still performances using a vertical rotating wick," *Desalination*, vol. 418, pp. 71–78, Sep. 2017, doi: 10.1016/j.desal.2017.05.030.
- [62] A. Ahsan, M. Imteaz, R. Dev, and H. A. Arafat, "Numerical models of solar distillation device: Present and previous," *Desalination*, vol. 311, pp. 173–181, Feb. 2013, doi: 10.1016/j.desal.2012.11.023.
- [63] N. Setoodeh, R. Rahimi, and A. Ameri, "Modeling and determination of heat transfer coefficient in a basin solar still using CFD," *Desalination*, vol. 268, no. 1–3, pp. 103–110, Mar. 2011, doi: 10.1016/j.desal.2010.10.004.
- [64] S. Marale, C. Chiranjeevi, T. Srinivas, and R. ThundilKaruppa Raj, "Experimental and Computational Fluid Dynamics Studies on Dehumidifier in a Combined Cooling and Desalination Plant," *Journal of Thermal Science and Engineering Applications*, vol. 9, no. 1, p. 011007, Mar. 2017, doi: 10.1115/1.4034596.
- [65] Z. Rahimi-Ahar, M. S. Hatamipour, and Y. Ghalavand, "Experimental investigation of a solar vacuum humidification-dehumidification (VHDH) desalination system," *Desalination*, vol. 437, pp. 73–80, Jul. 2018, doi: 10.1016/j.desal.2018.03.002.
- [66] K. Srithar and T. Rajaseenivasan, "Recent fresh water augmentation techniques in solar still and HDH desalination A review," *Renewable and Sustainable Energy Reviews*, vol. 82, pp. 629–644, Feb. 2018, doi: 10.1016/j.rser.2017.09.056.
- [67] K. Onda, H. Takeuchi, and Y. Okumoto, "MASS TRANSFER COEFFICIENTS BETWEEN GAS AND LIQUID PHASES IN PACKED COLUMNS," *J. Chem. Eng. Japan / JCEJ*, vol. 1, no. 1, pp. 56–62, 1968, doi: 10.1252/jcej.1.56.
- [68] M. Abedi, P. Saha, X. Tan, J. F. Klausner, and A. Benard, "Evaluation of Mass Transfer and Interfacial Area Correlations in DirectContact Packed-Bed: Comparison of Correlations," presented at the 2nd International Conference on Fluid Flow and Thermal Science (ICFFTS'21), Nov. 2021. doi: 10.11159/icffts21.118.

- [69] J. M. Blackledget, "Iterative Methods of Solution," in *Digital Signal Processing*, Elsevier, 2006, pp. 237–254. doi: 10.1533/9780857099457.2.237.
- [70] J. C. Kloppers and D. G. Kröger, "A CRITICAL INVESTIGATION INTO THE HEAT AND MASS TRANSFER ANALYSIS OF CROSSFLOW WET-COOLING TOWERS," *Numerical Heat Transfer, Part A: Applications*, vol. 46, no. 8, pp. 785–806, Nov. 2004, doi: 10.1080/104077890504113.
- [71] K. Onda, H. Takeuchi, and Y. Okumoto, "MASS TRANSFER COEFFICIENTS BETWEEN GAS AND LIQUID PHASES IN PACKED COLUMNS," *J. Chem. Eng. Japan / JCEJ*, vol. 1, no. 1, pp. 56–62, 1968, doi: 10.1252/jcej.1.56.
- [72] D. Van Krevelen and P. Hoftijzer, "Kinetics of simultaneous absorption and chemical reaction," *Chemical Engineering Progress*, vol. 44, no. 7, pp. 529–536, 1948.
- [73] M. G. Shi and A. Mersmann, "Effective interfacial area in packed columns," *International Journal of Heat and Mass Transfer*, vol. 54, no. 15–16, pp. 3381–3393, 2011.
- [74] R. Billet and M. Schultes, "Predicting mass transfer in packed columns," *Chem. Eng. Technol.*, vol. 16, no. 1, pp. 1–9, Feb. 1993, doi: 10.1002/ceat.270160102.
- [75] J. Zech and A. Mersmann, "Liquid flow and liquid phase mass transfer in irrigated packed columns," *Proceedings of Institution Chemical Engineering Symposium Series*, vol. 56, p. 39, 1979.
- [76] S. Puranik and A. Vogelpohl, "Effective interfacial area in irrigated packed columns," *Chemical Engineering Science*, vol. 29, pp. 501–507, 1974.
- [77] N. Kolev, "Operational parameters of randomly packed-columns," *Chemie Ingenieur Technik*, vol. 48,no.12, pp. 1105–1112, 1976.
- [78] J. L. Bravo and J. R. Fair, "Generalized correlation for mass transfer in packed distillation columns," *Ind. Eng. Chem. Proc. Des. Dev.*, vol. 21, no. 1, pp. 162–170, Jan. 1982, doi: 10.1021/i200016a028.
- [79] E. Eckert and R. Goldstein, *Measurements in heat transfer*. Hemisphere, Washington DC, 1976.
- [80] M. A. A. Albadr, S. Tiun, M. Ayob, and F. T. AL-Dhief, "Spoken language identification based on optimised genetic algorithm–extreme learning machine approach," *Int J Speech Technol*, vol. 22, no. 3, pp. 711–727, Sep. 2019, doi: 10.1007/s10772-019-09621-w.
- [81] S. Mirjalili, *Evolutionary Algorithms and Neural Networks*, vol. 780. Cham: Springer International Publishing, 2019. doi: 10.1007/978-3-319-93025-1.

- [82] J. H. Holland, Adaption in Natural and Artificial Systems. An Introductory Analysis with Application to Biology, Control and Artificial Intelligence, 1st ed. The University of Michigan: Ann Arbor, MI, USA, 1975.
- [83] M. A. Albadr, S. Tiun, M. Ayob, and F. AL-Dhief, "Genetic Algorithm Based on Natural Selection Theory for Optimization Problems," *Symmetry*, vol. 12, no. 11, p. 1758, Oct. 2020, doi: 10.3390/sym12111758.
- [84] C. Méndez and Y. Bicer, "Integration of solar chimney with desalination for sustainable water production: A thermodynamic assessment," *Case Studies in Thermal Engineering*, vol. 21, p. 100687, Oct. 2020, doi: 10.1016/j.csite.2020.100687.
- [85] X. Tan, P. Saha, J. Klausner, B. Abbasi, and A. Benard, "Modeling and Experimental Validation of Direct Contact Crossflow Packed Beds Condenser Used in Hdh Desalination Systems," *SSRN Journal*, 2022, doi: 10.2139/ssrn.4162527.

APPENDIX: ONDA'S CORRELATIONS

These correlations are used to estimate the interfacial area of the packed bed and mass transfer coefficients of liquid and gas,

Mass transfer coefficient of liquid, $k_L = 0.005 * Re_{Lw}^{\left(\frac{2}{3}\right)} Sc_L^{-0.5} (ad_p)^{0.4} (\mu_L g/\rho_L)^{\left(\frac{1}{3}\right)}$ Mass transfer coefficient of liquid, $k_G = C * Re_{GA}^{(0.7)} Sc_L^{\left(\frac{1}{3}\right)} (ad_p)^{-2} aD_G$ A wetted specific area, $\frac{a_W}{a} = \left\{1 - exp\left[-1.45(\frac{\sigma_c}{\sigma_L})^{0.75} Re_{LA}^{0.5} Fr_L^{-0.05} We_L^{0.2}\right]\right\}$

Coefficient C in the above equation is indeed affected by air-vapor temperature, however, no correlation is available from previous research for crossflow direct contact condensers. C was manually adjusted in different temperature range based on the author's experience. Future study is required to have a reliable method that can accurately estimate the mass transfer coefficients.

Reynolds number at liquid side based on the specific wet area of packing, $Re_{LW} = \frac{\ddot{m}_L}{a_w \mu_L}$

Reynolds number at gas side based on the specific area of packing, $Re_{GA} = \frac{\ddot{m}_a}{a\mu_G}$,

Reynolds number at liquid side based on the specific area of packing, $Re_{LA} = \frac{m_L}{a\mu_L}$

Schmidt number at the liquid side, $Sc_L = \frac{\mu_L}{\rho_L D_L}$, Schmidt number at the gas side $Sc_G = \frac{\mu_G}{\rho_G D_G}$

Froude number at the liquid side, $Fr_L = \frac{\ddot{m}_L^2 a}{\rho_L^2 g}$, Weber number at the liquid side, $We_L = \frac{\ddot{m}_L^2}{\rho_L \sigma_L a}$